Investigation of Response Amplification and Dynamic Stability of a Hyperloop System

Analysing the Interaction of the Vehicle with a Tubular Shell

MSc Thesis Report

Lukas Huber

Delft University of Technology

TU Delft

HARDT HYPERLOOP

Investigation of Response Amplification and Dynamic Stability of a Hyperloop System

Analysing the Interaction of the Vehicle with a Tubular Shell

by

Lukas Huber

Student Name	Student Number
Lukas Huber	5859018

Thesis committee:	Dr.ir. K.N. van Dalen	TU Delft, supervising chair
	Dr.ir. A.B. Fărăgău	TU Delft, daily supervisor
	Dr. A. Tsetas	TU Delft
	Dr. J. Paul	TU Delft
	Ir. J.S. Hoving	TU Delft
	S. Lamme	Hardt Hyperloop Global, company supervisor
Faculty:	Faculty of Civil Engineering, Delft	
Project Duration:	January, 2024 - July, 2024	

TU Delft

Acknowledgements

This thesis marks the final stage of my master's studies at TU Delft. Throughout these past two years, I went through great personal development. During my time in, I had the opportunity to meet some amazing and inspirational people from all across the globe which helped me in one way or another to reach the point I am currently at. Even though throughout this journey there were times when the Dutch weather and academic stress got to me, when I missed my town in the Italian Alps and the people and relatives from back home, it was also a period of my life which I am very grateful of having experienced and where I would not have wanted to miss any part of it. With this being said I want to devote this section of my thesis to thank the people who accompanied me throughout my academic journey and helped me complete this final step on my way to receiving my Master's degree.

First, I want to thank my committee Chair Dr.ir. Karel van Dalen, who I encountered at several stages of my academic career, from one the very first lectures I took to the courses of moving load dynamics in my specialisation and finally as a supervising chair of my master thesis. I want to thank him for always believing in my capabilities and motivating me to apply for a PhD position under his supervision. I am honoured and thankful that he selected me as a candidate and I am looking forward to collaborating with him in the future.

I want to express my greatest gratitude to my daily supervisor Dr.ir. Andrei Fărăgău who provided me with very detailed insights into the topic and motivated me throughout the process of formulating this thesis. I was always looking forward to the weekly discussions on the topic we had and was excited to see his opinion on my ideas. I am very thankful for the time he took to provide me with precise feedback, answer my questions and guide me throughout my thesis.

Additionally, I want to thank the rest of the thesis committee composed of Dr. Jithu Paul, Dr. Athanasios Tsetas and Ir. Jeroen Hoving for taking their time and sharing their comments and feedback with me. I want to especially thank Dr. Athanasios Tsetas for sharing his knowledge about shell dynamics and eventually joining the committee. I also want to thank the company Hardt Hyperloop and my company supervisor Sascha Lamme for their collaboration, by providing me with a workspace and the opportunity to get insights into the company.

Further, I want to thank my friends I met at TU Delft, with whom I share some of the greatest memories. Aside from our studies, we went on trips, dinners, drinks and many other activities things together. I wish all of them the best in their professional career and hope to keep in touch in the future. I also want to thank my friends back in Italy who always make me feel at home and where it feels like I never left. People who accompanied me through different parts of my life and were always there whenever needed.

Lastly, I want to thank my parents for supporting me throughout my whole educational period emotionally and always supporting my decisions. I especially want to thank my mom for being such an inspirational figure in my life and always having an open ear to hear my complaints and give me advice.

Lukas Huber
Delft, July 2024

Summary

Hyperloop is a high-speed transportation mode that operates through magnetic levitation of so-called pods which are then transported through a tunnel in which a low-pressure environment is created. Due to reduced air resistance and friction, high velocities are achievable. This thesis addresses the behaviour of such a system operating at high velocities, focusing mainly on dynamic stability. The novelty of this study lies hereby in the implementation of a more realistic guideway model in the analysis. This was achieved by modelling the Hyperloop tube as an infinitely long cylindrical shell on a viscoelastic foundation from which the vehicle is suspended through an electromagnetic force, including an active control system.

This study aims to evaluate the system's stability and its sensitivity to changes in the model by using mainly analytical methods which are supplemented by numerical computations where needed. There are two fundamentally different instability mechanisms studied, namely the electromagnetic instability caused by the inherent unstable nature of the suspension system and the wave-induced instability which originates from the energy feedback of radiated anomalous Doppler waves excited by the vehicle moving at large velocities. The research is motivated by two central questions: (1) What is the influence on the steady-state response when employing the more realistic guideway model? (2) What is the influence on the stability when employing such a model?

To address the first research question, only the steady-state of the guideway is analysed. Hereby, the electromagnetic force as well as the vehicle are disregarded and replaced by a constant moving load. To solve the system, the governing equations are projected on circumferential modes and transformed from space-time to the Laplace-wavenumber domain. This study analyses various scenarios based on their dispersion curves and/or steady-state response compared to a reference case.

For the second research question, the study analyses stability phenomena whereby the response of the guideway is expressed using a convolution of its Green's function and the unknown electromagnetic force. Linearising the system around its steady-state equilibrium allows a computation and analysis of its eigenvalues which describe its stability. To complement and verify the analysis of the linearised system, a non-linear transient model is solved by using a numerical time-stepping algorithm.

The study highlights that the cylindrical shell model significantly affects the critical velocity, compared to an Euler Bernoulli beam model. Analysing the vehicle-structure interaction through the linearised stability analysis reveals stability concerns primarily driven by wave-induced instability when operating at supercritical velocities. In the subcritical regime, instability is only caused by the electromagnetic suspension, which can be overcome when choosing the right control parameters. To reduce the risk of instability it is advisable to choose the structural dimension such that the system operates at subcritical velocities to avoid the interaction between the two instability mechanisms.

This research advances the understanding of Hyperloop dynamics and its stability, providing a foundation for future studies and practical implementations aimed at developing the novel transportation mode.

Contents

List of Figures

List of Tables

Nomenclature

Abbreviations

Abbreviation	Definition
EOM	Equation of motion
DOF	Degree of freedom
SDOF	Single degree of freedom
BC	Boundary condition
IC	Interface condition
EMF	Electromagnetic force
EMS	Electromagnetic suspension
EDS	Electrodynamic suspension
PD	Proportional-derivative
PID	Proportional-integral-derivative
FEM	Finite Element method
BEM	Boundary Element method
SAFE	Semi-analytical Finite Element
NL	Non-liner
EB	Euler-Bernoulli

1 Introduction

1.1. Background

Due to the increasing population in urban centres and globalisation, traffic loads are predicted to increase. Since aeroplanes and cars come with a large environmental cost, new travel modes are being investigated. Trains offer a more sustainable option than cars and planes, but due to their limited transportation speed ($\approx$ 300 km/h on selected tracks), they cannot fully replace aviation [5]. The Hyperloop technology, on the other hand, has the potential to provide transportation speeds around 800 km/h or higher. This could reduce the travel time between major cities drastically and thus provide a viable more sustainable alternative to both domestic and international travel [9]. However, the high speeds and technical intricacies of Hyperloop systems pose a potential risk not only for the passengers but also for the longevity of the infrastructure itself. To ensure a safe and comfortable operation further investigations regarding the dynamic interaction between the vehicle and the substructure need to be facilitated [15](pages 13-14). Furthermore, there is currently no such system in operation, which allows for full freedom in the design and development but also means that there is no measurement data which could influence certain design decisions. Therefore, the development of Hyperloop infrastructure relies on computational modelling as a primary source of knowledge.

1.2. Research Problem

In the past, several researchers attempted to study the dynamic behaviour of a Hyperloop system ([1], [6], [7], [28]). Most of them used a simplified approach to model the vehicle-structure interaction using a single-degree-of-freedom system [8]. Hereby the effect of the waves excited by the high-speed moving load problem is being neglected. Those studies considering the effects of the moving vehicle often rely on a simplified modelling approach employing a continuously supported Euler Bernoulli beam. It has been proven that moving loads (above critical velocity) excite propagating waves in the structure even if the load itself is not oscillating ([3], [4],[24]). Considering the vehicle as a moving mass with its dedicated degree of freedom – coupled to the structure by a spring or electromagnetic force – makes the travelling waves interact with the vehicle as the contact force depends on the guideway and vehicle vibration. This vehicle-structure interaction could cause extensive energy feedback into the moving object raising stability concerns, more specifically wave-induced stability ([4], [13]). Adding to that, the electromagnetic suspension system is inherently unstable and needs a control system which forces stability by adjusting the electromagnetic current to maintain a desired target air gap. The two main stability concerns have been studied in the past but often only for simplified models and or separate from one another [7]. To make conclusions about the occurrence of

instability phenomena and find potential measures to mitigate them, more realistic models are required than currently available.

1.3. Research objective

The objective of this research is to delve into stability phenomena and vibrations within a Hyperloop system under operational conditions. This is accomplished by employing a more detailed model of the substructure, representing it as an infinitely long tubular shell on a continuous visco-elastic foundation. The vehicle is characterized by a moving mass supported by electromagnetic suspension. Two key stability phenomena are investigated: wave-induced instability resulting from the moving load/mass problem and stability caused by the control system of the electromagnetic suspension. The research employs analytical approaches wherever feasible, supplemented by numerical methods where required. Essential information about the structure and the system is drawn from the current technological state provided by the company involved in this research project, *Hardt Hyperloop*. By modelling the system in this manner, insights into the vehicle-structure interaction are gathered. By using the developed model, the effects of various model parameters such as stiffness/damping coefficients and tube dimensions can be explored to mitigate vibrations and potential stability concerns at operational velocities. Moreover, the shell model facilitates the examination of how circumferential prestress, induced by the vacuum inside the tube, impacts the dynamic response of the system, thereby advancing Hyperloop development. Further, the shell model allows the investigation of how circumferential prestress, induced by the vacuum inside the tube, impacts the dynamic response of the system. A successful analysis of the posed objectives will contribute to the progression of Hyperloop development, as it highlights yet unknown characteristics of the structure and the structural model.

1.4. Research scope

Hyperloop systems are characterized by their technical complexity and since it is aimed to operate at extreme conditions, the interplay of the single components is crucial for the operation of the system. Certain aspects of such a system have been extensively studied in the past, especially the vehicle and electromagnetic force itself. This research, however, is predominantly focused on the structural aspect of the system. The vehicle is modelled in a simplified manner as a concentrated mass, neglecting the effects of aerodynamic forces. Recognizing the tubular cross-section's deviation from the Euler-Bernoulli beam theory due to its small radius-to-span ratio, the study employs a shell analysis of the tubular cross-section for a more realistic modelling approach. In contrast to the actual Hyperloop guideway, the vehicle is suspended straight from the tube and not from an internal rail – only a one-layered model is analysed. External factors such as thermal expansion, wind, and snow loads are not considered in this research. On the other hand, the study includes the effects of the low-pressure environment on the inside of the tube, the magnetic suspension, its nonlinear nature, along with the required control system for levitation adjustments (PD controller). The track is assumed to be infinitely long and straight, without turns, switches and out-of-plane motion of the pod.

1.4.1. Research Theory and Methods

The research project faces limitations in employing traditional large-scale experimental methods due to the absence of operational systems capable of achieving the high speeds crucial to the thesis. Consequently, the study is solely based on the insights gathered from a computational model. Given the impracticality of a large-scale Finite Element Method (FEM) model, a semi-analytical modelling approach is favoured, offering qualitative results to understand the system's dynamic behaviour. The modelling cycle involves building a model, whereby the

guideway is expressed as a tube and analysed using the shell theory. To achieve the desired outcomes, the process is split into two main parts. The first one focuses on building the guideway model and the second part looks mainly into the vehicle-structure interaction concerning instability. In the first part, the guideway model is solved in the Fourier/Laplace domain to obtain the Green's function for a moving impulse load. Using this function allows computation of the linear response to any load by evaluating a convolution integral. Furthermore, this section is supposed to expand the knowledge of tubular shells subject to moving loads and how certain modelling decisions are affecting the steady-state response. The second part of this thesis uses the Green's function in combination with the linearised electromagnetic force to quantify the stability of the system through an analysis of the eigenvalues. Thus properly accounting for the interaction between the vehicle and the guideway. The results from that analysis are verified by computing the non-linear response of the interaction using a numerical solution routine. This gives also insights into potential limit-cycle vibrations of the system.

1.5. Research questions

Based on the research objective and scope the following set of research questions can be formulated:

1. *What is the influence on the system's steady-state response when properly accounting for the tube through a cylindrical shell compared to a classical Euler-Bernoulli beam?*

    - *How is the critical velocity influenced by using the shell?*
    - *To what extent do the structural characteristics influence the critical velocities and consequently could be used in vibration reduction?*
    - *How does the steady-state response change when the vacuum on the inside of the tube is considered?*
    - *Can a beam be used as a reduced-order or phenomenological model for the shell to qualitatively predict the steady-state response?*

    Answering this research question is supposed to highlight the qualitative differences inherent to the shell model compared to a beam model. The variation in structural characteristics can be studied based on the steady-state response of the shell. By trying to define a beam model which is supposed to resemble the shells qualitatively, it is possible to make the two different modelling methods more comparable and thus possible to spot their differences. Further, this question is supposed to highlight the relevance of vibration suppression by adjusting the structural parameters of the guideway and highlights the effects that the vacuum on the inside of the tube has. This aspect can solely be studied in the shell model.

2. *What is the influence on the system's stability when properly accounting for the tube through a cylindrical shell compared to a classical Euler-Bernoulli beam?*

    - *To what extent do the structural characteristics influence the potential limit cycles and vibrations under operational conditions?*

    By answering this second central research question it is aimed to generate more knowledge on the dynamic stability of the shell and investigate how it diverges from the widely studied beam theories.

1.6. Report Structure

This thesis report is divided into four main chapters: a literature review, a chapter dedicated to deriving the equations which describe the structure, the analysis and interpretations of the

guideway model, a chapter focusing on the derivation describing the electromagnetic force and the instability of the system composed of the structure and the vehicle, and a final chapter which analyses the results obtained from the vehicle-structure interaction and stability analysis.

The second chapter is the literature study conducted for this thesis and covers the fundamental concepts and the current state of research relevant to this study. It includes the basics of the stability of systems, and the fundamentals of the dynamics of moving loads, emphasizing the use of Fourier and Laplace transformations as well as wave propagation. One section is dedicated to electromagnetic levitation, including control systems. Additionally, shell theory is described, detailing the stress resultants on shell edges, circumferential discretisation, and modeshapes of finite circular shells.

Chapter 3 describes the development and solution of the Hyperloop guideway model, excluding the vehicle suspended by the EMF. It starts by providing the assumptions and descriptions underlying the guideway model, ensuring a clear understanding of the foundational aspects. The solution method to obtain the time-domain response of the system is then described, based on the formulation of governing equations in both space-time and Laplace-wavenumber domains. The chapter discusses the dispersion relations for both free shells and shells on viscoelastic foundations. The chapter also focuses on the computational limitations of the selected solution method, whereby an alternative method and further insights into computational cost can be found in Appendix A. The final section of the chapter highlights the main findings obtained from a steady-state response of the system. This includes the analysis of the influence of several model properties as well as the consideration of the external pressure caused by the low-pressure environment inside the tube. Furthermore, it was attempted to approximate the behaviour of the cylindrical shell by tuning a beam model according to the dispersion relation of the shell.

Chapter 4 focuses on extending the model from Chapter 3 to include the vehicle-structure interaction through an EMF and conducting a stability analysis of the Hyperloop system. It includes a derivation of the EMS in both non-linear and linearised formulations based on [7]. The stability analysis is then addressed through the analysis of the eigenvalues of the linearised system which can lead to either divergence (exponential growth) or Hopf bifurcation. The unpressurised shell is compared to the one including the effects of the external pressure and the adjusted beam model concerning the stability of their equilibrium point. Furthermore, the chapter analyses the non-linear behaviour of the system to verify the stability of the linear system as well as explore limit cycle vibrations.

The concluding chapter explains the relevance of this research to the posed problem and presents a critical reflection on the research method and the results, focusing on answering the main research questions. Finally, some recommendations and potential further steps are proposed.

2

Literature review

2.1. Stability

The stability of equilibrium position(s) is expressed by its reaction to small perturbations. An equilibrium point is considered stable when small perturbations in its vicinity will tend to zero over time (attractive equilibrium point). In case of instability, this initial perturbation will lead to growth over time. It is important to mention that perturbations need to be sufficiently small to remain in the vicinity of the current equilibrium position and not jump to an adjacent equilibrium point or diverge completely.

This concept can be explained by the example of one-dimensional systems given in [19] (example 2.2.1). Hereby the stability of the equilibrium points is investigated for a simple function of $\dot{x} = x^2 - 1$. One has to imagine that fluid flows along a line with a local velocity, whereby the fluid is called the phase fluid and the real axis is called the phase space. For positive values of the function (positive velocities) the flow is to the right (positive axis) and vice versa for negative velocities. The equilibrium or fixed point of the system can simply be found by setting the function $f(x) = x^2 - 1$ to zero. It is trivial that $0 = x^2 - 1$ results in two equilibrium locations at $x = \pm 1$. The vector field as plotted in Figure 2.1 shows the nature of the stability. For those locations where $x^2 - 1 < 0$ the flow tends towards the left side and to the right side where the value of the function is positive. It can be seen in Figure 2.1 that the black equilibrium point on the left is indeed stable for small perturbations. The right point on the other hand diverges from the equilibrium for even the smallest disturbance. This example also shows that the definition of stability in this context is bound by small disturbances. In case the perturbation from the fixed point at $x = -1$ brings the particle to the right of $x = 1$, then the system can also become unstable and diverge to $+\infty$. It can be classified as locally stable but globally unstable [19].

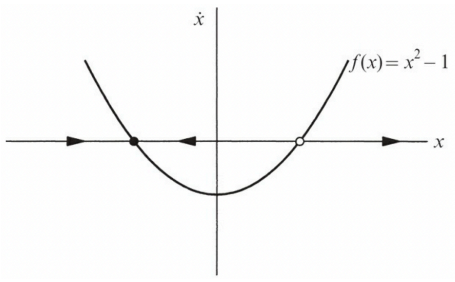

Figure 2.1: Stability of fixed points; left point is stable and the right one unstable for small perturbations [19]

Another approach, rather than depending on graphical methods, involves assessing the

vector field surrounding the equilibrium point. A stable equilibrium can be characterised by the rate of decay that the perturbation experiences. This measure requires a linearisation around the equilibrium position. As shown in section 2.4 of [19] a linearised system of the shape $\dot{\eta} \approx \eta \cdot f'(x_{fix})$ is unstable when $f'(x_{fix}) > 0$ and stable if $f'(x_{fix}) < 0$. In that case, perturbations either grow exponentially or decay over time. From this it can be concluded that the slope around the equilibrium determines the nature of the stability and the magnitude of that slope gives insights into the growth or decay rate of a perturbation. In case the derivative is zero the higher-order terms cannot be neglected, hence a non-linear analysis is needed.

Trajectories for linear systems can be written in the general form:

$$\mathbf{x}(t) = e^{\lambda t} \cdot \mathbf{v} \tag{2.1}$$

whereby $\mathbf{v}$ is a determined vector. For a linear system of this shape, the following expression holds:

$$A\mathbf{v} = \lambda\mathbf{v} \tag{2.2}$$

If this condition remains true, then $\mathbf{v}$ represents the eigenvector and λ the eigenvalue of the matrix A. It follows from linear algebra that the eigenvectors are linearly independent which allows the solution to a linear system to be expressed as a linear combination of its eigenvectors.

In linear systems of higher order, the phase portrait can be expressed by its eigenvectors and eigenvalues. If both eigenvalues in a two-dimensional system are negative, then the system is stable. If both are positive then the system is unstable and if the eigenvalues have different signs then the equilibrium node is a so-called *saddle node*. For that type of stability property, the fixed point is unstable in case $t \to +\infty$ and stable if $t \to -\infty$.

In the presence of damping the eigenvalues are complex of the form $\lambda = a + ib$, where $Re(\lambda) = a$ and $Im(\lambda) = b$. In case $a < 0$ then the system is called an exponentially decaying oscillator and considered stable. Then the phase plot shows a spiral that tends towards the equilibrium as shown in Figure 2.2 (b). If the real part of the eigenvalue is positive then the amplitude of the oscillation grows over time. In this case, the phase plot would be also a spiral but in the opposite flow direction (away from the fixed point). For purely imaginary eigenvalues ($a = 0$) the phase plane consists of concentric trajectories as shown in Figure 2.2 (a). [19]

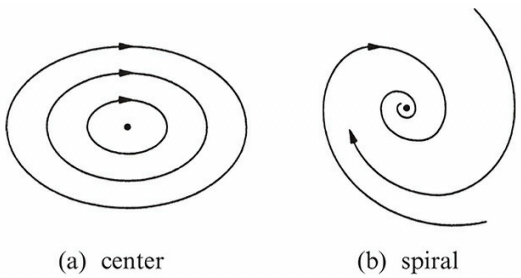

Figure 2.2: Trajectories of complex-valued eigenvectors [19]

2.1.1. Bifurcation

To understand bifurcations, the basic scenario of one-dimensional systems can be revisited. Bifurcations denote alterations in the system dynamics, such as the creation or destruction of fixed points or changes in their nature of stability, are called bifurcations. A fundamental

type of bifurcation is the saddle-node bifurcation, wherein fixed points are either formed or eliminated due to the bifurcation process [19].

A simple example of such a bifurcation can be seen by the system $\dot{x} = r+x^2$. The parameter r can either be positive, negative or zero. In the case of a positive parameter, the system has two fixed points, for r = 0 one solution can be found and for $r > 0$ no fixed point can be found. If r approaches zero from below, the fixed points move towards each other and consequently merge into one in case r=0 (see Figure 2.3). As the vector fields are qualitatively different for positive and negative r makes the transition point at r=0 the bifurcation point of this problem [19].

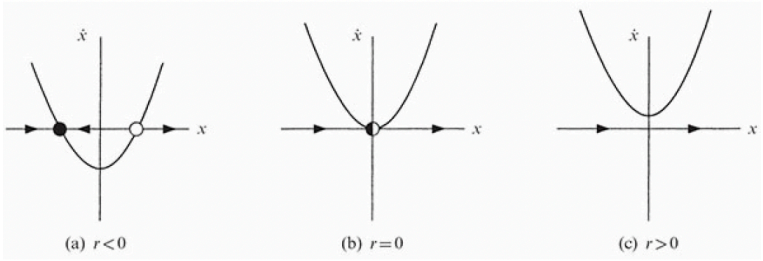

Figure 2.3: Example of saddle point bifurcation for one-dimensional systems [19]

Other cases of bifurcations for linear systems are transcritical bifurcation (bifurcation results in a change of stability) and pitchfork bifurcation (after bifurcation fixed points appear in pairs were both are possible solutions) [19].

Making the transition to two-dimensional systems focuses not only on the nature of fixed points but also on the extension of the behaviour of closed orbits which can also be generated or destroyed at the bifurcation point. In this context an extension of the term bifurcation was mentioned: "If the phase portrait changes its topological structure as a parameter is varied, we say that a bifurcation has occurred" ([19], chapter 8.0). Similar to one-dimensional systems, the saddle-node, transcritical and pitchfork bifurcations can occur. While these types of instability occur once the real-valued eigenvalues of the Jacobian matrix cross the imaginary axis, this is not the case for Hopf bifurcations. In that case, the eigenvalues are complex conjugates and cross the imaginary axis into the right half-plane simultaneously. If the real part is negative and/or a complex conjugate the fixed point is stable. As for the other bifurcation types, the Hopf bifurcation can occur as two types, namely the supercritical and subcritical Hopf bifurcation. Hereby is the former characterised by an unstable spiral enclosed by a stable limit cycle after the bifurcation (see Figure 2.4). In the case of a subcritical bifurcation, the system is surrounded by a stable spiral enclosed by an unstable limit cycle. As the bifurcation point is approached, the limit cycle shrinks to zero and the system becomes unstable. At this point, the trajectories have to jump to a distant attractor which could be another limit cycle, fixed point or potentially infinity. This sudden behaviour makes subcritical Hopf bifurcations especially dangerous [19].

2.1.2. Limit cycles

A limit cycle is a closed trajectory where neighboring trajectories are either spiralling towards or away from the limit cycle, but are never crossing the limit cycle. Limit cycles are classified into stable, unstable and half-stable, whereby the former attracts all trajectories from within and outside. In case this is not the case or only partially then the limit cycle is classified as unstable or half-stable respectively (see Figure 2.4). Limit cycles can only occur in non-linear systems, as the non-linear effects will limit the system's oscillations. While the amplitude of linear oscillations is only dependent on their initial perturbation, this is not the case for limit

cycle oscillations, as they are determined by the structure of the system [19].

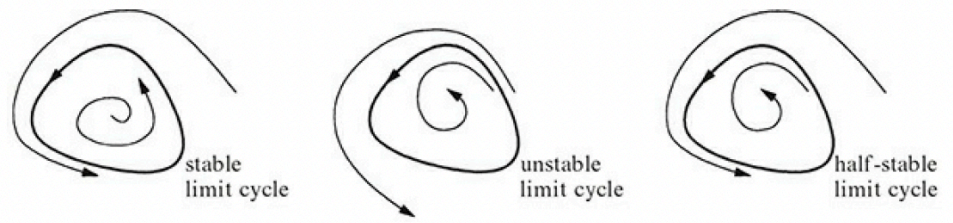

Figure 2.4: Different classifications of limit cycles [19]

2.2. Dynamics of moving loads

2.2.1. Fourier and Laplace transformation

In this section two important mathematical tools are used in solving vibration and wave propagation problems. The Laplace- and Fourier transformations are used to transform a system from the space-time domain into the frequency, wavenumber domain and vice versa when using their inverse form. By doing so it is possible to simplify partial differential equations into ordinary differential equations or even algebraic equations. Both of the transformations are based on the principle of linear superposition of harmonic waves, which renders it impossible to capture any non-linear behaviour [2].

Fourier transformation

The Fourier transformation is based on the principle that any signal can be decomposed into a sum of harmonic sinusoidal waves. If the transformation is applied to a function that is dependent on a specific variable, it will be transformed in such a way that it will be dependent on the reciprocal of the old variable. In the realm of signal processing, two primary types emerge. The first involves employing Fourier transformation to convert a signal from the time domain (t [s]) into the frequency domain (f [1/s]). Additionally, it can express spatial coordinates (x [m]) in terms of the number of cycles per unit distance (k [1/m]), this number is referred to as the wavenumber ([2], Chapter 4).

The analytical expression of the Fourier transformation applied over a space variable is given by the following expression:

$$F(k,t) = \int_{-\infty}^{+\infty} f(x,t) \cdot e^{-ikx} dx \tag{2.3}$$

Transforming the signal back into the space variable is possible by employing the inverse Fourier transformation as expressed below:

$$f(x,t) = \frac{1}{2\pi} \int_{-\infty}^{+\infty} F(k,t) \cdot e^{ikx} dk \tag{2.4}$$

Transforming an n-th order partial derivative for an arbitrary function can be done in the following manner, starting with the first derivative and assuming the radiation condition of $f(x,t) \to 0$ for $x \to \infty$:

$$F'(k,t) = \int_{-\infty}^{+\infty} f'(x,t) \cdot e^{-ikx} dx = \left[f(x,t) e^{-ikx} \right]_{-\infty}^{+\infty} - \int_{-\infty}^{+\infty} (-ik) f(x,t) \cdot e^{-ikx} dx$$
$$= 0 + ik \int_{-\infty}^{+\infty} f(x,t) \cdot e^{-ikx} dx = ik \cdot F(k,t) \tag{2.5}$$
$$F''(k,t) = \int_{-\infty}^{+\infty} f''(x,t) \cdot e^{-ikx} dx = ik \cdot F'(k,t) = (ik)^2 \cdot F(k,t) = -k \cdot F(k,t) \tag{2.6}$$
$$\vdots$$
$$F^{,n}(k,t) = \int_{-\infty}^{+\infty} f^{,n}(x,t) \cdot e^{-ikx} dx = (ik)^n \cdot F(k,t) \tag{2.7}$$

Laplace transformation

This integral transform is similar to the Fourier transform but can also be used for causal problems. This means that it can be applied for problems that are dependent on initial conditions (transient problems) for both periodic and aperiodic signals; the Fourier transform can only describe the steady-state of a signal. In contrast to the real-valued Fourier variable (ω or k as mentioned above), the Laplace variable $s = \sigma + i\Omega$ is complex which allows considering not only the oscillatory part ($e^{i\Omega t}$) but also the change in magnitude of a signal ($e^{\sigma t}$). The constant variable σ also takes away the path of integration from the imaginary axis, ensuring to capture also those roots with zero real part [2] (Chapter 5).

The analytical expression of the Laplace transformation applied over the time variable is given by the following expression:

$$\hat{f}(x,s) = \int_{0}^{+\infty} f(x,t) \cdot e^{-st} ds \tag{2.8}$$

The inverse Laplace transformation can be obtained in the following manner:

$$f(x,t) = \frac{1}{2\pi i} \int_{\sigma-\infty}^{\sigma+\infty} \hat{f}(x,s) \cdot e^{st} ds \tag{2.9}$$

The integration interval for this inverse Laplace transform spans the entire Laplace spectrum. However, if only a one-sided spectrum is available, the Sine and Cosine transforms, as referenced in [2] (Chapter 5), can be employed. These transforms facilitate the conversion of the signal back into the time domain when provided with the imaginary or real part of the Fourier transformation, respectively. These integral transforms necessitate only a one-sided spectrum and are applicable when the real part of s remains constant, hence possible to be moved outside of the integral. For initial conditions of zero, the Sine transformation should be utilized since that condition will be by default satisfied.

Applying the inverse Sine transformation to a function in the Laplace domain can be done in the following manner:

$$f(x,t) = -\frac{2}{\pi} \cdot e^{\sigma t} \int_{0}^{\infty} \hat{\Im} \left[f(x,s) \right] \cdot \sin(\omega t) d\omega \tag{2.10}$$

The Laplace transform for a first and second-order derivative with respect to time, as it is commonly used in mechanics, can be derived in the following manner by making use of integration by parts and the assumption of zero initial conditions:

$$\dot{\hat{f}}(x,s) = \int_0^{+\infty} \dot{f}(x,t) \cdot e^{-st} dt = \left[f(x,t) e^{-st} \right]_0^{+\infty} - \int_0^{+\infty} (-s) f(x,t) \cdot e^{-st} dt$$
$$= 0 + s \cdot f(x,s) \tag{2.11}$$
$$\ddot{\hat{f}}(x,s) = \int_0^{+\infty} \ddot{f}(x,t) \cdot e^{-st} dt = s^2 \cdot f(x,s) \tag{2.12}$$

2.2.2. Beam on continuous supports subject to a constant moving load

As this thesis considers a shell on a viscoelastic foundation, some initial understanding of the wave mechanisms on a simpler element is required. Euler-Bernoulli beams on viscoelastic foundations have been widely studied in the past ([3], [6], [7], [24]). In a moving load problem, the system can experience resonance even though the load is not oscillating. This happens when the load moves at the minimum phase velocity of waves in the guideway. In such a case the displacement amplitude goes to infinity in an undamped system.

In [24] a beam subject to a moving load has been extensively studied. The equation of motion for such a system reads:

$$EIu'''' + \rho A\ddot{u} + k_s u = -P\delta(x - v_0 t) \tag{2.13}$$

The primes denote derivatives of the displacement field u with respect to the spatial coordinate x and the dots resemble derivatives with respect to time. EI signifies the bending stiffness, ρA the distributed mass of the beam and k_s the stiffness of the foundation. The force is in this case a point load of magnitude P moving with a constant speed of v_0.

The critical velocity of such a system is analytically known and is $v_{crit} = \beta/\gamma$, whereby $\beta = \sqrt[4]{k_s/4EI}$ and $\gamma = \sqrt{\rho A/4EI}$ [24]. The critical velocity divides the problem into two domains; being the response at subcritical and supercritical velocities. The responses for a steady-state case are shown in Fig. 2.5 (a) and (b) respectively. The former case is characterised by a localised response and the latter response is dominated by a propagating wave field, with the greatest displacement appearing behind the load.

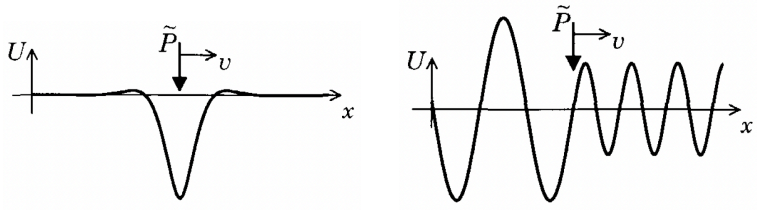

(a) $v_0 < v_{crit}$ **(b)** $v_0 > v_{crit}$

Figure 2.5: Steady-state response of an Euler Bernoulli beam on an elastic foundation subject to a constant moving load [24]

In case a system is subject to a constant moving load, the system is always stable and only subject to dynamic amplification due to resonance close to the critical velocity. In case a moving mass is considered, which has a separate degree of freedom, then the load on the beam is dependent on the interaction between structure and mass. In such a case the waves generated at supercritical velocities can lead to negative energy feedback into the system and an amplification of the vertical oscillations of the sprung mass. This mechanism is called wave-induced instability and is caused by so-called anomalous Doppler waves. This kind of wave can be characterised by its negative frequency and occurrence at supercritical velocities. While normal Doppler waves extract energy from the system, anomalous Doppler waves feed energy

back into the system. The stability is determined by the ratio of these two types of waves, i.e. the energy propagation of the system ([24],[13]).

2.3. Electromagnetic Levitation

For this thesis project is important to understand the various types of magnetic suspension systems, with the main focus on their operational principles and methods of quantification. Notably, two main types of magnetic levitation systems were identified: Electromagnetic suspension (EMS) and Electrodynamic suspension (EDS). It is not straightforward to say which of the two systems is favourable, since each comes with its technological challenges and drawbacks.

The EMS system offers technical simplicity and low energy consumption for vehicle suspension, utilizing permanent attracting magnets on the vehicle and a ferromagnetic guideway maintaining a small airspace ($10 - 20$ mm). However, this system is inherently unstable, even at low velocities, requiring an active control system to adjust the magnetic force corresponding to the air gap when perturbations are applied. On the contrary, the EDS system employs repulsive levitation, creating larger air gaps to mitigate infrastructure imperfections and ensure stability by increasing the levitation force if the vehicle drops. Nonetheless, a major drawback of EDS is electromagnetic drag, complicating guideway construction and necessitating magnetic shielding for the vehicle. Achieving a certain "lift-off speed" for vehicle levitation requires additional wheels at lower velocities. However, at higher speeds, electromagnetic drag diminishes, making EDS cost-effective for high-speed operation. The "Hardt Hyperloop" utilizes EMS for attractive levitation and employs separate propulsion via a linear synchronous motor. This choice is primarily motivated by lower construction costs and energy consumption for levitation, as energy is only needed to adjust the magnetic force. To enhance safety in case of power failure or loss of magnetic force, the "Hardt" model incorporates a catching system ([9], [16]).

2.3.1. Control systems

As mentioned before, the EMS system is by default unstable in nature and therefore requires an active control system to ensure the functioning of the system under operational conditions (small perturbations). Two commonly used control systems are the proportional-derivative (PD) and proportional-integral-derivative (PID) controllers. The latter represents hereby a slightly more sophisticated version of the first one. In essence, both give feedback based on a deviation from a target value. This error is computed at the beginning of the feedback loop, by subtracting the measured value from the target value. Afterwards, a correction term is determined based on a linear combination of the components used in the control system. In the case of a PD controller, there are two terms and for PID there is one extra term present as shown in Figure 2.6. Aside from the additional integral algorithm used in the PID controller, the two types are identical in their structure. The control gains for each of the terms represent a weighting function that is used in the linear combination of the components and results in the control variable. Each of the control variables has a specific function and can remove a certain type of error.

The proportional controller (**P**) adjusts the signal proportional to the error, which works if the error is within a certain threshold. In case the error is too large, the controller overshoots the signal due to the delay of the system; the controller loses stability.

The derivative controller (**D**) computes the rate of change of the error and counters overshooting and oscillatory behaviour of the control system. This controller is very sensitive to noise in the signal as it amplifies the noise, resulting in instability of the system.

The integral controller (**I**) computes a constant error over time which allows to removal

of steady-state errors – an error that cannot fully be removed due to the system limitations is called a steady-state error. The integration over time makes it insensitive to noise which improves the performance of such systems [25]. [1]

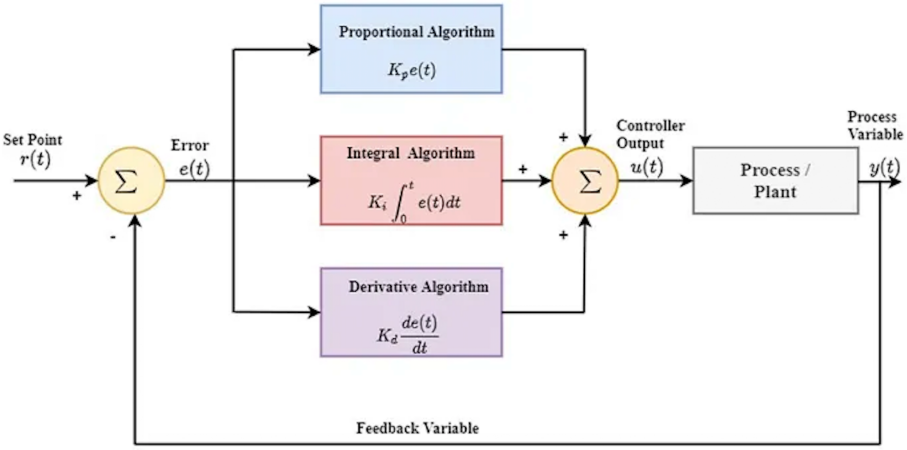

Figure 2.6: Flow chart of PID controller feedback loop [25]

2.3.2. Electromagnetic force

The expression to describe the electromagnetic force was found in the literature and uses a PD control system to regulate the electric current, thus maintaining stability. The equation mainly depends on the air gap, the cross-section area, the electrical current and other parameters of the electromagnet ([7], [8], [16]). The time-dependent electromagnetic force can be described by the following expressions:

$$F_{EMS}(t) = C\left(\frac{I}{\Delta}\right)^2 \tag{2.14}$$

$$C = \frac{\mu_0 N^2 A_m}{4}$$

$$\dot{I} = \frac{\Delta}{2C}\left(U - IR + 2C\frac{I}{\Delta^2}\dot{\Delta}\right) \tag{2.15}$$

$$U = K_p\left(\Delta - \Delta^{ss}\right) + K_d\dot{\Delta} + U^{ss} \tag{2.16}$$

where F resembles the electromagnetic force (*lift*) needed to suspend the vehicle from the guideway with a target air gap. This force depends on the air gap $\Delta = w_0 - u$, the current intensity I and the properties of the magnet, which are represented by the constant C. This coefficient is composed of the vacuum permeability μ_0, the number of turns used in the electromagnetic coil N and the area of the electromagnet pole A_m. The dots over the coefficients represent derivatives with respect to time. R is the resistance of the circuit and U represents the voltage which is regulated through the control system, whereby the coefficients K_p and K_d represent the feedback gains for the proportional and derivative control components used in a PD controller. Note that this expression varies depending on the control system used

[1] The proportional and derivative controller can be interpreted as a spring and dashpot respectively, whereby an increase in the control parameters has a similar effect as an increase in the stiffness and damping constant.

in the model. The error which is supposed to be minimised by the control system is defined by subtracting the air gap Δ from the desired air gap Δ^{ss} (*ss* stands for steady-state). The voltage that leads to the desired air gap in an equilibrium state is represented by the coefficient U^{ss} ([7], [8], [16]).

2.4. Shell theory

Shell theory can be seen as an extension of plate theories, aiming to simplify once again a three-dimensional continuum into a two-dimensional domain. This approach is particularly applicable when the cross-sectional size or thickness is significantly smaller compared to other dimensions such as radius or length. Unlike plate and beam theories, shell theory acknowledges that shell curvature prevents the uncoupling of in-plane displacement (*membrane action*) from out-of-plane displacements (*plate action*). In the case of thin shells, certain assumptions are commonly made. The Kirchhoff hypothesis, for example, assumes that the cross-section (thickness direction for plates and shells) remains orthogonal to the mid-surface, enabling the expression of element behaviour at the mid-surface with linear variation in the thickness direction. Another common assumption for thin shells involves neglecting out-of-plane shear deformation ([10], Chapter 7).

The membrane shell theory is often considered the simplest shell theory and is typically applied to thin shells subjected to distributed loads such as gravity, snow, wind, or pressure. This theory assumes that the shell, due to its thin cross-section, cannot provide significant resistance to bending deformation and thus only considers membrane forces (in-plane forces). However, in the case of a Hyperloop guideway loaded by a 'point load', significant bending deformation occurs, limiting the applicability of the membrane shell theory.

Based on the classical shell theory (*Kirchhoff-Love* shell theory) the theories for cylindrical shells were derived by adjusting the geometrical properties accordingly ($R_1 = R$, $R_2 = \infty$) [10], [11]. The most common ones used are the *Donnell-Mushtari* shell theory (DM shell theory), the *Sanders-Koiter* shell theory and the *Flügge* shell theory. The DM shell theory resembles the most elementary one as it neglects the effect of the tangential displacement for the midsurface changes in curvature [11]. The *Flügge* shell theory, on the other hand, is the most complex of the three. It is important to note that there exist various shell theories for both general cases which can be modified to be used for cylindrical shells. A selection of the various theories is summarised in Chapter 1 of [11] (thin shell theories) whereby their difference lies in the assumptions that are made throughout the derivation process, such as negligence of the coupling through curvature in some terms or overall different definitions of curvature and geometry.

In a study comparing the accuracy of different shell theories, documented in [20], the difference between the *Flügge* and Sanders shell theory was found to be almost negligible. However, the DM shell theory deviates substantially from the other two when applied to low wavenumbers and long tubes.

The governing equation for the *Flügge* shell theory for cylindrical shells subject to an arbitrary load is shown below in Eqs. (2.17) - (2.19) (formulation obtained from [10] Eqs. (7.33)-(7.38), (7.40)). The expressions below have been modified by substituting the variable $s = x/R$ into the version used by A. Leissa [10]. The tree equations represent a system of coupled partial differential equations whereby R resembles the radius of the tube, ν the Poisson's ratio, E the Young's Modulus and h the thickness of the shell. Cylindrical coordinates θ, r and x are used to describe the displacement field $\vec{u} = [u, v, w]^T$ oriented as shown in Figure 2.7.

$$\left[R^2\frac{\partial^2}{\partial x^2}+\frac{(1-\nu)}{2}\frac{\partial^2}{\partial\theta^2}-\rho\frac{(1-\nu^2)R^2}{E}\frac{\partial^2}{\partial t^2}+\kappa\frac{(1-\nu)}{2}\frac{\partial^2}{\partial\theta^2}\right]u(x,\theta,t)+ \tag{2.17}$$
$$\left[\frac{(1+\nu)\,R}{2}\frac{\partial^2}{\partial x\partial\theta}\right]v(x,\theta,t)+$$
$$\left[R\nu\frac{\partial}{\partial x}+\kappa\left(-R^3\frac{\partial^3}{\partial x^3}+\frac{(1-\nu)\,R}{2}\frac{\partial^3}{\partial x\partial\theta^2}\right)\right]w(x,\theta,t)=0$$

$$\left[\frac{(1+\nu)\,R}{2}\frac{\partial^2}{\partial x\partial\theta}\right]u(x,\theta,t)+ \tag{2.18}$$
$$\left[R^2\frac{(1-\nu)}{2}\frac{\partial^2}{\partial x^2}+\frac{\partial^2}{\partial\theta^2}-\rho\frac{(1-\nu^2)R^2}{E}\frac{\partial^2}{\partial t^2}+\kappa\frac{3R^2\,(1-\nu)}{2}\frac{\partial^2}{\partial x^2}\right]v(x,\theta,t)+$$
$$\left[\frac{\partial}{\partial\theta}-\kappa\frac{R^2(3-\nu)}{2}\frac{\partial^3}{\partial x^2\partial\theta}\right]w(x,\theta,t)=0$$

$$\left[R\nu\frac{\partial}{\partial x}+\kappa\left(-R^3\frac{\partial^3}{\partial x^3}+\frac{(1-\nu)\,R}{2}\frac{\partial^3}{\partial x\partial\theta^2}\right)\right]u(x,\theta,t)+ \tag{2.19}$$
$$\left[\frac{\partial}{\partial\theta}-\kappa\frac{R^2(3-\nu)}{2}\frac{\partial^3}{\partial x^2\partial\theta}\right]v(x,\theta,t)+$$
$$\left[1+\kappa\left(R^4\frac{\partial^4}{\partial x^4}+2R^2\frac{\partial^4}{\partial x^2\partial\theta^2}+\frac{\partial^4}{\partial\theta^4}\right)+\rho\frac{(1-\nu^2)R^2}{E}\frac{\partial^2}{\partial t^2}+\kappa\left(1+2\frac{\partial^2}{\partial\theta^2}\right)\right]w(x,\theta,t)=0$$

with $\kappa=\frac{h^2}{12\cdot R^2}$.

The coefficient κ represents the terms associated with the bending deformation of the shell. This can be confirmed by considering that the plate *membrane stiffness* $Eh/(1-\nu^2)$ yields the *plate bending stiffness* $D=Eh^3/12(1-\nu^2)$ when multiplied by $h^2/12$.[2] Consequently, it can be inferred that the shell theory equals the membrane theory when κ is set to zero [10].

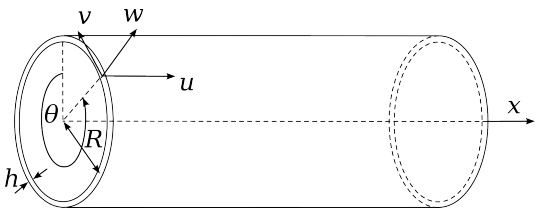

Figure 2.7: Coordinate system of closed cylindrical shell according to [10]

In [30] the stability of a shell was analysed, employing the *Flügge* shell theory as mentioned above. The model described in the paper considered the case of a moving oscillator which is running through a tubular shell embedded in an elastic half-space. In the paper, an indirect boundary element method (BEM) was applied to express the tube embedded in a soil layer through an equivalent elastic spring. The spring constant is dependent on the velocity and frequency of the object. To obtain this information, the Green's function for both the tube

[2]The membrane and plate bending stiffness are not present in this form since A. Leissa multiplies reformulated the equations which can be seen by the inertia term, which is $\rho h\ddot{w}$ in the original form

and the soil was computed, whereby the tube was solved by using a Fourier expansion in the circumferential direction and a Fourier transformation in both the space and time domains. It was noted in the paper that the instability is generally reached if the roots of the system cross the imaginary axis (positive real part, see Sec. 2.1.1). In this specific case it was found that at the onset of stability, the equivalent stiffness will reach a negative value, thus destabilising the system for small perturbations. To analyse the roots the D-decomposition was used over the parameters to find the stability regimes. In the paper, it was mentioned that only low-frequency vibrations of the oscillator are critical with respect to instability. On the other hand, high-frequency oscillations have stabilising effects on the system. This is due to the nature of anomalous Doppler waves. These waves are actively feeding energy back into the system, and are characterised by their negative frequency. Due to the oscillations of the object, the kinematic invariant shifts upward in the dispersion graph, making it more difficult to excite waves with negative frequencies. The absence of anomalous Doppler waves ensures the stability of a moving mass, rendering the system generally stable for "high-frequency" oscillations of the object. The paper highlighted that an increase in the system stiffness and damping makes it less susceptible to instability. An increase in soil damping, on the other hand, proved to have negative effects in some instances.

Another paper ([17]) investigated the dynamic stability of a tubular shell under the influence of a moving radial load. In that study, the elementary *Donnell-Mushtari* shell theory was used. The choice of this shell theory in combination with the axisymmetric load case enabled the elimination of the θ dependency altogether, significantly simplifying the governing equations. The study's novelty lies in examining the impact of periodically placed stiffeners along the shell on system stability. To facilitate the analysis of varying stiffness, a Finite Element Method (FEM) formulation was established. It was found in the study that periodic stiffeners are beneficial for stability as fewer zones of instability were found at subcritical velocities, compared to the uniform shell which was unstable for any velocity larger than the critical one (the speed of moving load is equal to the minimum wave speed of the system).

2.4.1. Stress resultants on a shell edge

To solve any differential equation, boundary and/or initial conditions need to be defined. In the case of mechanical systems, there are two main types of boundary conditions, the first one being *kinematic boundary conditions*, which give information about kinematic quantities (e.g., displacement, slope, etc.). The second type are *Neumann boundary conditions*, which are expressed in terms of stress resultants. For one-dimensional theories, such as the beam theory, the formulation of stress resultants which are then used in Neumann boundary conditions can be straightforward. For plates and shells, on the other hand, multiple factors play a role in formulating the stress resultants on the surface edges, such as the coupling between displacement fields through the *Poisson's ratio*.

For shell theories, there is an additional coupling between the membrane and bending forces (in and out-of-plane motion) through the curvature of the element itself. In [20] the equations were formulated for orthotropic carbon nanotubes comparing several thin shell theories, including the *Flügge* shell theory formulation. The derivation of the constitutive relation is also shown in [10], [11] and [23]. In the reviewed literature, the formulations were lacking transparency in the used shell theories, coordinate orientation and assumptions made throughout the modelling process. It was also found that supposedly equivalent theories seemed to not align in their expressions. For this reason, this thesis uses the expressions as shown in [11] and [21] as a reference.

The formulation of the curvatures varies between the different shell formulations as shown in [26], changing the stress formulations. In the following context, the constitutive relations are

going to be derived according to [11], starting from the strain on a shell edge and using linear elastic isotropic material and the plane stress assumption (see Eq. (2.23)) to relate strains to the stresses.

The strains in thin shells vary linearly according to the Love-Kirchhoff assumption, while out-of-plane shear deformation is neglected. However, in the *Flügge* formulation, displacement induces changes in curvature, necessitating its consideration in the formulation of stresses at the boundaries.

The strain consists of two components: a constant strain in the middle surface (membrane case) and a linear variation with thickness (shell bending case), dependent on the curvature and twist of the deformed shell. Notably, in the absence of curvature, the formulations would resemble those of plates. The strain expressions consistent with Flugge's thin shell theory for cylindrical shells are shown in Eqs. (2.20) - (2.22) below. Hereby ε_x represents the strain in the axial direction (along the tube), ε_θ the strain in the circumferential direction (around the perimeter) and $\gamma_{x\theta}$ the in-plane shear strain. The variable z indicates the distance perpendicular to the mid surface and runs therefore from $-h/2$ to $+h/2$, where h represents the thickness of the shell element. In thin shell theories, the strains vary linearly with an increase of $|z|$.

$$\varepsilon_x = \frac{1}{R}\frac{\partial}{\partial x}u(x,\theta) - \frac{z}{R^2}\left(\frac{\partial^2}{\partial x^2}w(x,\theta)\right) \tag{2.20}$$

$$\varepsilon_\theta = \frac{1}{R\,(R+z)}\left(-z\left(\frac{\partial^2}{\partial \theta^2}w(x,\theta)\right) + (R+z)\left(\frac{\partial}{\partial \theta}v(x,\theta)\right) + w(x,\theta)\,R\right) \tag{2.21}$$

$$\gamma_{x\theta} = \frac{1}{R^2\,(R+z)}\left(\left(-2Rz - z^2\right)\left(\frac{\partial^2}{\partial \theta \partial x}w(x,\theta)\right) + (R+z)^2\left(\frac{\partial}{\partial x}v(x,\theta)\right) + \left(\frac{\partial}{\partial \theta}u(x,\theta)\right)R^2\right) \tag{2.22}$$

According to the shell equations the stresses can be computed in the following manner, based on the material model (linear elastic, isotropic and plane stress; see Eq. (2.23)).

$$\begin{bmatrix}\sigma_x\\ \sigma_\theta\\ \sigma_{x\theta}\end{bmatrix} = [C]\begin{bmatrix}\varepsilon_x\\ \varepsilon_\theta\\ \gamma_{x\theta}\end{bmatrix} = \frac{E}{1-\nu^2}\begin{bmatrix}1 & \nu & 0\\ \nu & 1 & 0\\ 0 & 0 & (1-\nu)/2\end{bmatrix}\begin{bmatrix}\varepsilon_x\\ \varepsilon_\theta\\ \gamma_{x\theta}\end{bmatrix} \tag{2.23}$$

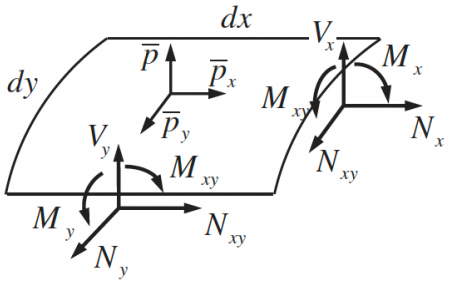

Figure 2.8: Stress resultants on edges of a cylindrical shell element. The y coordinate shown in the Figure is equivalent to theta used in the formulations above [23]

From the formulation, it can be seen that the stress in the axial and circumferential direction is not dependent on the shear deformation. The stress resultants on a cylindrical shell edge can now be obtained through an integration over the thickness of the element.

$$N_x = \int_{-h/2}^{h/2} \sigma_x \left(1 + \frac{z}{R}\right) dz \tag{2.24}$$

$$N_{x\theta} = \int_{-h/2}^{h/2} \sigma_{x\theta} \left(1 + \frac{z}{R}\right) dz \tag{2.25}$$

$$M_x = \int_{-h/2}^{h/2} \sigma_x \left(z + \frac{z^2}{R}\right) dz \tag{2.26}$$

$$M_\theta = \int_{-h/2}^{h/2} \sigma_\theta \left(z + \frac{z^2}{R}\right) dz \tag{2.27}$$

$$M_{x\theta} = \int_{-h/2}^{h/2} \sigma_{x\theta} \left(z + \frac{z^2}{R}\right) dz \tag{2.28}$$

The out-of-plane shear force Q_x can be computed based on an equilibrium equation [23].

$$\frac{\partial M_x}{\partial x} + \frac{1}{R}\frac{\partial M_{x\theta}}{\partial \theta} - Q_x = 0 \tag{2.29}$$

2.4.2. Circumferential modal expansion

To reduce the computational complexity and facilitate analytical or semi-analytical solutions, a discretisation technique in the circumferential direction can be employed. This method has been effectively utilized in various studies, including [18], [22] and [26], particularly in analyzing the dynamic behaviour of cylindrical shells. In these investigations, the cylindrical cross-section was represented using a truncated Fourier expansion, incorporating a finite number of circumferential wavenumbers. Although Finite Element discretisation along the pipe was adopted (commonly referred to as the semi-analytical Finite Element approach; SAFE), the discretisation technique utilizing a linear combination of harmonics is equally suitable for analytical or semi-analytical formulations. The Fourier expansion facilitates the representation of circumferential/cross-sectional behaviour through a series of harmonics, each multiplied by space and time-dependent coefficients. This formulation, as seen in equations derived from [18] and [26], involves the inclusion of N_h harmonics, where increasing this number enhances the accuracy of the model, analogous to refining the mesh in Finite Element analysis. To get an exact solution N_h would have to approach infinity but computational limitations require a truncation even after a few harmonics.

Notably, harmonics with $n > 1$ are indispensable for accurately capturing cross-sectional behaviour, their necessity contingent upon factors such as boundary conditions, dimensions, and applied load configurations. The adequacy of the selected number of modes varies accordingly to ensure the desired level of precision in the analysis. The formulation shown in Eq. (2.30) below shows the full form of the circumferential modal expansion. In this form, u represents the axial motion, v is the tangential motion and w is the radial motion of a shell element according to the definition shown in Figure 2.7. N_h represents the highest circumferential mode that is included in the Fourier expansion; all modes from 0 to N_h are considered in the analysis. The subscript 0 indicates the wave amplitudes corresponding to the circumferential mode $n = 0$. Analogous the subscript n indicates the wave amplitude corresponding to the "n-th" mode shape. The symbols c and s mark the amplitudes for the cosine and sine terms respectively.

$$u(x,\theta,t) = u_0(x,t) + \sum_{n=1}^{N_h} u_{c,n}(x,t)\cos(n\theta) + u_{s,n}(x,t)\sin(n\theta) \tag{2.30}$$

$$v(x,\theta,t) = v_0(x,t) + \sum_{n=1}^{N_h} v_{c,n}(x,t)\cos(n\theta) + v_{s,n}(x,t)\sin(n\theta)$$

$$w(x,\theta,t) = w_0(x,t) + \sum_{n=1}^{N_h} w_{c,n}(x,t)\cos(n\theta) + w_{s,n}(x,t)\sin(n\theta)$$

2.4.3. Modeshapes of finite circular shells

Similar to rectangular plates, circular shell vibration modes are characterized by two distinct wavenumbers, corresponding to each coordinate direction. In the case of circular shells, a distinction is often made between shell modes (circumferential modes) and beam modes (longitudinal modes) [10]. The latter is termed as such because they exhibit similarities to modeshapes derived for one-dimensional (1D) elements. As depicted in Figure 2.9, the circumferential mode $n = 0$ resembles a "breathing" motion, signifying constant expansion or contraction of the cross-section and no variation in θ direction. Modes with $n = 2$ and higher denote the number of complete sine/cosine waves within one revolution, resulting in symmetric modes for even circumferential wave numbers and anti-symmetric modes for odd ones. Notably, special attention should be given to modeshape $n = 1$, which closely resembles a modeshape one would obtain for a beam element. This mode exhibits no cross-section deformation but rather pure translation. Figure 2.9 illustrates various shell vibration modes, showcasing the diversity of behaviour exhibited by circular shells under dynamic loading conditions.

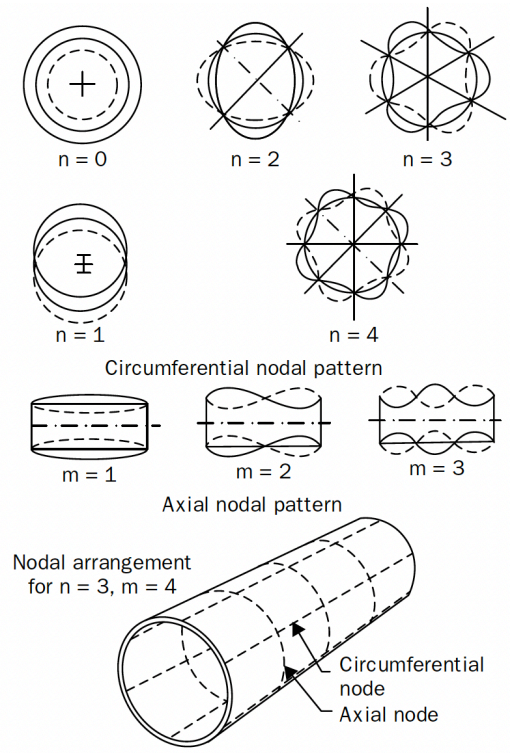

Figure 2.9: Shell vibration modes for a closed finite cylindrical shell [10]

3

Modelling of the Hyperloop Guideway

3.1. Description of the Model and solution method

In the course of the literature review, it was discovered that the dynamics of moving loads on tubular shells have not been extensively studied in the past. This study introduces novelty by transitioning from the well-established one-dimensional beam theories to the more sophisticated shell theory. The model consists of an infinitely long tubular shell supported by a continuous viscoelastic foundation along the bottom of the tube. The properties of this foundation are adjusted to mimic the characteristics of a discretely supported system by distributing the stiffness uniformly along each tubular element. Even though it is known that the results would be different both qualitatively and quantitatively between the continuous and discretely supported system [6], the limited scope of this thesis allows only an analysis of the former case.

The structure is subjected to a single lumped mass moving at a constant speed v_0, connected to the structure via an attracting electromagnetic force. This section derives the equations for an arbitrary force and subsequently analyzes the steady-state response of the system under a constant load, neglecting the interaction between the vehicle and the guideway. The effects of the suspended mass, including the electromagnetic force, are examined in Chapter 4. The model does not account for aerodynamic forces on the vehicle but does consider the impact of the pressure difference between the inside and outside of the tube on the structural dynamics. Other external factors, such as thermal expansion, wind, and snow loads, are not considered in this research.

Figure 3.1 provides an overview of the structural scheme. The governing equations, based on the *Flügge* shell theory for cylindrical shells, as introduced in Section 2.4 are adjusted to resemble the posed problem and can be seen in Section 3.2.

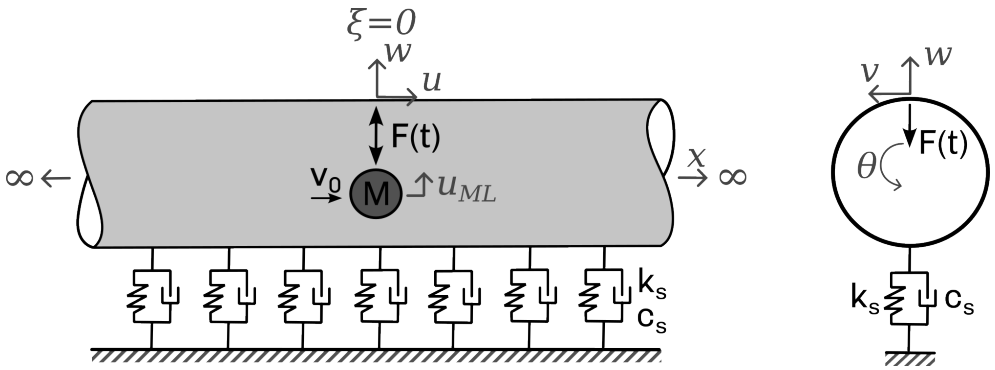

Figure 3.1: Overview of the problem analysed in this thesis

This section is dedicated to obtaining the steady-state response of the system. Given the need to analyze dynamic stability while properly accounting for vehicle-structure interaction, it is helpful to derive the Green's function for the system. Therefore, this section also outlines the steps necessary to obtain the Green's function.

The formulations for the shell theory are mathematically two-dimensional in space and dependent on time. To solve these equations analytically, a Fourier expansion in the circumferential direction is employed to express the cross-sectional variation of the displacement as a superposition of circumferential modes. Subsequently, the system is transformed into the Laplace-wavenumber domain, where it can be solved for a moving unit impulse load, thereby obtaining the Green's function of the system. The corresponding Green's function in the space-time domain is computed by numerically applying the inverse Laplace transformation.

Solving the system in this manner allows determination of the response to an arbitrary force through the convolution integral of the Green's function with the force. This method relies on the superposition principle, assuming the linearity of the guideway. It is important to note that despite the linearity assumption for the guideway, the non-linear interaction between the vehicle and the structure can still be captured through the time dependency of the vehicle and the beam. Consequently, the interaction force is both time- and state-dependent. More details about the interaction can be found in Chapter 4.3.

3.2. Governing equations in the space-time domain

The equations of motion according to the *Flügge* shell theory for an arbitrary load can be found in Section 2.4. For moving load problems it is advantageous to introduce the moving reference frame at the location of the moving load under the assumptions $\xi = x - V_0 t,\ \tau = t$. It has to be mentioned that the introduction of the new variables will introduce extra terms in the equation of motion due to the dependency of ξ on time. The following equations (Eqs. (3.1) -(3.3)) describe the displacement field of the shell in the moving reference system subject to an arbitrary moving point load as shown in Figure 3.1.

$$\left[R^2\frac{\partial^2}{\partial\xi^2}+\frac{(1-\nu)}{2}\frac{\partial^2}{\partial\theta^2}-\rho h\Lambda\left(\frac{\partial^2}{\partial\tau^2}-2\cdot V_0\frac{\partial^2}{\partial\xi\partial\tau}+V_0^2\frac{\partial^2}{\partial\xi^2}\right)+\kappa\frac{(1-\nu)}{2}\frac{\partial^2}{\partial\theta^2}\right]u(\xi,\theta,\tau)+ \tag{3.1}$$
$$\left[\frac{(1+\nu)\,R}{2}\frac{\partial^2}{\partial\xi\partial\theta}\right]v(\xi,\theta,\tau)+$$
$$\left[R\nu\frac{\partial}{\partial\xi}+\kappa\left(-R^3\frac{\partial^3}{\partial\xi^3}+\frac{(1-\nu)\,R}{2}\frac{\partial^3}{\partial\xi\partial\theta^2}\right)\right]w(\xi,\theta,\tau)=0$$

$$\left[\frac{(1+\nu)\,R}{2}\frac{\partial^2}{\partial\xi\partial\theta}\right]u(\xi,\theta,\tau)+ \tag{3.2}$$
$$\left[R^2\frac{(1-\nu)}{2}\frac{\partial^2}{\partial\xi^2}+\frac{\partial^2}{\partial\theta^2}-\rho h\Lambda\left(\frac{\partial^2}{\partial\tau^2}-2\cdot V_0\frac{\partial^2}{\partial\xi\partial\tau}+V_0^2\frac{\partial^2}{\partial\xi^2}\right)+\kappa\frac{3R^2\,(1-\nu)}{2}\frac{\partial^2}{\partial\xi^2}\right]v(\xi,\theta,\tau)+$$
$$\left[\frac{\partial}{\partial\theta}-\kappa\frac{R^2(3-\nu)}{2}\frac{\partial^3}{\partial\xi^2\partial\theta}\right]w(\xi,\theta,\tau)=0$$

$$\left[R\nu\frac{\partial}{\partial\xi}+\kappa\left(-R^3\frac{\partial^3}{\partial\xi^3}+\frac{(1-\nu)\,R}{2}\frac{\partial^3}{\partial\xi\partial\theta^2}\right)\right]u(\xi,\theta,\tau)+ \tag{3.3}$$
$$\left[\frac{\partial}{\partial\theta}-\kappa\frac{R^2(3-\nu)}{2}\frac{\partial^3}{\partial\xi^2\partial\theta}\right]v(\xi,\theta,\tau)+$$
$$\left[1+\kappa\left(R^4\frac{\partial^4}{\partial\xi^4}+2R^2\frac{\partial^4}{\partial\xi^2\partial\theta^2}+\frac{\partial^4}{\partial\theta^4}\right)+\rho h\Lambda\left(\frac{\partial^2}{\partial\tau^2}-2\cdot V_0\frac{\partial^2}{\partial\xi\partial\tau}+V_0^2\frac{\partial^2}{\partial\xi^2}\right)+\right.$$
$$\left.\kappa\left(1+2\frac{\partial^2}{\partial\theta^2}\right)+\left(k_s+c_s\left(\frac{\partial}{\partial\tau}-V_0\frac{\partial}{\partial\xi}\right)\right)\delta(\theta-\pi)\Lambda\right]w(\xi,\theta,\tau)=-F_w(\tau)\,\delta(\xi)\delta(\theta)\Lambda$$

with $\kappa=\frac{h^2}{12\cdot R^2}$ and $\Lambda=\frac{R^2\left(1-\nu^2\right)}{Eh}$

The coefficient Λ resembles a factor that Leissa A. used to simplify the form of the equations to the one presented in [10] and [11]. This needs to be taken into account whenever additional terms such as external forces or foundation terms are added to the equations. In alternative formulation as shown in [21] (Eqs. 2.3a-2.3c), this is not the case.

This problem will be solved by employing wavenumber integration, thus no interface conditions have to be used. In case the alternative solution method was to be used which uses the roots/poles of the system to assemble the displacement field as a summation of finite harmonics, see the derivation shown in Appendix A. This method was not used since it posed significant problems concerning computational expense, since the present root solver algorithms are inefficient to be utilised for the present system configuration. To derive the dispersion relation, the system is analysed without imposing any boundary or interface condition.

3.2.1. Circumferential projection

To remove the dependency on the circumferential direction, each of the equations can be projected on a finite set of circumferential harmonics. Substituting the Fourier series as indicated in Eq. (2.30) into the governing equations Eqs. (3.1) - (3.3), multiplying with a specific harmonic and integrating over the length of the modeshape (the circumference in this case) projects the equations onto the harmonic it was multiplied with. This effectively "filters" out the terms containing one specific term by using the following properties of the sine and cosine waves. This process will be referred to as "projection" in the remainder of the thesis.

$$\int_0^{2\pi}\sin(n\theta)\cdot\sin(m\theta)\;d\theta=\begin{cases}\pi, & n=m\\ 0, & n\neq m\end{cases} \tag{3.4}$$

In principle, this method is modal superposition whereby the modes are decoupled through their orthogonality. In the case of an infinite shell, modes are only present in the circumferential direction; along the shell, waves are described as waves per unit length i.e. through wavenumbers.

The combination of even and uneven order derivatives with respect to θ in the Eqs. (3.1) - (3.3) make it impossible to decouple the cosine and sine terms for the circumferential modes with $n>0$. This means that any system that uses this shell theory is inherently partially coupled. In this case, partially coupled means coupled within one projection. In other words, the solution obtained from the projected terms onto mode n is independent of the one obtained from mode m and can simply be superimposed based on Eq. (2.30).

Foundation and forcing term

The additional term describing the viscoelastic foundation in the EOMs is composed of two parts one dedicated to the spring and another one to the damping of the foundation. The

foundation is coupled with the displacement of the shell at a specific location, in this case at the bottom of the tube along the whole length (see Fig. 3.1). Eq. (3.5) shows exemplary the projection for the elastic part of the foundation term. Note that the projection requires a division over the interval, which is 2π for the constant terms and π for the trigonometric function. In the expression, the Dirac-delta function is used to evaluate the displacement at the desired location, which inevitably couples all of the circumferential modes due to its sifting property [1]. Consequently, the system matrix will not be diagonal as cross-coupling terms between the various modes will appear in the off-diagonal parts of the matrix. Therefore, the whole system has to be solved at once to obtain the wave amplitudes and not per mode as it would be possible in conventional modal superposition. The coupled system is of the size $3(1+2N_h)$, representing all the terms introduced by the Fourier expansion shown in Eq. (2.30).

$$\frac{1}{\pi}\int_0^{2\pi}(k_s \cdot w_n \cdot \cos(n\theta)\delta(\theta-\pi))\cos(m\theta)d\theta = \frac{1}{2\pi}k_s \cdot w_n \cdot \cos(n\pi)\cos(m\pi) \tag{3.5}$$

In the present problem configuration, the load is applied at $\theta = 0$ and the foundation at $\theta = \pi$. This means that the sign for the external force remains unchanged when projected onto the various circumferential modes since $\cos(n\theta)$ evaluated at $\theta = 0$ will be one regardless of the mode. For the foundation term, on the other hand, this is no longer the case as $\cos(n\pi)$ is negative when n is odd and positive when even. Eq. (3.5) shows that the signs in the term change based on combinations of n and m. If one is odd and the other one even the resulting term will be negative. In case both are even or odd, the term has a positive sign.

Symmetric response

To reduce the size of the system matrix the symmetry of the structure with respect to loading as well as the geometrical properties, can be used since symmetric loads on symmetric systems can only excite symmetric responses. This knowledge about the structural response allows a simplification of the Fourier expansion form Eq. (2.30) to the purely symmetric response as indicated in Eq. (3.6) assuming the origin of the θ coordinate is on the top or bottom of the tube.

The case $n = 0$, is a special one since the tangential displacement component with the wave v_0 describes a purely torsional motion of the shell. Such a motion cannot be excited by the loading configuration of this problem and can therefore be excluded in the circumferential expansion right away. The size of the coupled system can now be reduced from $3 + 6N_h$ to $2 + 3N_h$, since all the sine terms and v_0 drop out.

$$\begin{aligned} u(\xi,\theta,\tau) &= u_0(\xi,\tau) + \sum_{n=0}^{N_h} u_{c,n}(\xi,\tau)\cos(n\theta) \\ v(\xi,\theta,\tau) &= \sum_{n=0}^{N_h} v_{s,n}(\xi,\tau)\sin(n\theta) \\ w(\xi,\theta,\tau) &= w_0(\xi,\tau) + \sum_{n=0}^{N_h} w_{c,n}(\xi,\tau)\cos(n\theta) \end{aligned} \tag{3.6}$$

[1] It is worth mentioning that in case a uniformly distributed spring foundation would be used, (ex. tube embedded in homogeneous soil) the system could be partially decoupled – the system could be solved in the same way as a free shell –, as the foundation term only appears in the projection onto the circumferential mode $n = 0$. An embedded tunnel would be an example of such a case.

In any case, the projection onto the circumferential modes removes the θ dependency but on the other hand, leads to a growth of the system matrix, one set of governing equations for each harmonic considered in the modal expansion (N_h). Due to the reduction in computational cost, the assumption of symmetry as mentioned above will be used in further context. This also means that the model created in the course of this thesis is only applicable for symmetric loading and boundary conditions (symmetry around the axis running through $\theta = 0$ and $\theta = \pi$). The presented methods are applicable, irrespective of the assumption of symmetry.

The projection of the EOM onto an arbitrary mode n obtained by $1/2\pi \int_0^{2\pi} EOM_{u,w} d\theta$, $1/\pi \int_0^{2\pi} EOM_{u,w} \cdot \cos(n\theta) d\theta$ and $1/\pi \int_0^{2\pi} EOM_v \cdot \sin(n\theta) d\theta$. This operation will lead to the following set of equations, whereby the subscript c stands for the amplitude of the waves with the cosine and s for the ones with the sine terms. In the last EOM (Eq. (3.9)) it can be seen that the foundation introduces a coupling among all the circumferential modes.

$$\begin{aligned}
&\left[\frac{R^2\rho}{E}\left(\nu^2 v_0^2\frac{\partial^2}{\partial\xi^2} - 2\nu^2 v_0\frac{\partial^2}{\partial\xi\partial\tau} + \nu^2\frac{\partial^2}{\partial\tau^2} - v_0^2\frac{\partial^2}{\partial\xi^2} + 2v_0\frac{\partial^2}{\partial\xi\partial\tau} - \frac{\partial^2}{\partial\tau^2}\right) + \right. \\
&\left.\frac{n^2\left(\kappa\nu - \kappa + \nu - 1\right)}{2} + 2R^2\frac{\partial^2}{\partial\xi^2}\right] u_{cn}(\xi,\tau) \\
&\left[\frac{Rn}{2}\left(\nu\frac{\partial}{\partial\xi} + \frac{\partial}{\partial\xi}\right)\right] v_{sn}(\xi,\tau) + \\
&\left[\frac{R}{2}\left(-2\kappa\frac{\partial^3}{\partial\xi^3} + n^2\kappa\nu\frac{\partial}{\partial\xi} - n^2\kappa\frac{\partial}{\partial\xi} + 2\nu\frac{\partial}{\partial\xi}\right)\right] w_{cn}(\xi,\tau) = 0
\end{aligned} \tag{3.7}$$

$$\begin{aligned}
&\left[-\frac{Rn}{2}\left(\nu\frac{\partial}{\partial\xi} + \frac{\partial}{\partial\xi}\right)\right] u_{cn}(\xi,\tau) \\
&\left[\frac{R^2\rho}{E}\left(\nu^2 v_0^2\frac{\partial^2}{\partial\xi^2} - 2\nu^2 v_0\frac{\partial^2}{\partial\xi\partial\tau} + \nu^2\frac{\partial^2}{\partial\tau^2} - v_0^2\frac{\partial^2}{\partial\xi^2} + 2v_0\frac{\partial^2}{\partial\xi\partial\tau} - \frac{\partial^2}{\partial\tau^2}\right) + \right. \\
&\left.\frac{R^2}{2}\left(-3\kappa\nu\frac{\partial^2}{\partial\xi^2} + 3\kappa\frac{\partial^2}{\partial\xi^2} - \nu\frac{\partial^2}{\partial\xi^2} + \frac{\partial^2}{\partial\xi^2}\right) - n^2\right] v_{sn}(\xi,\tau) \\
&\left[\frac{R^2 n}{2}\left(-\kappa\nu\frac{\partial^2}{\partial\xi^2} + 3\kappa\frac{\partial^2}{\partial\xi^2}\right) - n\right] w_{cn}(\xi,\tau) = 0
\end{aligned} \tag{3.8}$$

$$\begin{aligned}
&\left[\frac{R}{2}\left(\kappa n^2\nu\frac{\partial}{\partial\xi} - 2R^2\kappa\frac{\partial^3}{\partial\xi^3} - n^2\kappa\frac{\partial}{\partial\xi} + 2\nu\frac{\partial}{\partial\xi}\right)\right] u_{cn}(\xi,\tau) + \\
&\left[\frac{R^2 n}{2}\left(\kappa\nu\frac{\partial^2}{\partial\xi^2} - 3\kappa\frac{\partial^2}{\partial\xi^2}\right) + 1\right] v_{sn}(\xi,\tau) \\
&\left[\frac{R^2\rho}{E}\left(-\nu^2 v_0^2\frac{\partial^2}{\partial\xi^2} + 2\nu^2 v_0\frac{\partial^2}{\partial\xi\partial\tau} - \nu^2\frac{\partial^2}{\partial\tau^2} + v_0^2\frac{\partial^2}{\partial\xi^2} - 2v_0\frac{\partial^2}{\partial\xi\partial\tau} + \frac{\partial^2}{\partial\tau^2}\right) + \right. \\
&\left.\left(R^4\kappa\frac{\partial^4}{\partial\xi^4} + n^4\kappa - 2n^2R^2\kappa\frac{\partial^2}{\partial\xi^2} - 2n^2\kappa + \kappa\right) + 1\right] w_{cn}(\xi,\tau) \\
&+ \frac{\Lambda}{\pi}\left(k_s + c_s\frac{\partial}{\partial\tau} - c_s v_0\frac{\partial}{\partial\xi}\right)\sum_{m=0}^{N_h} w_{cm}(\xi,\tau)(-1)^{n+m} = -F_{w,n}(\tau)\delta(\xi)\Lambda
\end{aligned} \tag{3.9}$$

The modal force $F_{w,n}$ in Eq. 3.9 includes the factor $1/2\pi$ if projected on $n = 0$ or $1/\pi$ if projected on $n > 0$.

3.3. Governing equations in the Laplace-wavenumber domain

The partial differential equations can be transformed into a set of algebraic equations by transforming the governing equations from the space-time domain into the Laplace– wavenumber domain. In this case, the Fourier transformation is applied over space and the Laplace transformation over time to include the effects of initial conditions. Commonly used is the following expression below, whereby $\bar{f}$ denotes an arbitrary function, k resembles the wavenumber and $s = \sigma + i\omega$ is the complex Laplace variable.

$$\hat{\bar{F}}(k,s) = \int_{-\infty}^{+\infty} \int_{0}^{+\infty} \bar{f}(\xi,\tau) \cdot e^{-ik\xi} \cdot e^{s\tau} d\tau d\xi \tag{3.10}$$

After substituting the above expression into the Eqs. (3.7) - (3.9) following the to procedure shown in Section 2.2.1. The equations below resemble the EOMs projected onto a harmonic n in the Laplace - wavenumber domain. By following this procedure, the partial differential equations were transformed into algebraic equations, whereby both k and s resemble running variables for the wavenumbers and frequency/Laplace variable respectively

$$\begin{aligned} &\hat{U}_{cn}\left(\frac{n^2\left(\nu-1+\kappa\nu-\kappa\right)}{2} - R^2k^2 + \frac{R^2\rho}{E}\left(-k^2\nu^2v_0^2 + k^2v_0^2 + 2ik\nu^2sv_0 - 2iksv_0\right.\right. \\ &\left.\left.+\nu^2s^2 - s^2\right)\right) + \hat{V}_{sn}\left(-\frac{inRk\nu}{2} - \frac{inRk}{2}\right) + \\ &\hat{W}_{cn}iR\left(-R^2k^3\kappa - \frac{n^2k\kappa\nu}{2} + \frac{n^2k\kappa}{2} - k\nu\right) = 0 \end{aligned} \tag{3.11}$$

$$\begin{aligned} &\hat{U}_{cn}iRkn\left(\frac{\nu+1}{2}\right) + \hat{V}_{sn}\left[-n^2 + R^2\left(\frac{3k^2\kappa\nu - 3k^2\kappa + k^2\nu - k^2}{2} + \right.\right. \\ &\left.\left.\frac{1}{E}\left(-k^2\nu^2\rho v_0^2 + k^2\rho v_0^2 + 2ik\nu^2\rho sv_0 - 2ik\rho sv_0 + \nu^2\rho s^2 - \rho s^2\right)\right)\right] + \\ &\hat{W}_{cn}n\left(\frac{R^2k^2\kappa\nu - 3R^2k^2\kappa}{2} - 1\right) = 0 \end{aligned} \tag{3.12}$$

$$\begin{aligned} &\hat{U}_{cn}iR\kappa\left(-R^2k^3 + \frac{n^2k\left(-\nu+1\right)}{2} - \frac{k\nu}{\kappa}\right) + \hat{V}_{sn}n\left(\frac{-R^2k^2\kappa\nu + 3R^2k^2\kappa}{2} + 1\right) + \\ &\hat{W}_{cn}\left[1 + R^2\left(R^2k^4\kappa + 2k^2n^2\kappa + \kappa n^4 - 2\kappa n^2 + \kappa + \frac{\rho}{E}\left(k^2\nu^2v_0^2 - k^2v_0^2 - 2ik\nu^2sv_0\right.\right.\right. \\ &\left.\left.\left.+2iksv_0 - \nu^2s^2 + s^2\right)\right)\right] + \frac{\Lambda}{\pi}\left(k_s + c_sikv_0 + c_ss\right)\sum_{m=0}^{N_h}\hat{W}_{cj}(-1)^{m+n} = -\hat{F}_{w,n}\Lambda \end{aligned} \tag{3.13}$$

3.4. Dispersion relation and shell modes

3.4.1. Dispersion relation for a free shell – uncoupled case

The purpose of this section is to explore the dynamic behaviour of the shell more thoroughly. To start off, the cylindrical shell itself will be analysed, neglecting the viscoelastic foundation, which allow to partially decouple the system and thus analyse each circumferential mode individually. The structure analysed in this thesis is only finite in its circumference which is why along the tubular shell modes cannot be defined as such, but rather expressed through wavenumbers. In other words, the wavenumbers m as shown in Figure 2.9, are not integers

representing the number of full waves in the system but expressed through the wavenumber k, resembling the number of full waves per unit length.

The dispersion relation is a key tool in analysing the nature of the waves present in the system. In an elastic mechanical system, it represents the relation between frequency and wavenumber, describing what frequency and wavenumber/ wavelength a wave in the system may have; in other words, which waves can exist in the system. The dispersion relation describes the property of the system itself and is independent of the load and other boundary conditions, thus $\hat{F}_{w,n} = 0$ in Eq. (3.13). This means that the moving reference frame as introduced in section 3.2, has to be omitted and a static reference frame introduced (substituting $v_0 = 0$ into the EOM). The dispersion relation can be obtained by applying the Fourier transformation over space and time or assuming a harmonic wave in space and time by substituting the following expression for an arbitrary wave $\bar{w}(x,t)$ into the EOM which have been projected onto a circumferential harmonic (Eqs. (3.1) - (3.3)):

$$\bar{w}(x,t) = \hat{\bar{W}} \cdot e^{i(\omega t - kx)} \tag{3.14}$$

In this equation $\hat{\bar{W}}$ represents an arbitrary wave amplitude and ω and k the frequency and wavenumber respectively. The result is equal to the Eqs. (3.11) - (3.13) If the foundation term is removed from the equations, the velocity is set to zero and $i\omega$ substituted for the Laplace variable s. To solve for the wavenumbers of the system, the roots have to be determined by setting the determinant of the system matrix to zero. When assuming symmetry, a polynomial of eighth order is obtained, leading to eight wavenumbers per frequency (six for $n = 0$). The dispersion relation Δ reads:

$$\Delta_n(\omega, k) = det\left([M_n(\omega, k)]\right) = 0 \tag{3.15}$$

In the expression above, the matrix M represents the systems matrix in frequency– wavenumber domain projected onto the circumferential mode n. Computing the wavenumber k based on an input frequency ω, or vice versa results in the dispersion relation Δ. The roots can only be determined by using numerical root solvers, consequently, no analytical expression for the dispersion relation can be obtained.

The dispersion curves for the first three circumferential modes are presented in Figure 3.2. The dispersion graphs for the modes $n = 3$ to $n = 6$ can be seen in Appendix C. Hereby, only the positive frequencies are shown as the dispersion graph would be symmetric around the x-axis in case of low damping. On the x-axis, there are the absolute values of the real and imaginary parts of the wavenumber plotted, whereby the imaginary part is displayed in the negative part of the x-axis for visual purposes. On the y-axis, on the other hand, the frequency is plotted in rad/s. This graph allows analysing the nature of roots in the system as it gives insights into the development of the real and imaginary parts of a specific branch of wavenumber. As mentioned before, there are eight wavenumbers for $n = 0$ and 16 for the other modes in case the symmetry condition is not applied. In the symmetric response, the number of wavenumbers reduces to six for $n = 0$ and eight for the remaining modes. Despite the number of roots, only four distinct wavenumbers with respect to their amplitude of real and imaginary parts were found for the projections on $n > 1$. The mode $n = 0$ does exclude the torsional wave in the symmetric case, thus only three branches are present in sub-figure (a). From the plots, it can be seen that in contrast to the beam theory, the cut-off frequency is not at $\omega = 0$, but rather at around 4000 rad/s. A similar shape of the dispersion curve can be obtained for a beam supported continuously on an elastic foundation. This similarity indicates that the membrane stiffness of the shell acts similarly as a spring foundation (displacement-dependent feedback). In other words, an infinitely small shell element is supported elastically by its neighbouring elements.

Below the cut-off frequency, the waves excited are purely *evanescent*, which can be seen by the large imaginary part in all the waves. Above the cut-off frequency, some waves carry way more propagation energy than their decay rate i.e. the real part is dominating. In the absence of damping, such waves would not decay but rather radiate with an unchanged amplitude and are therefore referred to as *propagating waves*.

Comparing the dispersion graphs for the different circumferential modes, it can be seen that the qualitative characteristics of the waves do not change much. Nevertheless, the cut-off frequency for branches 1 and 4 increases for larger circumferential modes. This indicates that propagating waves occur at higher frequencies for larger circumferential modes. From the dispersion graphs 3.2 (a) it can be seen that there is a strong resemblance between a beam model on an elastic foundation and the shell for branches 2 and 3 based on which it can be concluded that these branches are dominated by bending motion of the shell. Branch 1 on the other hand has similar characteristics to a rod and describes waves in the longitudinal direction. In sub-figure (b) branch 3 describes waves causing a twisting motion similar to a beam subject to torsion; this branch is not present at $n = 0$ as it resembles a uniform torsional motion of the shell, which is by definition anti-symmetric and was therefore excluded (see Sec. 3.2.1).

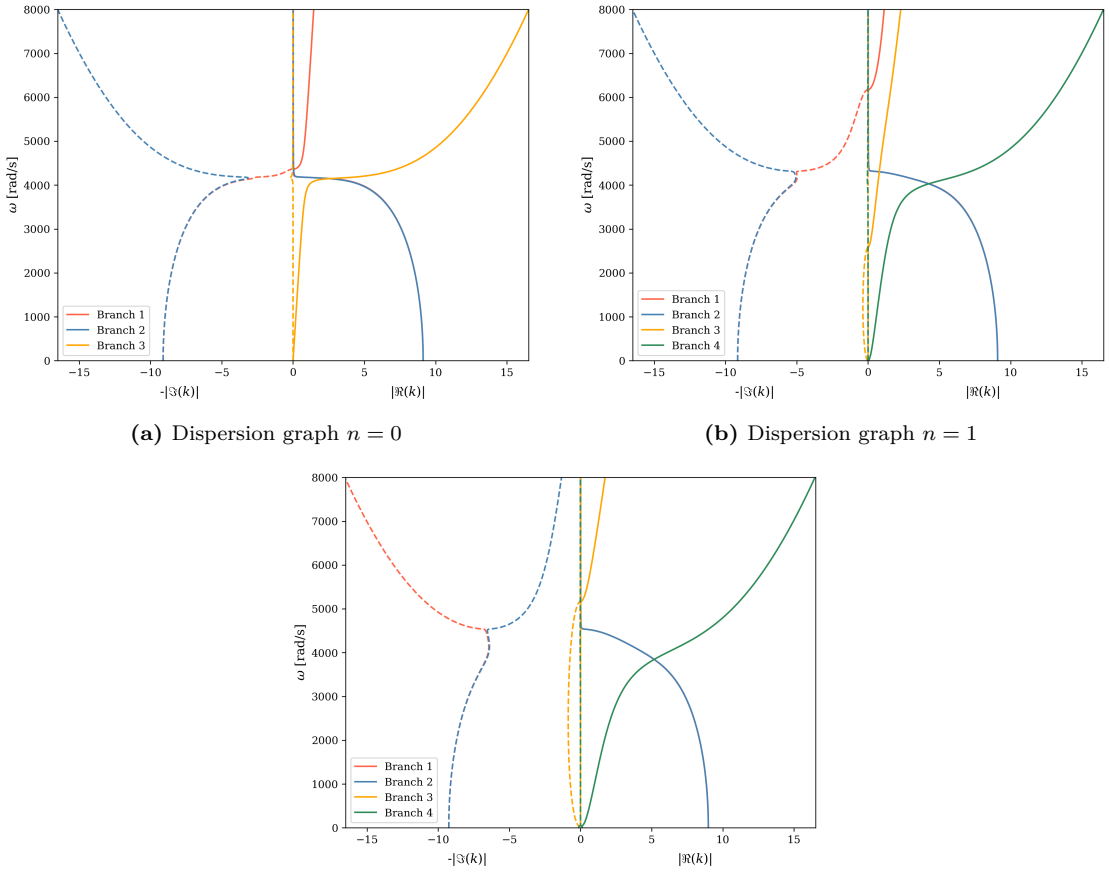

(a) Dispersion graph $n = 0$

(b) Dispersion graph $n = 1$

(c) Dispersion graph $n = 2$

Figure 3.2: Dispersion graphs of the first three circumferential modes for a free, closed, cylindrical shell

3.4.2. Dispersion relation for a shell on viscoelastic foundation – coupled case

While the uncoupled case allows a distinction between the various circumferential harmonics, the presence of the foundation couples all of those modes and therefore all of the roots have

to be solved at once. A dispersion curve is strictly speaking the relation between wavenumber and frequency in an undamped system. Therefore, the damping constant in the viscoelastic foundation was set to zero. The graph below (Fig. 3.3) resembles the dispersion relation for a coupled system with $N_h = 2$ ($n = 0$, $n = 1$ and $n = 2$). Despite the coupled nature of the system, the branches can still be assigned manually to specific circumferential modes in this case simply by finding the ones that resemble closest to the ones in the uncoupled case.

Also shown in the graph is the kinematic invariant ($k = \omega/v_0$), it resembles the moving vehicle at a constant velocity; the slope resembles the speed. In this case, the speed of the vehicle aligns with the phase velocity of a harmonic wave it excites; the vehicle is moving at the critical velocity of the system. This quantity divides the sub- and supercritical regimes and can be found iteratively by defining the kinematic invariant such that it meets the dispersion graph tangentially. In such a case the velocity of the vehicle aligns with the phase velocity of the excited wave. Each intersection between the dispersion graph and the kinematic invariant marks a wave that is excited by the load moving at that speed.

Comparing the uncoupled to the coupled case shows that the coupling introduced by the foundation has only minor effects on the system, as the dispersion curves as shown in Fig. 3.3 align overall almost perfectly. Nonetheless, there is an additional cut-off frequency introduced for the $n = 0$ and $n = 1$ branches for low frequencies. This shows that the foundation stiffness is causing the formation of this additional cut-off frequency, which consequently means the one at around 4000 rad/s is caused by the membrane stiffness as it is already present in the prior case (uncoupled case; without foundation term). For the $n = 2$ branches, this effect is not present which suggests that this mode does not greatly activate the spring foundation. It has to be mentioned that the large computational expense of computing the dispersion curves for the coupled case using complex root solver algorithms, made it infeasible to compute cases higher than $N_h = 2$. Consequently, it could be the case that coupling is more dominant in larger modes than it is for $n = 0$ to $n = 2$.

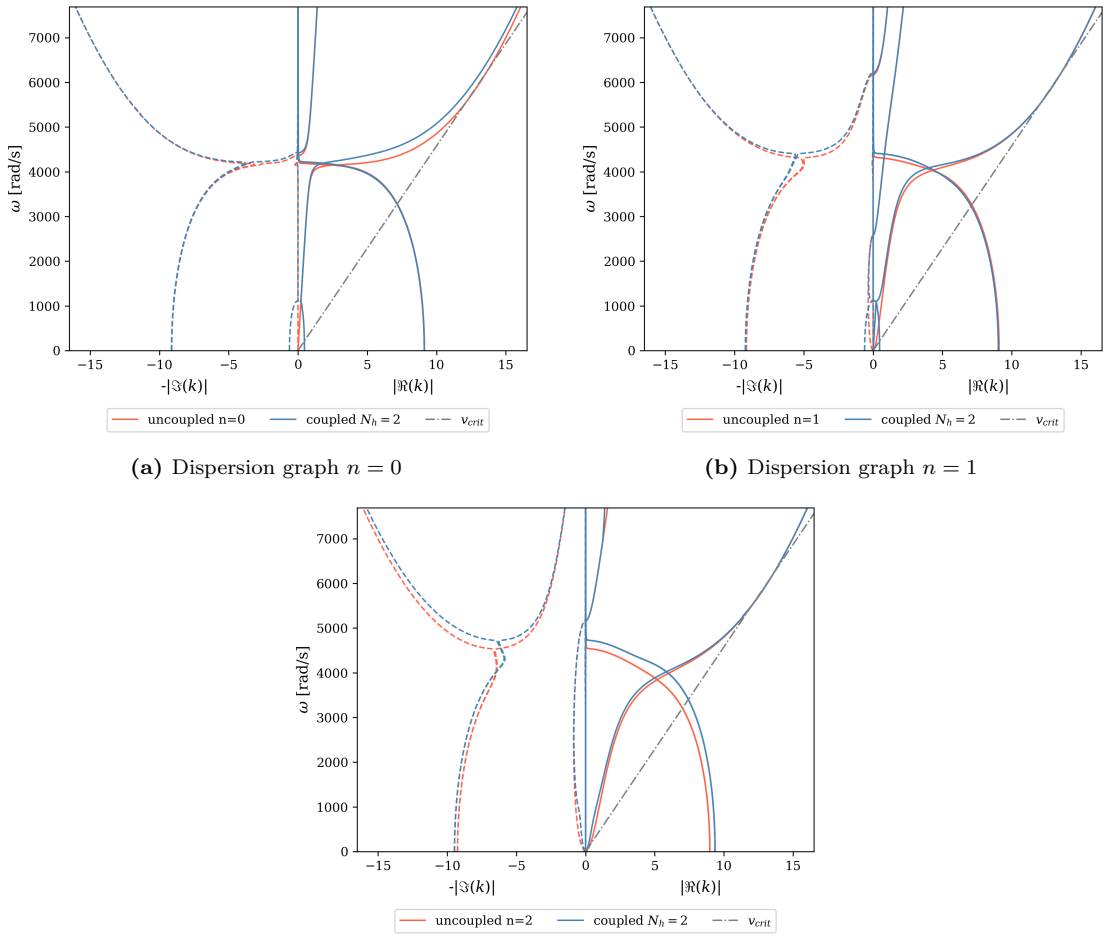

(a) Dispersion graph $n = 0$

(b) Dispersion graph $n = 1$

(c) Dispersion graph $n = 2$

Figure 3.3: Dispersion graph for a closed, cylindrical shell on an elastic foundation for the circumferential modes $n = 0$, $n = 1$ and $n = 2$; comparison to the uncoupled case

3.5. Wavenumber integration

The computational cost of searching for complex roots grows rapidly for an increase in the total number of circumferential modes considered N_h. The roots of the system are closely spaced with each other and the numerical round of errors in the computation of the determinant due to the LU decomposition make root solver routines such as *cxroots* inefficient and delicate. Further, the velocity of the moving load introduces an asymmetry in the roots such that any symmetry cannot be used to reduce computational time [2]. Throughout this thesis several approaches were analysed (graphical, Newton optimisation, adaptive initial guesses), but even advanced algorithms such as *cxroots* seem to have difficulties finding roots due to the properties inherent to this problem.

An alternative to the root-solving routine as shown in Appendix A is to compute the inverse Fourier transformation numerically which is referred to as wavenumber integration in the further context. The advantage is hereby, that the algorithm is not significantly affected by an increased number of circumferential modes. Henceforth, a more realistic model including more modes can be analysed. The response can be computed by evaluating the integral as shown in Eq. (3.16) for every frequency. In this expression $\vec{\mathbf{U}} = [U, V, W]^T$ marks the vector

[2] In case the dispersion curves are computed, the symmetry of the roots can be used as an initial guess in the complex root solving routine using *cxroots* to significantly reduce the computational time.

of complex wave amplitudes which are computed by inverting the system matrix numerically to solve the system of the form $[\mathbf{M}]\,\vec{\mathbf{U}} = \vec{\mathbf{f}}$, whereby $[\mathbf{M}]$ and $\vec{\mathbf{f}}$ represent the coupled system matrix and the external force vector composed of all the projected EOMs introduced in the Fourier expansion respectively. The individual wave amplitudes are then assembled based on the modal expansion in the circumferential direction as shown in Eq. (3.6). In contrast to the root-solving method, the domain does not have to be split at the interface and therefore no boundary or interface conditions need to be imposed. As a consequence, all the forces and other spatial features need to be considered in the EOM by making use of Heaviside or Dirac-Delta functions to spatially assign the components.

$$\vec{\mathbf{u}}(\xi, \theta, s) = \frac{1}{2\pi} \int_{-\infty}^{+\infty} \vec{\mathbf{U}}(\theta, s) \cdot e^{-ik\xi} dk \tag{3.16}$$

In the numerical implementation, the integral is evaluated for every Laplace variable, following the frequency resolution with accordance to the Nyquist sampling rate [3] ($df \leq \frac{1}{T_{max}}$) used in signal processing [2]. The wavenumbers need to be integrated over the whole domain, to have the complete representation of the spectrum, nonetheless in numerical applications fixed integration boundaries need to be set. These bounds need to be large enough to capture all the singularities i.e. the excited waves, of the spectrum. Due to the complex nature of the integrand/ wave amplitude, it is advisable to use an adaptive integration scheme which subdivides the domain at locations of local singularities to achieve the desired accuracy, instead of relying on conventional numerical integration algorithms with fixed bin widths [4].

3.6. Circumferential prestress due to vacuum

One of the key features of the Hyperloop system, and the one that distinguishes it from conventional Maglev trains, is that it operates in an environment of near vacuum, to eliminate aerodynamic drag. This section examines a method to capture the effects of pressure differences on the shell surfaces caused by low internal pressure with the model built in this thesis. It has to be mentioned that this cannot be considered in a beam model.

This preloading condition can either lead to an increase in fundamental frequencies in the case of tensile forces or decrease them when the system is under compression [12]. In the latter case, the system can also buckle at zero frequencies if the compressive force is sufficiently large [11]. As the interior of the tube is at 'vacuum' (leakage in the system will introduce a small amount of pressure), the pressure will be directed inwards of the tube (negative w direction) with a magnitude of 1 atmosphere (atm) assuming the system is at sea level. This will result in a compression force on the shell.

The effect of the vacuum can be accounted for through an initial membrane force. The equations of motion as shown in Eqs. (2.17) - (2.19) are already linearised and can therefore not capture the effects that such external loading conditions have. Introducing the external pressure in the linearised equations would be considered as a distributed force through a constant particular solution. This solution would be added to the homogeneous solution, creating a constant static offset in the displacements and thus not alter the dynamic response. For that reason, additional terms need to be introduced to the equations which are based on non-linear formulations. The required terms compliant with the *Flügge* thin shell theory used

[3] In this thesis a frequency step of $df = \frac{1}{2T_{max}}$ was used to avoid that the signal wraps around in the time domain such that the end of the signal has the same value as the start since the transient response of this problem is not periodic.

[4] In Python the adaptive quadrature function *quad* from the *scipy.integrate* package can be used. In that case is advisable to use $\pm$ *np.inf* as the integration bounds since it is not only more accurate but also more efficient than setting the boundaries to a fixed number which is large enough to capture the full wave spectrum. This is because *quad* sets the bounds automatically if infinity is set.

in this thesis can be found in [11] and are here shown in a slightly modified form for a uniform circumferential preloading condition, i.e. axial and torsional loading conditions are removed from the operator for brevity. Furthermore, the generalised variable $s = x/R$ was substituted such that the expressions read:

$$\frac{(1-\nu^2)N_\theta^i}{Eh}\left[\frac{\partial^2 u(\xi,\theta,\tau)}{\partial\theta^2} - R\frac{\partial w(\xi,\theta,\tau)}{\partial\xi}\right] \tag{3.17}$$

$$\frac{(1-\nu^2)N_\theta^i}{Eh}\left[\frac{\partial^2 v(\xi,\theta,\tau)}{\partial\theta^2} + \frac{\partial w(\xi,\theta,\tau)}{\partial\theta}\right] \tag{3.18}$$

$$\frac{(1-\nu^2)N_\theta^i}{Eh}\left[-R\frac{\partial u(\xi,\theta,\tau)}{\partial\xi} + \frac{\partial v(\xi,\theta,\tau)}{\partial\theta} - \frac{\partial^2 w(\xi,\theta,\tau)}{\partial\theta^2}\right] \tag{3.19}$$

The terms above are added to the equations of motion, whereby Eq. (3.17) - (3.19) correspond with the equations for u, v and w respectively. The initial membrane force caused by the external loading is considered in $N_\theta^i = -p_0 R$, where p_0 is the pressure difference between the inside and outside of the tube (1 atm in this case). If the external load causes a tensile force in the circumferential direction (force vector points outwards), the sign in N_θ^i needs to be changed.

The equations can be transformed into the Laplace-wavenumber domain and projected onto a circumferential mode in the same way shown in previous chapters for the EOMs. The resulting expressions after applying this transformation are omitted for brevity and shown in Appendix B.

3.7. Green's function of the system

The Green's function is typically a unit impulse response function, but in moving load scenarios, the impulse load is moving at a constant speed. Using the Green's function to solve differential equations relies on the superposition principle, making it inherently linear. By convolving the Green's function with the force in the time domain, one can obtain the response for any type of time-dependent loading (Eq. (3.20) [7], [27]). The term $w^{ic}(x,t)$ represents the free vibration of the guideway based on the system's initial conditions (static equilibrium position). This initial displacement is used to counter the transient effects that a load application on a system at rest has. It has to be added to the expression separately as the convolution integral captures the response for zero initial conditions [7].

$$w(\xi=0,t) = -\int_0^t f(\tau)\cdot G(\xi=0,t-\tau)d\tau + w^{ic}(\xi=0,t) \tag{3.20}$$

To obtain the Greens function, the coupled problem has to be solved for a unit load. In this project, this can be done by setting the force $F_w(\tau)$ in Eq. (3.13) to $-1\cdot\delta(\tau)$. The negative sign in the impulse function was introduced to displace the system in the positive radial coordinate direction ($+w$) since the EOMs were established based on the force orientation as depicted in Fig. 3.1, whereby the force vector points in the opposite direction of the positive coordinate. After expressing the system in the Laplace-wavenumber domain and applying the moving impulse load (assuming zero initial conditions) the system is solved and transformed into the space-frequency domain by applying the wavenumber integration as shown in Eq. (3.16). This enables evaluating the time response by computing the inverse Laplace transformation numerically according to Eq. (2.10).

For this project, only the Green's function for the radial displacement is of importance ie. $\hat{w}(\xi,\theta,s)$. Although the axial and tangential responses could be computed in the same manner,

they are not required anywhere in this thesis, as the electromagnetic force interaction depends solely on the vertical displacement of the tube. [5] Nonetheless, the fully coupled system has to be solved. For the vehicle-structure interaction, which will be more thoroughly explained in Chapter 4, the Green's function needs to be only evaluated at the point of action of the electromagnetic force. Since a single point of contact is assumed, the response needs to be computed for both ξ and $\theta = 0$; more specifically $\hat{w}(\xi = 0, \theta = 0, s)$. In further context, this specific function will be referred to as $\hat{g}_0(s)$ in frequency or $g_0(t)$ in the time domain (the hat symbol indicates that the quantity is in the frequency or Laplace domain).

The Green's function for this system is shown in Figure 3.4 (a), it is notable that the response is dominated by low-frequency oscillations except for the single peak at the cut-off frequency introduced by the membrane stiffness as shown in the dispersion graphs in Fig. 3.2. Sub-figure (b) shows that the total number of circumferential modes introduces low-frequency peaks after $N_h > 1$, suggesting that each of those peaks describes a wave dedicated to one of the shell bending modes ($n = 2$ and beyond) as shown in Fig. 2.9. From the plot of the Green's function, it can also be seen that the $n = 2$ is the mode with the lowest frequency and therefore the "softest" one. All the modes after that have a higher frequency but are still in the lower frequency spectrum and much softer than the membrane mode ($n = 0$) which has a frequency of approx. 4000 rad/s. It is worth mentioning that the decay of the Green's function with respect to frequency is comparatively low, necessitating the inclusion of frequencies beyond 15000 rad/s to fully reduce the offset in the time domain response.

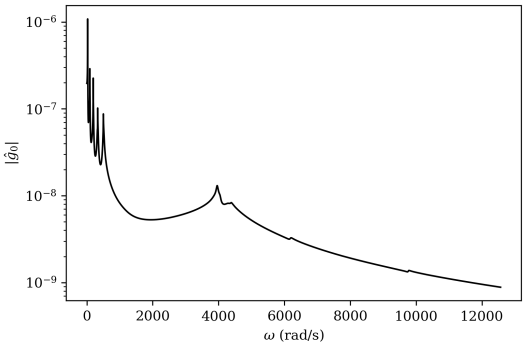

(a) Green's function in frequency domain for $N_h = 6$

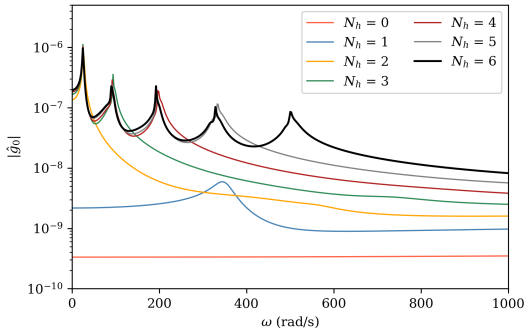

(b) Green's function in the frequency domain for varying N_h

Figure 3.4: Green's function in the frequency domain; changes in the low-frequency spectrum depending on the number of circumferential modes N_h.

3.7.1. Steady-state response due to a constant moving load

A steady-state response refers to the response of the system, where the transient effects inherent to the system are no longer present.

To derive the steady-state response of a system subject to a moving impulse load one can apply the Fourier transformation over time to obtain an algebraic equation which can be transformed into the following form:

$$\tilde{w}(\xi, \omega) = f(\xi, \omega) \cdot Q_0 \delta(\xi) 2\pi\delta(\omega) \tag{3.21}$$

Hereby f refers to the corresponding terms from the left-hand sight of the equation of motion. Q_0 represents the magnitude of the moving impulse load. Evaluating the equation at $\xi = 0$, applying the inverse Fourier transformation leads to the equation:

[5] It is worth mentioning that the longitudinal green's function could be used to investigate the effect of the acceleration and breaking of the vehicle.

$$\frac{1}{2\pi}\int \tilde{w}(\xi=0,\omega)e^{i\omega\tau}d\omega = \frac{1}{2\pi}\int f(\xi=0,\omega)\cdot Q_0 2\pi\delta(\omega)e^{i\omega\tau}d\omega \tag{3.22}$$

The sifting property of the Dirac-delta function applies when evaluating the integral, which results in an evaluation of the functions at $\omega = 0$. Therefore the exponent vanishes and the steady-state response reads:

$$w^{ss}(\xi=0,\tau) = Q_0 \cdot \tilde{w}(\xi=0,\omega=0) \tag{3.23}$$

In case of an oscillatory force with frequency Ω, the Dirac-delta function would have to be set to $\delta(\omega-\Omega)$. Hereby the sifting property causes an evaluation of the function for $\omega = \Omega$, which then leads to the steady-state response due to an oscillatory force.

3.8. Results and Analysis of the Guideway model

The following table summarises the parameters used by the reference case in this analysis, whereby the geometrical properties resemble the ones used in the European Hyperloop Center (EHC) and were provided by Hardt. Some of the parameters are being altered as a matter of the analysis. [6]

Table 3.1: Material Properties, Geometry, and Vehicle Parameters

Parameter	Value	Unit
Material Properties		
Steel Loss Factor	0.002	-
Young's Modulus of Steel (E_s)	210×10^9	$\mathrm{N/m^2}$
Density of Steel (ρ_s)	7850.0	$\mathrm{kg/m^3}$
Poisson's Ratio of Steel (ν)	0.3	-
Young's Modulus of Concrete (E_c)	50×10^9	$\mathrm{N/m^2}$
Density of Concrete (ρ_c)	2640	$\mathrm{kg/m^3}$
Geometry		
Tube Thickness (h)	16	mm
Outer Radius of Tube (R)	1.25	m
Column Diameter (d_{column})	1.0	m
Length of Column (L_{column})	5	m
Span	16	m
Foundation		
Foundation stiffness (k_s)	9.82×10^7	N/m/m
Foundation damping (c_s)	33498	Ns/m/m
Vehicle		
Critical velocity (v_{crit})	458	m/s

The critical velocity v_{crit} is not a predefined parameter but the result of the analysis of the dispersion relation for the present problem.

3.8.1. Model Validation using a FEM model – static case

This section will delve briefly into the results obtained from a FEM model built in the COMSOL FEM package. The aim is hereby to validate the results obtained from the semi-analytical model as described in this thesis, by comparing them to the ones from the FEM model. Hereby, only the radial displacement due to a static constant load is considered.

Model description

The model built in the FEM software has the same geometrical properties as the one in the semi-analytical model. The only difference is that the numerical model is finite in length. To still capture the behaviour of the infinitely long tubular shell, a boundary condition could be applied by using methods such as a perfectly matched layer (PML boundary). Since this is out of scope for this thesis, the length of the tube was chosen in such a way that the displacement due to the point load does not cause any deflection at the boundaries, in other words long

[6] The foundation stiffness was defined based on the stiffness of the column and reduced by a factor of 5 to account for the stiffness of the soil. $k_s = E_c A_{column}/(L_{column} \cdot span \cdot 5)$. The damping coefficient was determined based on the formulation of the critical damping for an SDOF system, whereby the damping ratio was set to 5e-2. The damping constant depends therefore also on the foundation stiffness and reads $c_s = 2\sqrt{k_s \cdot \rho_{mean}} \cdot$ 5e-2.

enough to approach the behaviour of an infinitely long shell. In this case, the tube needed to be approximately 100 m long to reach this state.

The model was subjected to a point load on the top of the tube with a magnitude resembling the suspended vehicle at rest. For the sake of simplicity, force was chosen to be both constant in space and time, consequently resembling a purely static case. The mesh had a resolution of 150mm and the analysis was geometrically non-linear for more reliable convergence.

Analysis and Interpretation

The comparison between the semi-analytical model and the solution obtained from the FEM model is summarised in Figure 3.5. Next to the comparison of the two models, the plot gives insights into the influence of the number of circumferential modes (N_h) on the static displacement. The modes $n = 0$ and $n = 1$ were not plotted in the graph since they are negligible in displacement magnitude and therefore to avoid clutter in the plot.

In the figure (Fig. 3.5), it can be seen that the cross-sectional behaviour of the tube is captured accurately after the number of circumferential harmonics is sufficient. Interestingly, the model built in this thesis overshoots the results obtained by the numerical model slightly when considering more than five modes – converging to a value larger than the FEM solution. This could be caused by the geometrical non-linear effect that is not considered in the semi-analytical modelling approach. Nevertheless, the results are of the same magnitude and qualitatively equivalent.

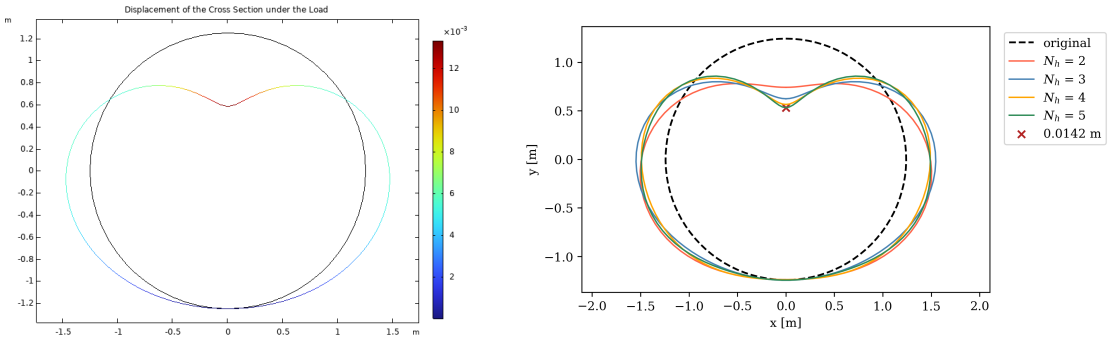

(a) FEM solution from COMSOL

(b) Semi-analytical model for various N_h

Figure 3.5: Comparison of cross-section displacement at $\xi = 0$ of the FEM solution and the semi-analytical model due to a static load.

Furthermore, in Figure 3.5 it can be seen that the foundation stiffness is significantly larger than the shell bending stiffness, judging by the difference in displacement magnitude. Due to the scaling of the displacement field, it seems as if there is no displacement at the bottom of the tube ($\theta = \pi$). Since the displacement is dominated by the bending deformation, the shell cross-section effectively ”decouples” the foundation from the vibrations occurring at the top of the beam. Consequently, the stiffness of the foundation is expected to not greatly influence the response of the system, hence explaining the similarity in dispersion curves between the coupled and uncoupled case (see Fig. 3.3). It has to be mentioned that this might only be caused by the limitations of this modelling approach rather than the reality. In case the tube would be supported at discrete locations instead of the continuous foundation used in this study, the ”beam modes” of the tubular shell (bending along the tube) might be activated more, hence showing larger displacement for $n = 0$ and $n = 1$. A similar effect could also occur, in case the bending stiffness of the shell wall increases by enlarging the thickness or reducing the radius of the tube, essentially bringing the foundation and the shell bending stiffness closer together.

To make judgements about the required amount of circumferential modes (N_h), the dis-

placement was computed for a static constant load for various N_h. The results of this analysis were summarised in the plot as shown in Fig. 3.6. Notable is the large increase in displacement amplitude when making the transition from $N_h = 1$ to $N_h = 2$. This jump occurs since $n = 2$ is the first 'shell mode' which describes waves leading to a cross-section deformation. Figure 3.5 shows clearly that the deformation of the cross-section dominates the response. In other words, the modes $n = 0$ and $n = 1$ describe the membrane and beam-like behaviour, which are much stiffer in this model configuration than the shell bending modes. An increase in the total number of circumferential modes increases the displacement which seems to converge when considering around $8 - 9$ modes. Nevertheless, there is no qualitative gain in the results when increasing the number of modes even further. As a result of the trade-off between accuracy and computational cost, $N_h = 6$ was chosen for further analysis.

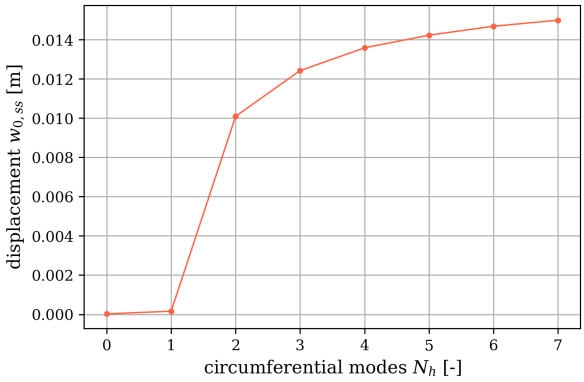

Figure 3.6: Influence of the number of circumferential modes N_h on the radial displacement w for for static constant load at $\theta = 0$ and $\xi = 0$

3.8.2. Effects of model parameters on the critical velocity

This section aims to shed light on the various model parameters and how they influence the steady-state response of the system, focusing on the variation in the critical velocity. The critical velocity refers in this context to the case at which the phase speed of the excited waves matches the velocity of the moving load. At that point, the waves are in phase which results in an amplification of displacement magnitude due to resonance. Furthermore, this parameter separates the system into a sub- and super-critical regime, whereby the former includes all the velocities from zero up to the critical velocity and the latter everything that lies beyond. It has to be mentioned that due to the various waves present in the system, visible by the various dispersion branches in Fig. 3.2, multiple critical velocities will be present in the system. Nonetheless, the one with the lowest velocity is the most important as the amplification will occur first and the most dominant.

In this thesis, there were two methods used to estimate the critical velocity of a linear system. The first one is using the dispersion graphs, whereby the kinematic invariant should meet the dispersion curves tangentially. This means that the phase velocity of the excited waves aligns with the velocity of the load (see the grey line in Fig. 3.3). The second method relies on the computation of the steady-state response for a varying velocity of the constant moving load. In such a plot the locations of large amplification indicate critical velocities. The latter approach, gives a more accurate representation of the occurrence of critical velocities, as the fully coupled problem is investigated and the interplay between the various waves is captured correctly.

In the following sections, multiple parameters and scenarios will be analysed as to how

they affect the dynamic amplification of the steady-state response with respect to the velocity of the moving load. Based on this, the effects of the parameters on the critical velocity can be investigated. This is important as it shows how certain parameters influence the response of the system which gives insights into the behaviour of the system and highlights potential limitations inherent to this modelling approach.

Extending the results from the previous section, the influence of the number of circumferential modes is once again studied for various velocities.

Furthermore, the effects of the foundation stiffness are analysed, which is important as it is the model parameter with the greatest uncertainty because it dominantly depends on the stiffness of the subsoil. In this model configuration, the stiffness of the column was used and distributed over the span of the tube, which assumes a rigid soil layer and is therefore unrealistic. To account for the stiffness of the subsoil, multiple reduction factors are investigated. Additionally, the influence of various tube spans can be evaluated, since this model parameter also influences the "equivalent" foundation stiffness; larger spans result in smaller spring stiffness and vice versa. It has to be mentioned that this is only the case for this model configuration with a continuously supported shell, as a model on discrete supports would change the frequency of periodic excitation instead of the foundation stiffness.

Finally, the effects of varying tube dimensions are analysed (i.e. wall thickness and diameter) since those parameters could potentially aid in enhancing the system performance concerning dynamic amplification as well as stability concerns. In practical applications, these parameters are determined with structural design requirements in mind, which depend on load, span, and foundation type (elevated tracks or submerged tunnels). Consequently, some combinations may not comply with the chosen spatial dimensions and vehicle weight, potentially leading to violations of design codes and regulations. However, this aspect will not be addressed in this thesis. Instead, the study is intended to provide an indicative analysis of how certain parameters influence the system's response, rather than serving as a reference for the design and optimization of Hyperloop guideways.

Influence of the number of circumferential modes on the critical velocity

Figure 3.7 compares the steady-state response due to a constant moving load for various numbers of circumferential modes used in the analysis (N_h). A significant jump in displacement is observed when transitioning to a model with $N_h = 2$, as it was observed already in the static case (see Fig. 3.6). However, models with only one or two circumferential modes, specifically $N_h = 0$ or $N_h = 1$, can still accurately approximate the system's critical velocity, despite differences in the overall response. Each additional mode introduced in the analysis results in a new peak or amplification in the supercritical regime. Although these peaks are of much smaller magnitude compared to the amplification at approximately 420 m/s, each represents a critical velocity associated with a specific mode. As previously inferred from the Green's function shown in Fig. 3.4, the modes from $n = 2$ onwards exhibit increased stiffness, leading to their critical velocity being higher. Each additional mode will introduce another resonance peak at supercritical velocities.

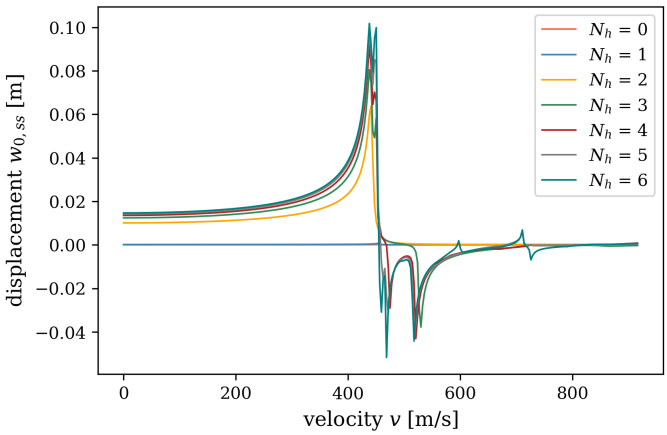

Figure 3.7: Influence of the number of circumferential modes N_h on the radial displacement – critical velocity

Influence of the Foundation on the critical velocity

In Figure 3.8 below, the effect of the foundation stiffness on the critical velocity is analysed by varying the reduction factor applied to the spring constant [7]. From the figure, it is evident that the variation of the foundation stiffness has negligible effects on the response at the point of load application. Only when reducing the stiffness by a factor of 200, minor quantitative changes in the critical velocity do arise. It can therefore be concluded that the localised displacement on the top of the tube caused by the low bending stiffness of the shell walls, is effectively decoupled from the displacement at the bottom. Consequently, the variation of the foundation term does not pose any significant changes to the response for this specific model configuration. A variation in the span will therefore not have significant changes and will not be further analysed. In case the model would consider the discrete foundation, both foundation stiffness and span are suspected to once again gain importance.

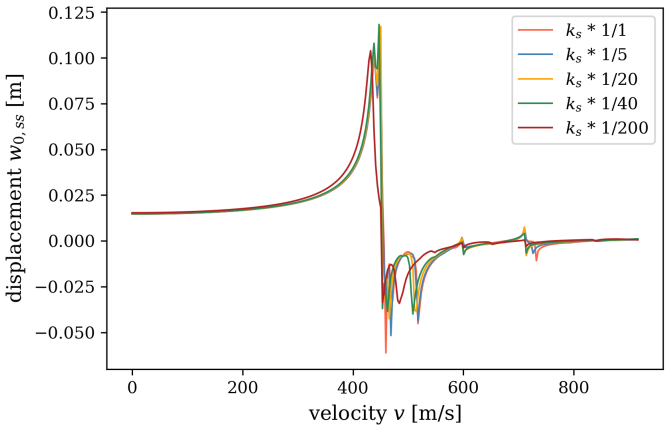

Figure 3.8: Influence of the foundation stiffness on the radial displacement – critical velocity

[7] In [7] the problem concerning the foundation stiffness was tackled by reducing the initial stiffness by a factor to match the quasi-static displacements of a FEM model on discrete supports. The foundation stiffness of the Euler-Bernoulli beam model was hereby tuned to match the displacements of a shell model, thus including the effects of the cross-section deformation. In that study the reduction factor for the foundation stiffness was 1/40 of the initial value.

Influence of tube dimensions on the critical velocity

To gain a better understanding of the effects of tube dimensions, the thickness and diameter are analysed separately by changing only one parameter at a time. In both scenarios, the dimensions of the reference case according to Tab. 3.1, were varied by approximately ±10%.

The graphs in Fig. 3.9 demonstrate that changes in either thickness or diameter significantly influence the structural response, unlike the foundation stiffness, which had negligible effects (see Fig. 3.8). Both thickness and diameter affect the critical velocity and the magnitude of the response. As expected, a larger diameter or smaller thickness leads to an increase in displacement amplitude and a decrease in critical velocity, both resulting in reduced system stiffness on a cross-sectional level. A smaller diameter increases the curvature and consequently activates more of the membrane action of the shell which is significantly greater than the bending stiffness (plate action). In a model configuration where the axial bending contribution is more dominant ($n = 1$ mode; beam-mode) compared to the circumferential bending modes ($n = 2$ and higher), an increased diameter is expected to increase the stiffness for those modes and consequently reduce the magnitude of displacement. In such a case the shell is also suspected to be more comparable to a beam model. This state could be achieved by changing the model configuration, for instance, by applying the load to the bottom of the tube to directly activate the foundation.

The responses shown in Fig. 3.9 are qualitatively similar in all cases, even though it is suspected that after a certain wall thickness, the shell bending modes will dominate the response less. It can be concluded that wave-induced instability under operational conditions could be mitigated by adjusting either parameter to effectively increase the critical velocity, ensuring the system operates at subcritical velocities.

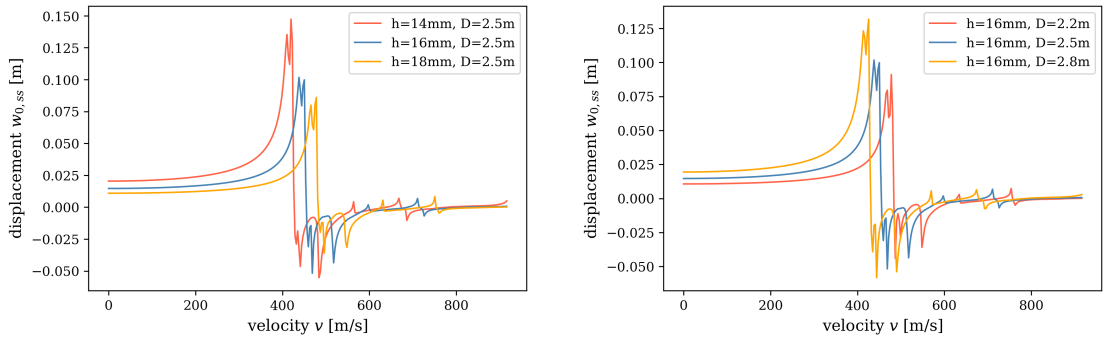

(a) Variation of tube thickness

(b) Variation of tube diameter

Figure 3.9: Effects of the variation of the tube diameter and thickness on the steady-state response of the system as well as the critical velocity

To further investigate the impact of the two parameters, the dispersion relation is used. Fig. 3.10 shows the effects of the parameters based on the dispersion graphs for the first three uncoupled modes. The figures reveal that the effects of these parameters are more complex than indicated in Fig. 3.9. Variations in thickness lead to an overall change in the wavelength for branches describing shell bending motion, while the branches for rod or axial wave propagation remain unchanged (see Fig. 3.10 (a)-(c)). Changes in diameter shift the dispersion graphs along the y-axis, causing a change in the cut-off frequency (see Fig. 3.10 (d)-(f)). This latter effect is similar to the dispersion graph of an Euler-Bernoulli beam on a Winkler foundation when the spring stiffness is adjusted, accordingly. Reducing the radius increases the stiffness of the shell wall in the circumferential direction, shifting the dispersion branches to higher frequencies. The former case on the other hand has the same effects on the dispersion graphs as an increase of the bending stiffness (EI) has for an Euler-Bernoulli beam.

It can be concluded that in shells of greater diameter, propagating waves occur at much lower frequencies. The changes in critical velocities shown in Fig. 3.9 align with the changes of the slope for the kinematic invariant to meet the main dispersion branch tangentially, which approximates the critical velocity.

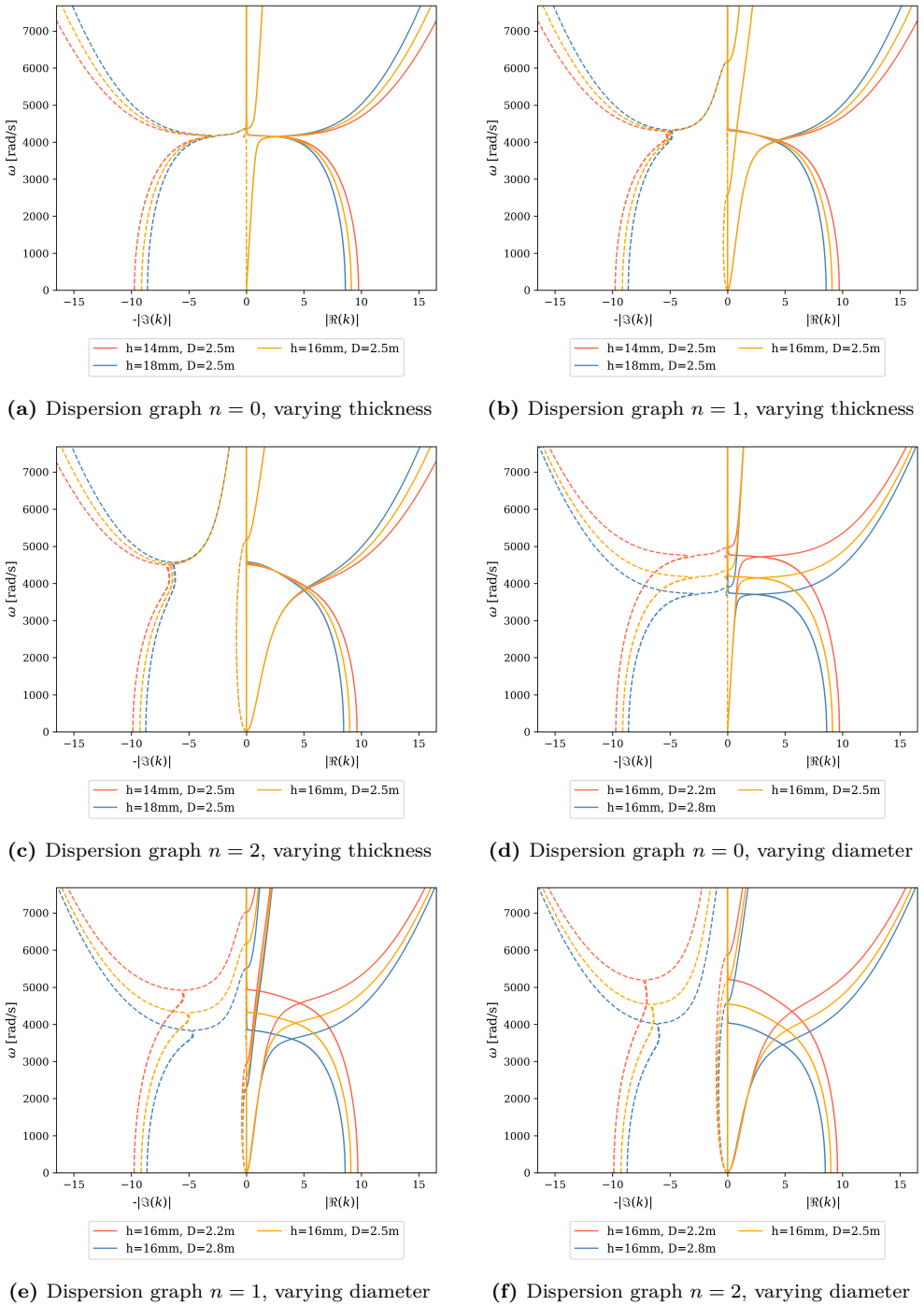

(a) Dispersion graph $n = 0$, varying thickness

(b) Dispersion graph $n = 1$, varying thickness

(c) Dispersion graph $n = 2$, varying thickness

(d) Dispersion graph $n = 0$, varying diameter

(e) Dispersion graph $n = 1$, varying diameter

(f) Dispersion graph $n = 2$, varying diameter

Figure 3.10: Variation in the dispersion graphs due to varying diameter and thickness; circumferential shell modes $n = 0$, $n = 1$ and $n = 2$ for the uncoupled system

To summarize the main findings of this section, it was found that the number of circumferential modes does not affect the lowest (main) critical velocity but introduces additional resonance peaks at supercritical velocities, each corresponding to a critical velocity linked to a

specific circumferential mode. Additionally, changes in the foundation stiffness do not significantly impact the system's response in the current problem configuration, as a result of the low bending stiffness of the shell wall and the continuous support. This leads to a minor activation of the *beam modes*. Lastly, it was shown that the critical velocity can be modified by adjusting the tube thickness or radius, while the overall response remains qualitatively unchanged. Increasing the diameter or reducing the thickness both result in a lower critical velocity and higher displacement due to reduced dynamic stiffness [8]. This allows a modification of the structure such that the system operates at subcritical velocities to avoid anomalous Doppler waves from being excited.

3.8.3. Variaton of the steady-state response across the cross-section

To expand on the insights of the shell dynamics from the previous sections, it is essential to not only look at the response at the point of contact but also the whole cross-section. Fig. 3.11 shows the steady-state response across the cross-section for various velocities as a surface plot. This plot is consequently an extension of the analyses presented in Sec. 3.8.2 in the circumferential direction θ.

In the plot, there is once again a clear distinction visible between the subcritical and supercritical regimes, divided by the resonance peak at $v/v_{crit} = 1$. In the subcritical regime, a quasi-static response dominates, which increases closer to the critical velocity due to resonance. Once the system operates at supercritical velocities, it undergoes resonance with various circumferential wave modes, each of which represents a critical velocity of the system. This is evidenced by the standing wave pattern, which shows an increasing number of fluctuations around the circumference as the velocity increases. This indicates once again that higher modes are stiffer and therefore amplified at higher velocities.

The plot also reveals that the radial displacement at the bottom of the tube ($\theta = \pm\pi$) remains close to zero across all velocities. This highlights once again that the influence of the foundation stiffness is not relevant to the dynamic response in this model configuration.

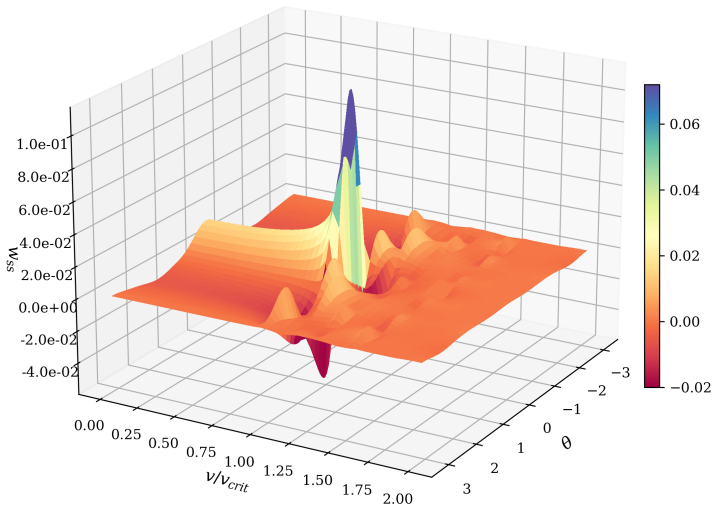

Figure 3.11: Variation of the steady-state response with respect to θ and velocity

Figure 3.12 shows the steady-state response of the cross-section at selected velocities. Hereby it is notable that the sub-critical response remains qualitatively unchanged, but rather

[8] In a beam model one would intuitively assume that an increased diameter increases the bending stiffness. In a shell on the other hand this is not the case if the deformation is dominated by shell wall bending modes, i.e. $n = 2$ and above

scales in magnitude with an increased velocity. In the supercritical regime, the response undergoes several modes of resonance with the circumferential modes. Having multiple critical velocities could cause the excitation of multiple anomalous Doppler waves which could feed energy back into the system and therefore lead to wave-induced instability.

These results show that a standing wave field in circumferential direction occurs after the critical velocity is surpassed which propagates as a flexural wave in the axial direction (along the tube). This wave in the axial direction is expected to be qualitatively similar to the one of a beam – shorter wavelength to the front and longer to the back (at supercritical velocities) – with the only difference that the wave is distributed in the circumferential direction as a standing wave.

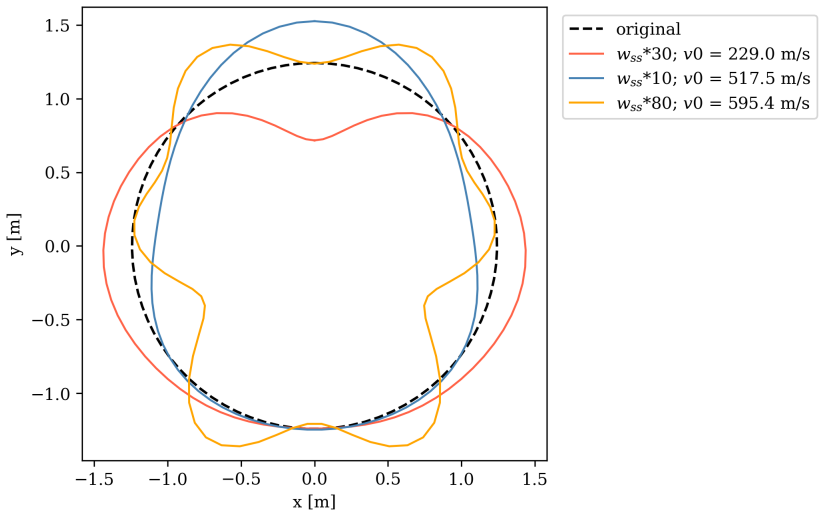

Figure 3.12: Variation of the steady-state response with respect to θ for $\xi = 0$ and $v0 = 0.5$,1.13,1.3 v_{crit}. Note that the displacement fields were scaled for graphical purposes.

3.8.4. Influence of the circumferential prestress caused by the low-pressure environment inside the tube

This section will highlight the changes in the steady-state response caused by the circumferential prestress due to the pressure difference between the inside and outside of the tube. As mentioned in Section 3.6, the force acting on the outer shell is assumed to be 1atm = 101325 N/m^2, creating a constant membrane compression force (prestress) on the system, thus referred as the pressurised case in further context. This compression is expected to significantly impact the results due to its large magnitude, shifting the dynamic response to lower frequency ranges and making the system potentially more prone to instability and dynamic amplification [11]. In [12] it is shown exemplary on a compressed EB beam that with an increase of a compression force, the stability of the system is impacted causing an exponential growth over time at lower velocities; the onset of instability occurs at lower velocities with an increase in compression force.

Figure 3.13 compares the Green's function for the pressurized and unpressurised cases. It can be seen that the low pressure in the tube results in a decrease in the response frequency, introducing a frequency shift of around 20 rad/s for the first five peaks (circumferential shell bending modes), while the peak at around 4000 rad/s remains unchanged ($v = 0.1\ v_{crit}$, i.e. subcritical velocity). The low-frequency waves dominate the system's response, evident from their large amplitude in the Green's function. Consequently, the response is expected to be qualitatively similar but of lower frequency. Notably, the peaks are slightly larger in

amplitude, especially at $\omega = 0$, where the difference is significant. This indicates that the static displacement is being amplified by the pressurized case, which is intuitive considering that a compressive force is applied to the tube, aiding the external load.

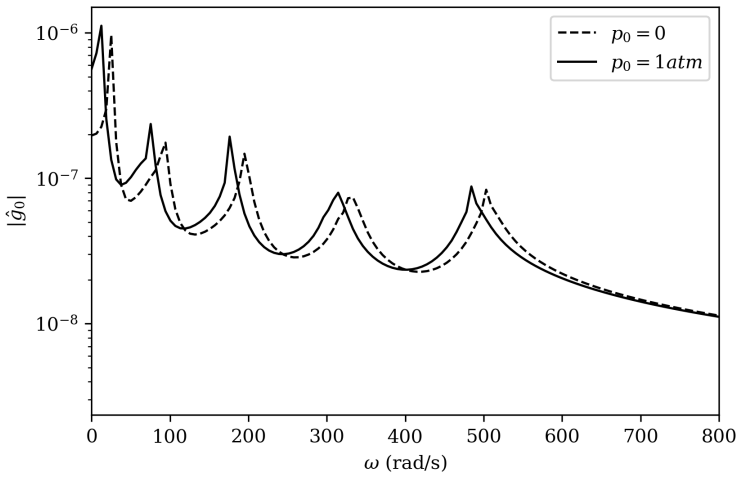

Figure 3.13: Effects of the prestress caused by the vacuum the inside of the tube on the Green's function $v = 0.1v_{crit}$

Figure 3.14 compares the steady-state responses for velocities up to twice the critical velocity, considering three pressure scenarios: no vacuum, half vacuum, and full vacuum (0.0, 0.5, and 1.0 atm). The figure shows that the overall response is larger in magnitude and qualitatively different across these scenarios. While the intermediate case (yellow curve) somewhat resembles the model which neglects vacuum effects, this similarity diminishes as the internal pressure decreases. Notably, the critical velocity shifts to lower values with decreasing internal pressure since that results in an increase in the prestress.

A Hyperloop system is expected to cruise at speeds of around $800 - 1000$ km/h ($220 - 280$ m/s) [9]. While the critical velocity for the reference case was approximated to be 458 m/s (obtained from the dispersion graphs in Fig. 3.3 and the steady-state response shown in Fig. 3.7) it reduces to 284 m/s when the external pressure is considered. The reduction of approximately 50% brings the system's operational conditions close to supercritical velocities. This means the system is not only subject to electromagnetic instability but also to wave-induced instability due to anomalous Doppler waves excited at supercritical velocities.

However, it should be noted that results might differ with a more realistic model that properly considers the internal rail and the discrete foundation. The periodic supports could introduce another instability phenomenon, namely *parametric instability*. Nonetheless, the negative effects on system stability are expected to persist even with these advanced modelling approaches. This means that the consideration of the pressure difference leads to a reduction of the critical velocity in any case.

To summarize, the effects of external prestress, whether caused by a difference in atmospheric or hydrostatic pressure inside and outside the tube or by constant soil pressure in the case of a submerged tunnel, lead to significant changes in the system's behaviour. These effects amplify with increasing pressure, resulting in larger deformations and lower critical velocities. Therefore, these preloading conditions should always be considered when developing models for such systems.

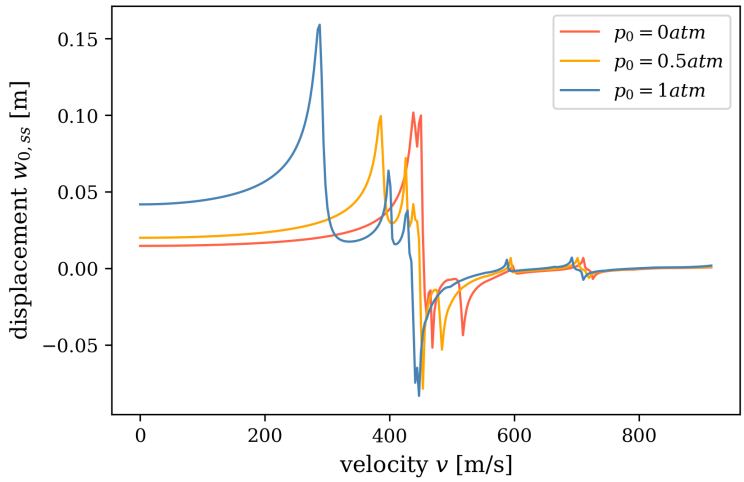

Figure 3.14: Change of the steady-state response due to external pressure

3.8.5. Comparison of Tubular shell and equivalent Euler - Bernoulli beam

This section describes the attempts to align the responses of a tubular shell and an "equivalent" Euler-Bernoulli beam, highlighting the challenges and limitations of this approach. An EB beam is inherently stiffer than a shell element because it neglects shear and cross-sectional deformations. Therefore it is more practical to explore how beam theory can be adjusted to match the characteristics of a shell element, rather than emphasizing their inherent differences. The underlying idea is to investigate the possibilities of a beam to be used as a phenomenological model to study the behaviour of shells or as a reduced-order model to save on computational expense. The adjustment of the beam model should therefore be possible without major prior computations of the shell model.

As discussed in Section 3.8.1, the primary contributor to the displacements in this problem configuration is the bending of the shell walls, with the foundation having negligible effects. In contrast, an Euler-Bernoulli beam element assumes an unchanging cross-section and cannot differentiate between load applications at different points on the cross-section. For a tubular shell, this distinction is significant: a load applied at the bottom directly engages the foundation, while a load on top activates the shell's cross-sectional bending, transferring force to the foundation differently (as shown in Figs. 3.5 and 3.8). Therefore, both a beam and a shell loaded at the bottom would be sensitive to changes in foundation properties. This highlights the importance of considering these differences when attempting to align the behaviours of shell elements and Euler-Bernoulli beams.

To tune the Euler-Bernoulli beam model in such a way as to resemble the characteristics of the shell, the dispersion curve of the beam is matched to the one of the shell. Hereby, the second shell mode ($n = 2$) is considered since it showed to have the greatest contribution in the response for subcritical velocities (see. Fig. 3.4 (b)). The detailed procedure of the tuning process is avoided for brevity and can be seen in Appendix D.

The performance of this tuned beam model is evaluated based on the difference between the steady-state response of the two models across a range of velocities. Figure 3.15 (a) compares the steady-state responses of the beam and shell models, with the beam model scaled by a factor of 5 to match the static displacement of the shell model. This difference in displacement is most likely caused by the other modes which are not considered in the beam model but still contribute to the overall response of the system. Furthermore, the beam model considers no shear deformation which could further increase the displacement and lead to a more comparable

magnitude. From the plot, it is evident that the EB beam model aligns well with the shell model in the subcritical regime. Around the critical velocity, the beam model exhibits a steeper and larger spike, the magnitude of which is solely dependent on the system's damping. In the supercritical velocity range, the beam model fails to capture the effects present in the shell model, particularly the cross-sectional effects that become significant due to the standing wave field in the circumferential direction. This discrepancy is especially notable immediately after reaching the critical velocity, where the shell model shows a negative displacement at the top of the tube due to the resonance with one of the circumferential modes.

Comparing the activated masses between the two models (see Eq. (3.24)), shown in Figure 3.15 (b), it is notable that the beam's activated mass is greater than that of the shell, once the static displacement of the beam was adjusted accordingly. This difference is due to the more localized displacement in the shell compared to the full cross-sectional translation in the beam model. Additionally, the shell has multiple peaks at supercritical velocities due to the resonance of higher circumferential modes. This analysis underscores the limitations of the beam model in capturing the complex dynamics of the shell, particularly in the supercritical regime, but also highlights areas where the models align better.

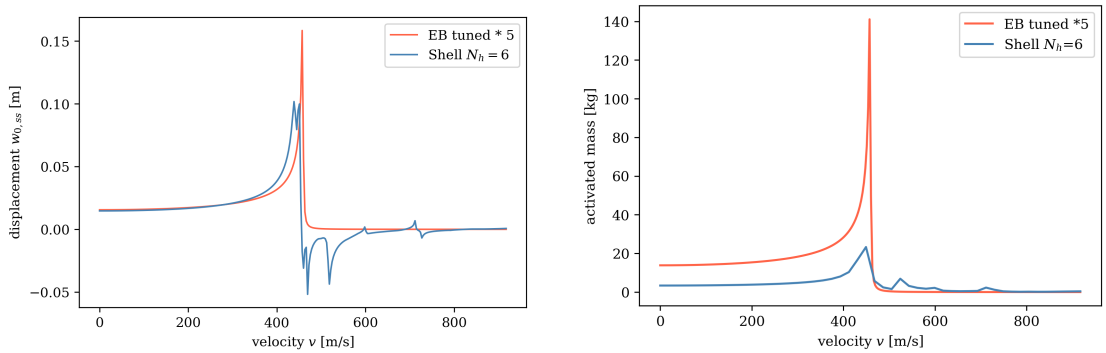

(a) Steady-state response vs. velocity

(b) Activated mass vs. velocity

Figure 3.15: Comparison between the beam and the shell model after tuning – response due to a constant moving load

The activated mass can be computed as shown below, with the shell's activated mass requiring integration over the circumference. It needs to be mentioned that this computation is based on the steady-state response and could differ in a transient case.

$$m_{eff,SH} = \rho h \int_0^{2\pi} |w_{0,ss}(\theta)| d\theta \tag{3.24}$$

$$m_{eff,EB} = \rho A w_{0,ss} \tag{3.25}$$

In summary, the beam model can capture the global characteristics of the steady-state response of the shell model when properly tuned, but it fails to account for the intricacies inherent to the cross-sectional effects, which involve more than just global displacement and encompass wave propagation in the circumferential direction. These limitations might be mitigated in a more realistic modelling approach where the load is applied not directly to the shell wall but rather to an internal rail. Such a model could distribute the load more evenly along the tube, potentially reducing the pronounced effects of the shell and making the beam model a more viable alternative. Even a spatially distributed load, which more closely resembles a realistic scenario, could enable the use of a beam model without introducing significant inaccuracies.

4

Modelling of the Electromagnetic Suspension and Stability Analysis

4.1. Model formulation

To explore the dynamic interaction between the Hyperloop vehicle and the guideway, further extensions of the model developed in Chapter 3 are required. This entails combining the two parts, namely the vehicle and the guideway through an electromagnetic "contact force," which exhibits nonlinear behaviour dependent on the air gap between them. Particularly in electromagnetic suspension (EMS) systems, analysed in this thesis, an increased air gap results in a significant reduction in the attracting force. This property renders the system inherently unstable, necessitating constant adjustment of the electromagnetic force through an active control system. In this model, one of the simplest control systems, the proportional-derivative (PD) controller mentioned in Section 2.3, has been adopted. The vehicle is represented as a lumped mass suspended directly from the inside of the shell. While a more realistic approach would involve suspending the vehicle from an internal rail with multiple points of contact, this was not considered due to the scope limitations of this thesis. To describe the relative motion between the guideway and the vehicle, a new degree of freedom representing the displacement of the mass u needs to be introduced. The equation of motion (EOM) governing the dynamics of this SDOF system is as follows:

$$M\ddot{u} = F_{EMS}(t) - Mg \tag{4.1}$$

In this expression, M marks the mass of the vehicle, g the gravitational constant and F_{EMS} the time-dependent electromagnetic force due to the interaction between the mass and the guideway according to Eqs. (2.14) - (2.16). The theoretical background of this chapter of this thesis is based on the previous study by [7] on the vehicle-structure interaction between an Euler-Bernoulli beam and a suspended mass. Since the present work focuses mainly on the extension of the previous study by [7] through a more realistic guideway model, the detailed derivations of the electromagnetic force are going to be omitted for brevity.

Transitioning from a moving load, as discussed in Chapter 3, to a moving mass problem can introduce two main instability phenomena. Firstly, the electromagnetic suspension (EMS) system itself can become unstable if not properly controlled, irrespective of velocity [8]. The second instability mechanism is wave-induced instability which arises from radiated energy feeding back to the vehicle through the reaction force provided by the infrastructure when moving at supercritical velocities through anomalous Doppler waves [4]. The stability of an equilibrium point is therefore influenced by the interplay of these two mechanisms [7]. It is

worth mentioning that if the model were supported at discrete locations instead of continuously, the system could also become unstable due to a phenomenon known as parametric instability [14]. However, this third mechanism will not be considered in this thesis.

The interaction force between the vehicle and the guideway is non-linearly dependent on the relative displacement between the two. To assess the stability of the equilibrium position, with the proposed methods shown in Section 2.20, the system requires prior linearisation. To verify the results obtained from the linear stability analysis and to study the formation of limit cycles, the non-linear formulation is used. In the next section, the two formulations are derived, starting with the non-linear governing equations of the vehicle-structure interaction.

4.1.1. Non-linear formulation of the vehicle-structure interaction

To formulate the interaction between the vehicle and the guideway, the displacement of the latter needs to be evaluated at the point of action of the electromagnetic force i.e. $\xi = 0$ and $\theta = 0$. The response of the structure to any load can be obtained through the convolution integral with the load and the Green's function as outlined in Section 3.7. This part of the solution is linear and is used in combination with the non-linear EMF to obtain the response of the suspended mass. The governing equations of the vehicle-structure interaction are shown in Eqs. (4.2) - (4.4) and obtained from [7]. Hereby w_0 represents the displacement of the guideway under the moving load, u_{ML} the displacement of the mass, I the current intensity, C a constant describing the properties of the magnet (see Eq. (2.14)), U the voltage in the electromagnet, Δ^{ss} the target air gap and K_p and K_d the control gains for the proportional and derivative components used in the PD control system respectively.

$$F_{EMS}(t) = C\left(\frac{I}{w_0 - u_{ML}}\right)^2 \tag{4.2}$$

$$\dot{I} = \frac{w_0 - u_{ML}}{2C}\left(U - IR + 2C\frac{I}{(w_0 - u_{ML})^2}(\dot{w}_0 - \dot{u}_{ML})\right) \tag{4.3}$$

$$U = K_p\left((w_0 - u_{ML}) - \Delta^{ss}\right) + K_d(\dot{w}_0 - \dot{u}_{ML}) + U^{ss} \tag{4.4}$$

To establish a non-linear formulation of the vehicle-structure interaction, the electromagnetic force used in the convolution integral has to be discretised in time. In this model, a linear variation between the time steps was chosen. The linear variation can be achieved through a combination of the response of two triangular impulses evaluated at $t_{\bar{n}}$ and $t_{\bar{n}+1}$. This allows an approximation of the convolution integral through the two impulses (see [7] Eqs. (7)-(9)). The force in the convolution integral depends on the solution of the integral itself and is consequently implicit in nature. Therefore, the solution is divided into a yet unknown instantaneous contribution, initial condition and a history term. The solution of this form needs to satisfy the equation of motion Eq. (4.1). After substituting the formulations of the EMS (Eqs. (4.2) - (4.4)) into the EOM (Eq. (4.1)), the equations in the discretised form as shown in Eqs. (4.6) - (4.6) can be obtained [7]. The subscript n resembles the discretisation over time. The full expression for $w_{0,n}$ is obtained by evaluating the Green's function for triangular pulses and discrediting over time and can be found in [7] Eqs. (10-11). This results in the expression being a function f of the initial displacement of the guideway $w^{ic}_{0,n}$, the past displacements captured in a history term $w^{hist}_{0,n}$ as well as the displacement of the mass u_n and the current intensity I_n. After the discretisation, the governing equations read:

$$w_{0,n} = f(w^{ic}_{0,n}, w^{hist}_{0,n}, u_{ML,n}, I_n) \tag{4.5}$$

$$M\ddot{u}_n = C\frac{I_n^2}{(w_{0,n} - u_{ML,n})^2} - Mg \tag{4.6}$$

$$\dot{I}_n = \frac{w_{0,n} - u_{ML,n}}{2C}\left(U_n - I_n R + 2C\frac{I_n}{(w_{0,n} - u_{ML,n})^2}\left(\dot{w}_{0,n} - \dot{u}_{ML,n}\right)\right) \tag{4.7}$$

$$U_n = K_p\left(w_{0,n} - u_{ML,n} - \Delta^{ss}\right) + K_d\left(\dot{w}_{0,n} - \dot{u}_{ML,n}\right) + U^{ss} \tag{4.8}$$

The system of discretised ODEs formed by Eqs. (4.6) - (4.8) can be solved through a time-stepping routine. In this project, an in-house built version of a Runge-Kutta algorithm was used.

4.1.2. Linearised model of the vehicle-structure-interaction

To analyse the stability of the system based on an eigenvalue analysis, the system is linearised. As mentioned above, the interaction between the vehicle and the structure is non-linear in nature, hence requiring linearisation upfront, to use the tools mentioned in Section 2.1.1. The guideway model is already linear; a requirement for it to be solved via the Green's function. Even though the system could have multiple equilibrium positions, only the behaviour around its operational equilibrium condition is of interest (i.e., the standard steady-state of an equivalent mechanical system) [7]. To do so, a perturbation was introduced around the steady-state solution of the problem, by substituting $w_0(t) = w^{ss} + w^{tr}(t)$, $u(t) = u^{ss} + u^{tr}(t)$, $F(t) = F^{ss} + F^{tr}(t)$ and $I(t) = I^{ss} + I^{tr}(t)$ into the governing equations describing the electromagnetic force interaction Eqs. (2.14)- (2.16), (3.20) and (4.1). In this context, the superscript ss stands for steady-state and tr for transient response. Employing the first-order Taylor series expansion on Eqs. (2.14) – (2.15) and applying mathematical operations result in the following set of linearised governing equations in the time domain [7]:

$$w_0^{tr} = -\int_0^t g_0(t-\tau)\cdot F^{tr}(\tau)d\tau \tag{4.9}$$

$$M\ddot{u}^{tr} = F^{tr} \tag{4.10}$$

$$F^{tr} = \frac{2CI^{ss2}}{\Delta^{ss3}}\left(\frac{\Delta^{ss}}{I^{ss}}I^{tr} + u^{tr} - w_0^{tr}\right) \tag{4.11}$$

$$\dot{I}^{tr} = \frac{\Delta^{ss}}{2C}\left[-I^{tr}R + K_p\left(w_0^{tr} - u^{tr}\right) + \left(K_d + \frac{2CI^{ss}}{\Delta^{ss2}}\right)\left(\dot{w}_0^{tr} - \dot{u}^{tr}\right)\right] \tag{4.12}$$

As mentioned earlier, the stability of the system is quantified through the eigenvalues of the system matrix, i.e. the roots of the characteristic equation. Therefore, the linearised system needs to be transformed into the Laplace domain, equivalent to the procedure outlined in Sec. 3.2. This results in the following set of equations, whereby the hat symbol indicates that a quantity is in the Laplace domain:

$$\hat{w}_0^{tr} = -\hat{g}_0(s)\cdot\hat{F}^{tr} \tag{4.13}$$

$$s^2 M\hat{u}_{ML}^{tr} = F^{tr} \tag{4.14}$$

$$\hat{F}^{tr} = \frac{2CI^{ss2}}{\Delta^{ss3}}\left(\frac{\Delta^{ss}}{I^{ss}}\hat{I}^{tr} + \hat{u}_{ML}^{tr} - \hat{w}_0^{tr}\right) \tag{4.15}$$

$$s\hat{I}^{tr} = \frac{\Delta^{ss}}{2C}\left[-\hat{I}^{tr}R + K_p\left(\hat{w}_0^{tr} - \hat{u}_{ML}^{tr}\right) + \left(K_d + s\frac{2CI^{ss}}{\Delta^{ss2}}\right)\left(\hat{w}_0^{tr} - \hat{u}_{ML}^{tr}\right)\right] \tag{4.16}$$

Substituting Eq. (4.15) into Eqs. (4.13) and (4.14) allow the expression of the system of equations through a matrix whereby the right-hand side of the equations describes the initial conditions of the system. Hereby $f_0 = su_{ML,0} + v_0$ and $u_{ML,0}$, v_0 and I_0 are the initial displacement, velocity and current intensity respectively. The initial current intensity is the one used to levitate the vehicle at the desired air gap in a static case ($\Delta_{ss} = 15$ mm). The numerical value can be determined by removing the time dependency from Eq. (2.14), defining the air gap and solving the current intensity I_0. The initial displacement of the mass can be found by adding the steady-state response of the guideway to the target air gap. The tube is considered unperturbed concerning the steady-state response and therefore not included in the expression. The system in the matrix reads:

$$\begin{pmatrix} 1 - \hat{g}_0(s)\frac{2CI^{ss2}}{\Delta^{ss3}} & \hat{g}_0(s)\frac{2CI^{ss2}}{\Delta^{ss3}} & \hat{g}_0(s)\frac{2CI^{ss}}{\Delta^{ss2}} \\ \frac{2CI^{ss}}{\Delta^{ss3}Ms^2} & 1 - \frac{2CI^{ss2}}{\Delta^{ss3}Ms^2} & -\frac{2CI^{ss}}{\Delta^{ss2}Ms^2} \\ -\frac{(\Delta^{ss2}K_d + 2CI^{ss})s + \Delta^{ss2}K_p}{2C\Delta^{ss}} & \frac{(\Delta^{ss2}K_d + 2CI^{ss})s + \Delta^{ss2}K_p}{2C\Delta^{ss}} & \frac{\Delta^{ss}R}{2C} + s \end{pmatrix} \begin{pmatrix} \hat{\omega}^{tr} \\ \hat{u}_{ML}^{tr} \\ \hat{I}^{tr} \end{pmatrix} = \begin{pmatrix} 0 \\ f_0 \\ I_0 \end{pmatrix} \tag{4.17}$$

The roots of the system can be found by computing the determinant of the matrix symbolically (using Maple, Sympy or equivalent) and then searching for the values of s which make the determinant vanish i.e. the roots of the characteristic equation. In this approach, the right-hand side is considered to be zero, in other words, the stability of the unperturbed case is analysed. To solve for the eigenvalues, an iterative procedure is used, as the Green's function is also s dependent. In this thesis, a numerical solver was utilised in Python (i.e. Newton algorithm from the scipy.optimize package) with several initial guesses for s to cover the areas of interest in the complex plane [1]. In case either of the eigenvalues has a positive real part, the amplitude of the vehicle displacement grows over time and renders therefore the perturbed system unstable. To verify the results based on this linearised model, the non-linear formulation can be used.

4.2. Green's function in the time domain

This section aims to analyse the Green's function as computed in Section 3.7 after it has been transformed into the time domain by evaluating the inverse Laplace transformation numerically (see Eq. 2.10). By doing so, insights into the transient response of the structure can be gathered, such as the decay of displacement magnitude and oscillation frequency.

The circumferential displacement shape in the sub-critical regime as shown in Fig. 3.5 leads to a very low activation of the foundation damping. Consequently, the system has unrealistically small damping. In a real structure, multiple points of energy dissipation, such as expansion joints and other connections, contribute to greater structural damping than activated in this model. To overcome this, an artificial dashpot is placed at the top ($\theta = 0$) (see Fig. 4.1). The damping coefficient was set to $c^* = 300$ Ns/m^2, to provide sufficient decay but also not alter the results qualitatively. This additional element is incorporated in the EOM in the same manner as the one at the bottom.

Figure 4.2 presents the Green's function in the time domain. As mentioned in the chapters before the Green's function represents the impulse response function of a system, whereby the

[1] The area around the real axis is the most important since it dictates the stability of the system based on Hopf bifurcation. To find the areas of interest, I suggest using contour plots of the real and imaginary parts of the determinant to see where their zero crossings intersect and, consequently the location of the roots

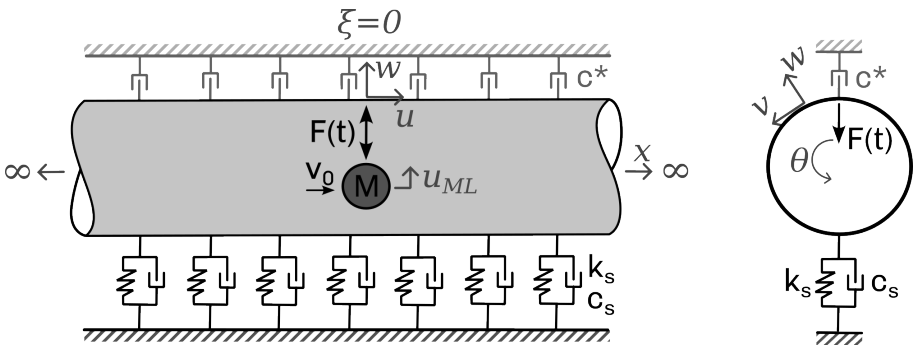

Figure 4.1: Extension of the structure with an additional dashpot to improve the decay over time

impulse is moving with a constant velocity of 0.1 v_{crit} in this case. Sub-figure (a) represents the response without additional damper, i.e. the original configuration of the system. Hereby it is evident that the decay is indeed very small, as the response of the system remains almost unchanged beyond two seconds. By extending the time window even further, it was found that the amplitude decreases only by a very small amount. Sub-figure (b) shows the effect of the additional damper and it can be seen that the decay is indeed improved substantially. In panel (c) the effect of the prestress, caused by the pressure difference, shows that the frequency of the fluctuations decreases significantly. Furthermore, it can be seen that the amplitude of the fluctuations short after the initial impulse peak are larger in amplitude compared to the cases neglecting the external pressure ((a) and (b)), indicating an overall greater amplitude.

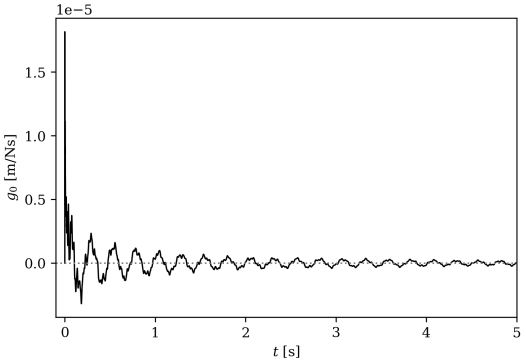

(a) Response of the guideway with $c^* = 0$

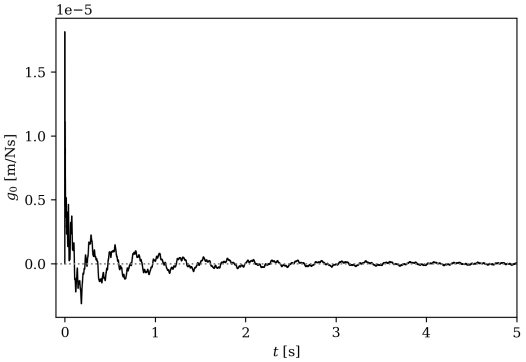

(b) Response of the guideway with $c^* = 300$

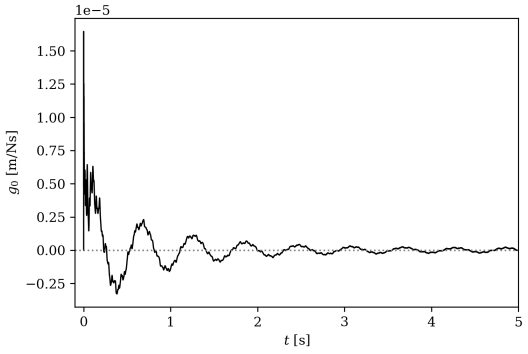

(c) Response of the guideway with $c^* = 300$ and external pressure

Figure 4.2: Green's function in the time domain with-, without additional damper and external pressure at $\xi = 0$ and $\theta = 0$

4.3. Results and Analysis of Vehicle-Structure-Interaction

The following table (Tab. 4.1) summarises the parameters used in this analysis, which were chosen equivalent to the ones used in [7].

Table 4.1: Properties of the vehicle and the electromagnetic suspension

Parameter	Value	Unit
Vehicle Properties		
Mass	7650	kg
Target air-gap (Δ^{ss})	15	mm
Magnet Properties		
Magnetic permeability of air or vacuum (μ_0)	1.26×10^{-6}	H/m
Number of turns (N)	800	-
Area of magnet (A_m)	0.25	m^2

4.3.1. Stability analysis of the linearised system

In this section, the stability of the linearised system is analysed by examining its eigenvalues. Hereby, three scenarios are considered: the unpressurised case, the case with external pressure due to the vacuum inside the tube, and the tuned Euler-Bernoulli (EB) beam model. The latter case is analysed to see if there are parallels between the two systems concerning dynamic stability. If so, the beam model could potentially be used as a phenomenological model to more efficiently obtain qualitative results, thus allowing an investigation of multiple scenarios which would be computationally infeasible when using the shell theory.

The presented models in this configuration capture two instability mechanisms: electromagnetic and wave-induced instability, with the system's stability determined by their interplay. To study these mechanisms individually, two types of analyses are employed. The first is an eigenvalue analysis with varying velocity, where the control gains are kept constant. This approach provides insights into instability caused by radiated energy feedback through anomalous Doppler waves, i.e., wave-induced instability. The second analysis examines eigenvalues for different combinations of control gains K_p and K_d with a fixed velocity, allowing an observation of zones in which combinations of control gains are more favourable over others for a set of fixed velocities. Repeating this analysis for multiple velocities can capture the interplay between the two instability mechanisms.

Shell without external pressure, $p_0 = 0$ atm

The model in this section has no external prestress, representing the reference case (parameters according to Table 3.1). The model includes the additional dashpot in the model as outlined in the previous section, ensuring consistency between the linear and nonlinear cases. The dashpot aids in a faster decay of perturbations, thus saving computational time when analysing limit cycle vibrations.

Figure 4.3 shows the eigenvalues of the linearised system for a fixed pair of control gains. Sub-plot (a) depicts the eigenvalues in the complex plane, with colours indicating the vehicle's velocity. Sub-plot (b) illustrates the real and imaginary parts of the eigenvalues as functions of velocity. The critical velocity $v_{crit} = 458$ m/s is estimated based on the dispersion graphs or the steady-state response shown in Section 3.8.2. Generally, three distinct eigenvalues can be found: one real-valued and two complex conjugates. At velocities around 1.1 v_{crit}, two additional pairs of complex conjugates appear; at higher velocities, only one extra pair was found. These additional eigenvalues, most likely, correspond to branch points of the characteristic equation, introduced by the dynamic stiffness of the infinitely long guideway,

and do not affect the stability of the equilibrium point [7]. In certain velocity ranges, such as around $1.7 - 2v_{crit}$ and $1.0v_{crit}$, no complex roots were found due to the limitations of the numerical root solver (Newton method). Locally adjusting the tolerances could help in finding more roots, although the ones identified now are accurate and additional ones will not alter the results significantly.

The real-valued eigenvalues in Figure 4.3 (a) remain mostly unchanged with increasing velocity, whereas the complex-valued eigenvalues change significantly with varying velocities. As the velocity approaches the critical value from the bottom, the negative real part of the complex-conjugate pair increases in magnitude, indicating faster decay of perturbations. Beyond the critical velocity, the system undergoes multiple instability zones, shown by branch formations in subplot (b). At supercritical velocities, wave-induced instability can occur due to the anomalous Doppler waves excited by the moving vehicle. Given the shell's multiple critical velocities in the supercritical regime – marked by the grey dotted lines based on amplification peaks of the steady-state response – it is suspected that successive zones of wave-induced instability occur and interact with each other. In other words, it is suspected that the instability zones caused by the anomalous Doppler waves for each of the critical velocities are overlapping and thus rendering the equilibrium point unstable for a large range of velocities. In contrast, the beam model exhibits only one instability zone before regaining stability [7].

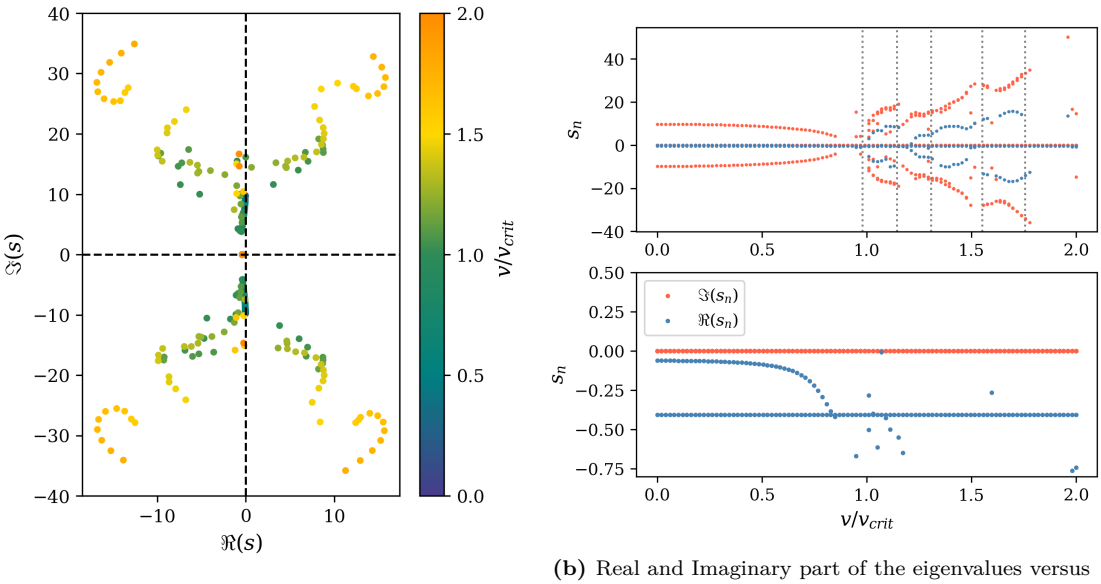

(a) Eigenvalues on the complex plane versus velocity

(b) Real and Imaginary part of the eigenvalues versus velocity

Figure 4.3: Eigenvalues of the linearised system versus the velocity of the vehicle. The bottom right is a zoom-in of the top right plot. $K_p = 20$ [kVs/m], $K_d = 20$ [kV/m]

To gain a more comprehensive overview of the interplay between the two instability mechanisms, Figure 4.4 illustrates the stable zones in the control gain space for selected velocities. The shaded areas indicate where combinations of K_p and K_d result in a positive real part of at least one eigenvalue, signifying zones of instability. Regardless of the velocity, the equilibrium position is unstable if $K_p \leq K_{p,min} \approx 1.2e4$ [kVs/m]. In this case, the control system is too slow to stabilize the vehicle against gravity. Hereby, the *real-valued* eigenvalue is positive and the system is unstable due to *divergence*. If K_p is greater than this threshold, the equilibrium position can be stabilized by appropriately choosing K_p based on K_p. Poorly chosen control gains can lead to instability of the equilibrium position at any velocity. In that case one of the *complex-valued* eigenvalues has a positive real part and the instability mechanism is called

Hopf Bifurcation. The range of stable regimes increases with larger velocities in the subcritical regime, reaching a maximum at $v = 0.8\ v_{crit}$. Generally, the system's stability improves when the structure extracts energy from the system. As the dynamic stiffness of the system decreases with increasing velocity, more energy is extracted due to the evanescent wave field, leading to improved energy dissipation and stability. However, once the vehicle surpasses the critical velocity, the effect reverses. At that point Anomalous Doppler waves feed energy back through the guideway to the suspended mass, a phenomenon more pronounced in structures with lower dynamic stiffness. Sub-figure (b) depicts the stable regimes for supercritical vehicle velocities. Hereby, all the investigated velocities until $\approx 1.5\ v_{crit}$ showed no stable zone. Afterwards, a small stable zone appeared which can be seen in Figure 4.4 (b). This zone grows with an increase in velocity. Against the common intuition, an increase in the damping of the system to mitigate vibrations does not help for instability (comparable to an increase in K_d), but the energy feedback through the guideway into the vehicle actually increases, leading to an unstable equilibrium point.

Even though there are velocities where no stable zone was found at supercritical velocities, it is suspected that a very small zone exists throughout all velocities, which was just unable to be detected due to the coarse grid size chosen in the analysis. This would align with the qualitative behaviour of an Euler Bernoulli beam shown in [7]. Nevertheless, the small size of the stability zone would make it practically impossible to stabilise the system from a control system point of view.

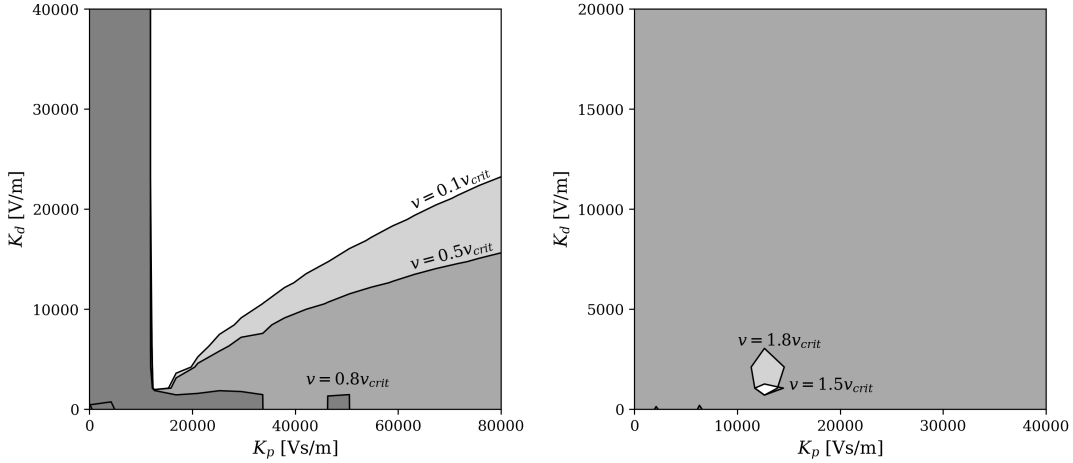

(a) Subcritical velocities

(b) Supercritical velocities

Figure 4.4: Stability vs control gains for different vehicle velocities; subcritical velocities $v = 0.1$–$0.8v_{crit}$ (left panel) supercritical velocities $v = 1.5 - 1.8v_{crit}$ (right panel); grey indicates combination of instability; between $1.0 - 1.5v_{crit}$ no stable zone was found.

Shell with external pressure, $p_0 = 1$ atm

In this section, the results of the stability analysis are presented for the system which considers the effects of the internal prestress caused by the vacuum on the inside of the tube. Figure 3.14 demonstrates that the prestress reduces the critical velocity ($v_{crit,p0} = 284$ m/s) and causes greater amplification in the steady-state response. Consequently, the system's stability response is also expected to change. Given the reduced critical velocity with internal pressure, it is wise to normalize velocities based on the reduced critical velocity such that $v/v_{crit,p0} \leq v/v_{crit,p}$. This normalization allows a comparison of the two cases according to their specific critical velocity and observes potential qualitative differences in their responses.

The left panel of Figure 4.5 (a) shows the eigenvalues in the complex plane and the right one the real and imaginary parts against velocity. For subcritical velocities, the system behaves similarly to the unpressurised case, gaining stability due to the decrease in dynamic stiffness and energy dissipation of the guideway. Beyond approximately 1.25 $v_{\text{crit},p0}$, an additional pair of complex roots appears, with one pair crossing the real axis, causing instability via a *supercritical Hopf bifurcation*. The system then experiences an extended zone of instability at supercritical velocities, similar to the reference case. Around 1.5 $v_{\text{crit},p0}$, the system tends to regain its stability but before it becomes stable the real part keeps growing once again until 2.0 $v_{\text{crit},p0}$. The analysis shows that the system is not stable at any point after the initial onset of instability; for the selected control gains the onset of instability happens at $\approx 1.25\ v_{\text{crit},p0}$. The grey dotted lines indicate once again the zones of amplification in the steady-state response, consequently the critical velocities of the individual harmonics according to Fig. 3.14.

Compared to the unpressurised shell shown in Figure 4.3, the pressurised shell exhibits fewer branches of instability. This difference is due to the relative velocities between the two cases, as the pressurised shell effectively considers velocities up to approximately 550 m/s, even though Figure 3.14 indicates that more critical velocities occur at higher velocities. This effect is caused by the fact that the preloading condition, seems to affect the lower modes greater than the higher ones. The onset of instability happens occurs at a much lower velocity for the pressurised case than for the case without the consideration of the vacuum on the inside of the tube. The system destabilises at 355 m/s opposed to 458 m/s, whereby it has to be mentioned that the numerical values of these velocities might differ depending on the chosen control gains.

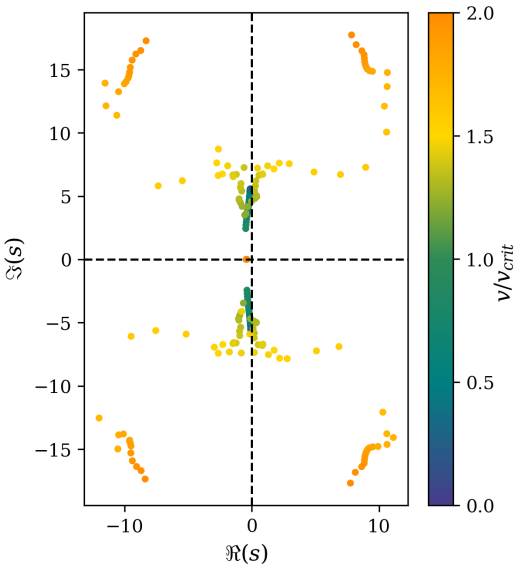

(a) Eigenvalues on the complex plane versus velocity

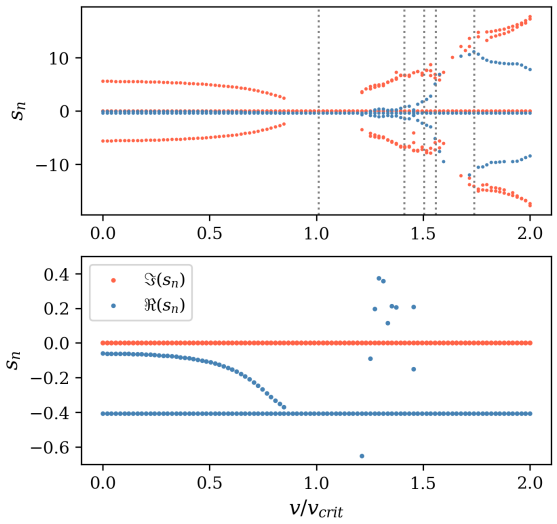

(b) Real and Imaginary part of the eigenvalues versus velocity

Figure 4.5: Eigenvalues of the linearised system versus the velocity of the vehicle. The bottom right is a zoom-in of the top right plot. $K_p = 20$ [kVs/m], $K_d = 20$ [kV/m], $p_0 = 1$ atm

Figure 4.6 shows the stable zones in the space of control gains for various velocities. Sub-figure (a) illustrates that the initial loading condition positively impacts system stability. The reduction in stiffness due to the external pressure increases the energy dissipation of the guideway. This effect is further amplified with increased velocity, eventually making almost the entire region stable, provided that $K_p \leq K_{p,\text{min}}$.

Sub-figure (b) shows the onset of instability at supercritical velocities. Hereby it can be

seen that the unstable zone slowly grows until it abruptly changes from an overall stable zone of control gains to a completely unstable one (see Sub-figure (c)). With the present resolution of this analysis, no stable zone was found from that point afterwards.

It is important to note that although the preloading condition enhances the system's stability for subcritical velocities compared to the unpressurised case, the range of subcritical velocities is reduced significantly. This effectively brings the critical velocities closer to the system's operational conditions, thus potentially increasing its susceptibility to losing stability as a consequence of the interplay between the two instability mechanisms.

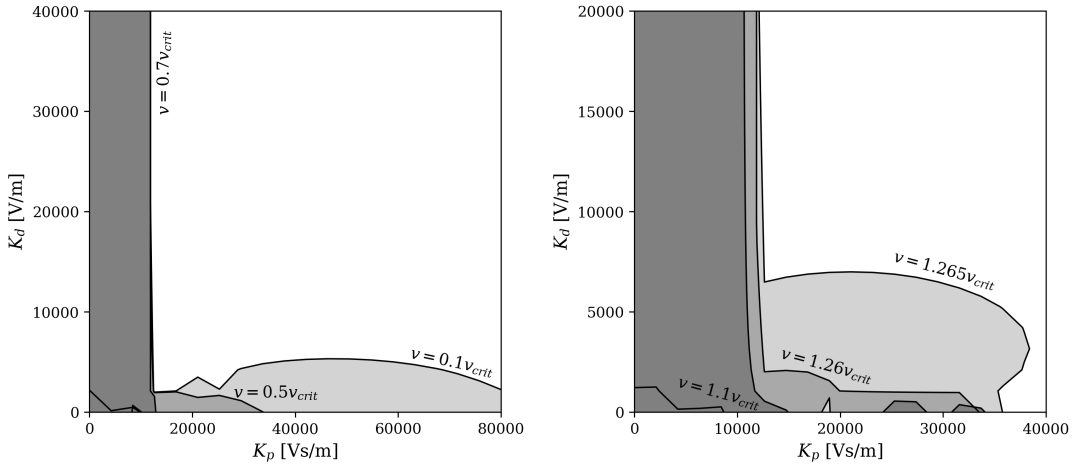

(a) Subcritical velocities

(b) Supercritical velocities $v = 1.1$–$1.265\ v_{crit}$

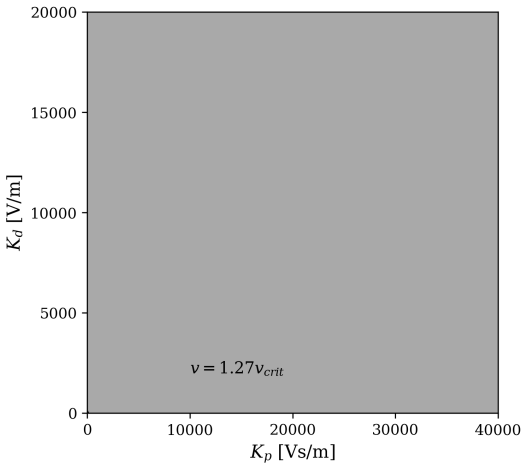

(c) Supercritical velocities $v = 1.27\ v_{crit}$

Figure 4.6: Stability vs control gains for different vehicle velocities for a pressurised shell; subcritical velocities $v = 0.1$–$0.7\ v_{crit}$ (left panel) supercritical velocities v = $v = 1.1\ v_{crit}$ (right panel); grey indicates zones of instability. After v = $v = 1.27\ v_{crit}$ no stable zone was found. $p_0 = 1$ atm

Tuned Euler-Bernoulli model

The main idea of this section is to showcase the qualitative differences between the Euler-Bernoulli beam model and the shell model, whereby former has been tuned to match the properties of the shell model (see Sec. 3.8.5). This comparison allows an evaluation of the beam model's performance as a phenomenological or reduced-order model. As shown in Figure 4.2, the shell was damped locally at the top of the tube, since the foundation at the bottom had negligible effects due to the decoupled motions. Since the beam model cannot distinguish

between the point of load application, the damping constant at the top of the shell ($c^* = 300\ \mathrm{Ns/m^2}$) is used for the foundation of the beam model.

Figure 4.7 illustrates the qualitative differences in behaviour. While the shell is shown to be mostly unstable after reaching supercritical velocity, the beam exhibits only one such zone at very high velocities (for the chosen control gains).

Conceptually, both systems behave similarly: they remain stable at low velocities if the control gains are chosen appropriately. As velocity increases, the real part of the complex eigenvalues decreases, making the system less prone to losing stability due to perturbations. Around the critical velocity, the system becomes unstable due to anomalous Doppler waves excited by the vehicle moving at high velocities. If the velocity increases further, the system regains stability. The same behaviour was found in [7]. However, depending on the parameters or the type of the model the onset of instability and the unstable range differ significantly. The analysed shell model is subjected to a much greater zone of instability compared to the beam model.

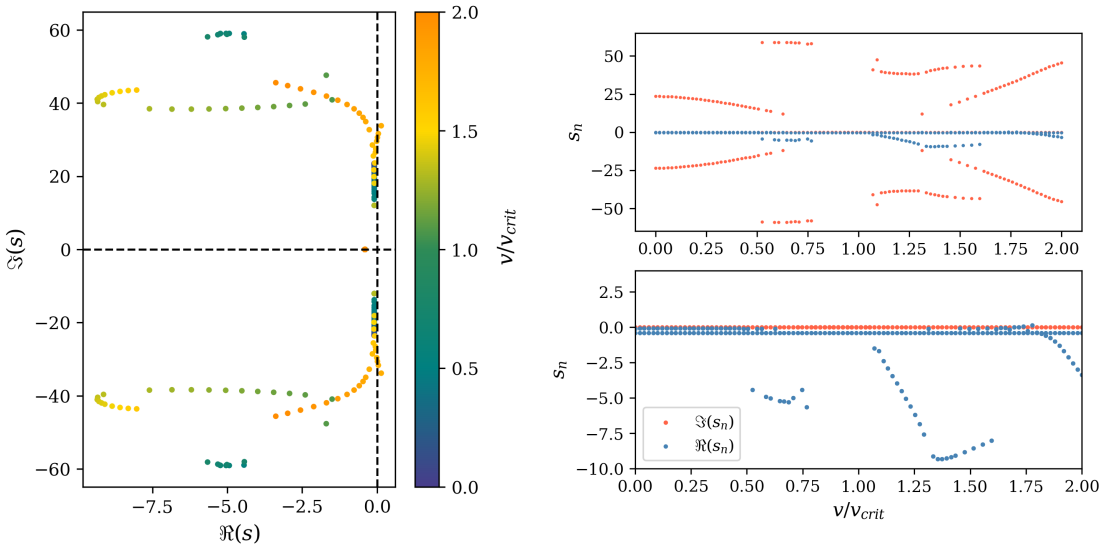

(a) Eigenvalues on the complex plane versus velocity

(b) Real and Imaginary part of the eigenvalues versus velocity

Figure 4.7: Eigenvalues of the linearised system versus the velocity of the vehicle. The bottom right is a zoom-in of the top right plot. $K_p = 20$ [kVs/m], $K_d = 20$ [kV/m]

Figure 4.8 below shows the stability zones in the space of control gains. At subcritical velocities (a), the stability zone is qualitatively similar to that of the shell model, as indicated in Figure 4.4, although the beam model appears to have a slightly larger stable zone. This is caused by the fact that the beam is tuned to the lowest frequency peak occurring in the Green's function, even though the response of the shell is composed of multiple modes each with its resonance frequency. Increasing the velocity further improves stability, with a maximum reached at approximately 0.5 v_{crit}. Beyond this point, the stability zone slightly reduces in size (see $v = 0.8\ v_{crit}$ in (b)).

After the critical velocity is reached, the system feeds energy back into itself, resulting in increased instability zones. Notably, around 1.5 v_{crit}, the unstable zone connects with the area $< K_{p,\mathrm{min}}$, leaving a small enclosed zone that remains stable throughout all velocities. As the speed of the moving load increases, the instability zone continues to grow – the horizontal line at 1.8 v_{crit} shifts upward (panel (c)). Further increasing the velocity shifts the horizontal line upwards and increases the enclosed stable zone close to the origin. At a velocity of 2.0 v_{crit} (panel (d)), the entire domain is unstable except for a small enclosed area near $K_{p,\mathrm{min}}$.

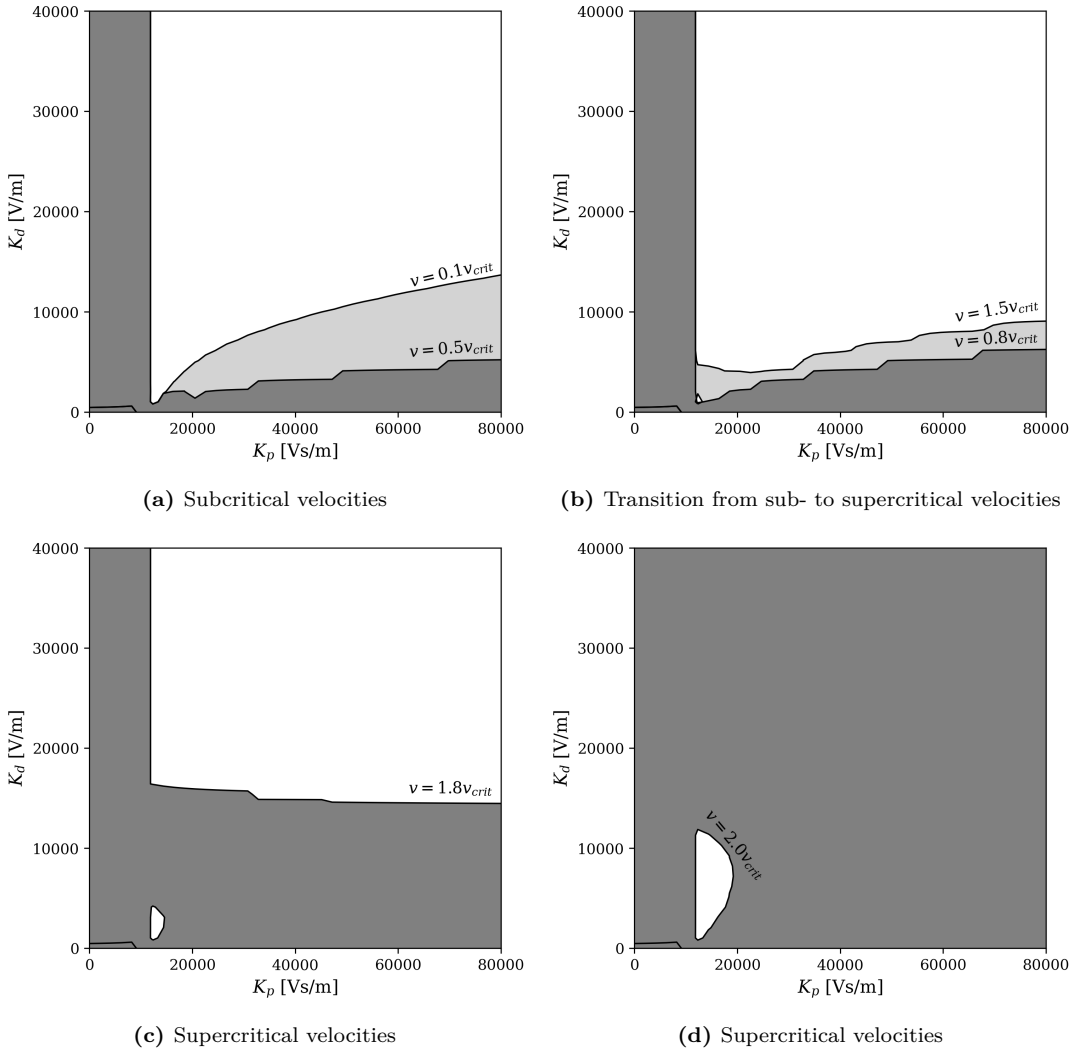

(a) Subcritical velocities

(b) Transition from sub- to supercritical velocities

(c) Supercritical velocities

(d) Supercritical velocities

Figure 4.8: Stability vs control gains for different vehicle velocities for the adjusted Euler Bernoulli beam; subcritical velocities $v = 0.1$–$0.5\ v_{crit}$ (top left panel), the transition between the two regimes $v = 0.8$–$1.5\ v_{crit}$ (top right panel), supercritical velocities $v = 1.8$–$2.0\ v_{crit}$ (bottom panels); grey indicates zones of instability.

Comparing the beam and shell models, the main stability characteristics are similar, especially in the subcritical regime. However, at supercritical velocities, the beam model fails to capture the more complex wave propagation and interaction caused by the waves propagating in axial but also circumferential directions (forming a standing wave field in case of steady-state). The multitude of anomalous Doppler waves excited in the shell model extends its instability zone over a much wider range of velocities. Nonetheless, the qualitative behaviour concerning the control parameters is comparable to the beam model. For example, the small stable zone close to the origin that exists at supercritical velocities exists for both the shell and beam model (compare Fig. 4.4 (b) and Figs. 4.8 (b)-(d)). In conclusion, the beam model can be used as a reduced-order model at subcritical velocities if tuned accordingly. However, it must be noted that for this specific problem configuration, the stiffness was somewhat underestimated by tuning the beam only to the first shell mode. At supercritical velocities, the responses of the two models are qualitatively different, making it inadvisable to use the beam as a reduced-order model. Instead, it should be considered a phenomenological model for studying the influence of global parameters on the stability of the system.

It is worth mentioning that if this thesis's model were extended to include another internal

rail, an equivalent two-layered beam model could be a viable approximation.

4.3.2. Transient analysis

This section analyses the non-linear response of the model which is computed numerically based on the formulation shown in Sec. 4.1.1, accounting for the interaction between the tubular shell and the vehicle. This non-linear analysis is used to validate the results obtained from the linear stability analysis. It should be noted that the non-linear response depends largely on the chosen time duration, as a system can prove to be unstable if the observation time is sufficiently long, even though it may initially appear otherwise. Furthermore, the non-linear transient response is compared to the linear transient response, which can be obtained by solving the linearised system in the Laplace domain (see Eq. (4.17)). The response can then be transformed back to the time domain using the inverse Laplace transformation numerically.

Non-linear stability analysis

To assess the stability of the non-linear system for the given problem, the transient analysis is computed numerically based on the Green's function, which then gives insights into the development of the response over time. Based on that the stability of the equilibrium position can be judged and thus the results obtained from the linear stability analysis are validated.

When the equilibrium position is unstable, as indicated by the shaded regions in the space of control gains (see Sec. 4.3.1), but close to the instability boundaries (black curves), limit cycles can be observed, provided that $K_p \leq K_{p,min}$. Limit cycles can only occur in non-linear systems, as explained in Sec. 2.1.2. In this study, the limit cycles are caused by the electromagnetic force and can therefore occur at any velocity. The limit cycle arises whenever the control system responds aggressively to a deviation from the target air gap, i.e. a perturbation from the steady-state equilibrium position. This results in an overshooting of the target value which afterwards requires a correction by reducing the electromagnetic force to zero. At this stage, the vehicle undergoes free fall until the control system increases the force again to prevent it from dropping entirely. This cyclic behaviour creates the limit cycles as the control system cannot react quickly enough. For a controlled system limit cycles can occur at any velocity if the control gains are chosen accordingly. In that case the system is unstable but the amplitude of the oscillations is limited by the limit cycle.

The Runge-Kutta algorithm used in this analysis includes a stop criterion if the non-linear (NL) response diverges. If the force reaches zero at any point in time or the amplitude grows over time slow enough to not cause divergence, limit cycle vibrations are considered to be reached. If neither condition applies, the system can be considered stable for the given observation time. It is important to note that systems can still become unstable afterwards and the results could vary for different initial conditions. By categorising the NL transient response based on the criteria mentioned before, it is possible to define zones of stability, instability, and limit-cycle oscillation in the space of control gains. Generally, an observation time of 25 seconds was chosen as a compromise between computational time and accuracy.

Figure 4.9 shows the stability zones obtained from the numerical analysis. Grey areas indicate unstable zones and light grey areas are unstable zones with stable limit cycles. Sub-figure (a) shows that a time signal of 25 seconds is not sufficient to fully detect the stability of the system, as the analysis shows stability in the zones of $K_p \leq K_{p,min}$. Generally speaking, the formation of limit cycles takes longer at subcritical velocities because the amplitude growth is smaller due to greater energy dissipation of the guideway compared to supercritical velocities. Sub-figure (b) shows the vehicle moving at a supercritical velocity, where the system exhibits a stability zone similar to that shown in the beam model (Fig. 4.4 (b)).

Compared to the linear stability analysis in Fig. 4.4 the non-linear transient analysis

seems to overestimate the stable system configuration. Nevertheless, the fact that even after 50 seconds (in case of the analysis for subplot (a)) the system does not experience a growth in amplitude, suggests that the instability will most likely never occur in a realistic scenario. Since the amplitude growth is so small, limit cycle vibrations are expected to occur eventually or vehicle is subject to new perturbations in the meantime.

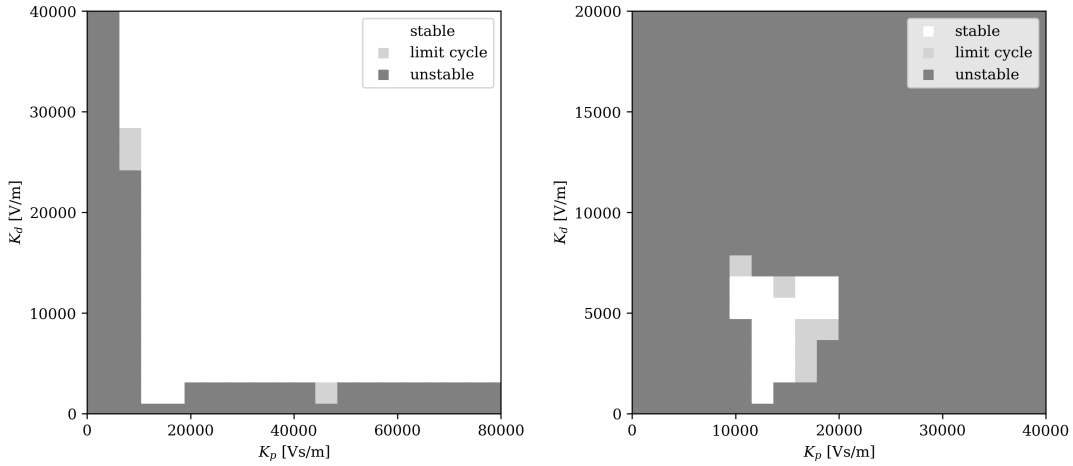

(a) $v = 0.5v_{crit}$; 50 s time-frame **(b)** $v = 1.8v_{crit}$; 25 s time-frame

Figure 4.9: Non-linear stability analysis

Limit cycle vibrations

In this section, the limit cycle vibrations are presented for a selected case from Fig. 4.9.

In the presence of limit cycle vibrations, the control system prevents the vehicle from colliding with the guideway by switching off the EMF altogether (zero current intensity). Due to this property, the vibrations of the system are limited upwards to the magnitude of the target air gap between the guideway and the vehicle. To the bottom, on the other hand, the displacement magnitude can surpass that value, which results in an off-centred limit cycle. In a real scenario, there is most likely a limit to the maximum current intensity that the magnet can be subjected to which ultimately also limits the magnitude to the bottom. This was not considered in the magnet model used in this thesis.

Figure 4.10 shows the transient response of the guideway, the mass and the electromagnetic force in a configuration where limit cycle vibrations exist. This indicates that the equilibrium position is considered unstable, which was correctly captured by the linear transient analysis, as shown by the grey line. Unlike the non-linear response, the linear response is not self-limiting and grows exponentially in magnitude over time. The lowest panel of the plot shows the electromagnetic force, which drops to zero during the limit cycle oscillation to avoid a collision of the vehicle with the track. The black line represents the steady-state response for the static case, resembling the target value that the control system tries to maintain, i.e., a constant air gap of $15mm$. Notably, the mass displacement does not cross zero in the non-linear case, as this would resemble a collision of the vehicle and the guideway which is prevented by the control system. If the system does collide with the guideway, the control system is unable to stabilise its fluctuations and the limit cycle can no longer exist. A similar effect occurs when K_p is too large since the control system is so aggressive that it overshoots the target in such a way that it breaks the limit cycle.

Figure 4.11 shows the limit cycle of the mass in the phase plane. It is important to note that the limit cycle in this case is of infinite dimension and is only shown as a projection on a 2D phase plane. Therefore, it appears that the trajectories are crossing each other, which would

violate the uniqueness theorem, but in their multidimensional space, they do not intersect.

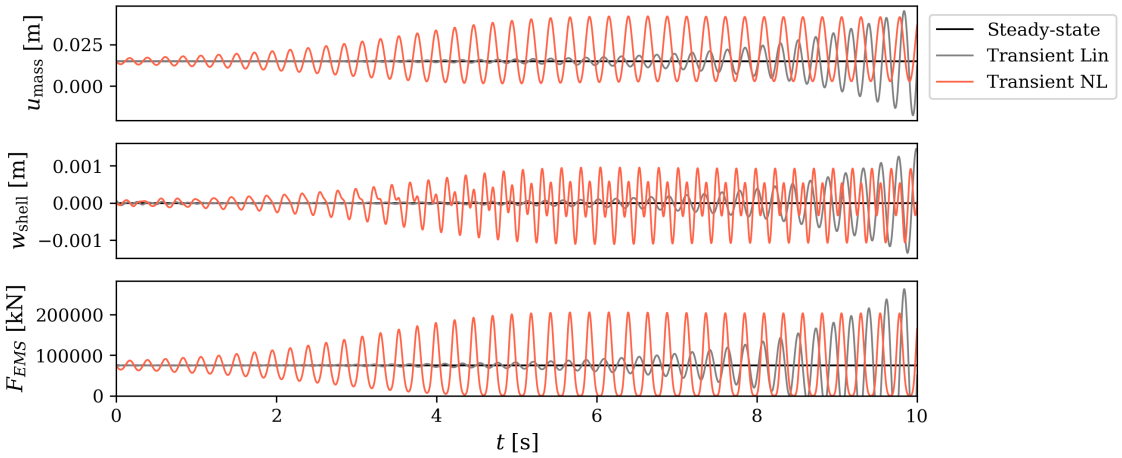

Figure 4.10: Transient response of the vehicle, the guideway and the electromagnetic force, for the linear and non-linear case; limit cycle vibrations for $v = 1.8v_{crit}$ and $K_p = 20$ [kVs/m], $K_d = 5$ [kV/m]. Note that limit cycles can occur at any velocity due to the control system.

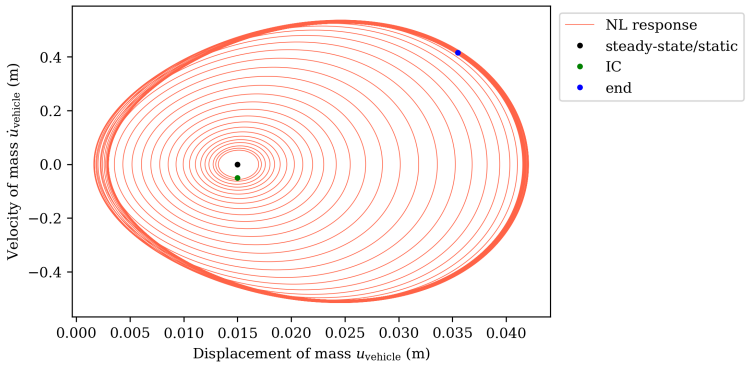

Figure 4.11: Limit cycle in the phase plane for $v = 1.8v_{crit}$ and $K_p = 20$ [kVs/m], $K_d = 5$ [kV/m]

5

Conclusions and Discussion

This thesis aimed to expand the knowledge of the dynamic behaviour of a Hyperloop system by employing a more sophisticated structural model. This was achieved by successfully modelling the guideway as a tubular shell instead of 1D elements, based on which the dynamic amplification andsthe stability was investigated. The model was solved in a semi-analytical manner whereby numerical methods were used only when necessary. The implementation of the shell theory resulted in qualitative changes in the system's behaviour, advancing the understanding of the mechanisms inherent to the structure. The study highlighted the effect of various model parameters on the steady-state response of the system. Based on an eigenvalue analysis of the linearised system, the stability of the steady-state equilibrium was investigated. The study highlighted that the pressure difference between the inside and outside of the tube leads to significant changes in the results, both for the dynamic amplification as well as the dynamic stability.

5.1. First central research question

What is the influence on the system's steady-state response when properly accounting for the tube through a cylindrical shell compared to a classical Euler-Bernoulli beam?

The main difference between beam and shell elements is that the cross-section can deform in the case of tubular shells, while the whole cross-section remains unchanged in beams. This results in an overestimation of the stiffness in the latter case which consequently reflects on the difference in critical velocities. Not only does the critical velocity occur at much lower velocities for the shell, but also the presence of waves propagating in both circumferential and axial directions, whereby the former leads to a standing wave field due to wave interference, results in multiple critical velocities, each linked to a specific circumferential mode. Once the vehicle surpasses the critical velocity the quasi-static displacement field changes to a standing wave field in the circumferential direction, which changes depending on the velocity to different resonance modes. The flexural wave moves therefore along the tube as a standing wave field around the circumference.

The study highlighted the significant impact of various structural parameters on critical velocities, demonstrating their potential for strategic vibration reduction. Specifically, it was analysed how foundation stiffness, tube thickness, diameter, and prestress from internal vacuum alter the dynamic behaviour. These effects were analysed through the system's steady-state response. (Sec. 3.8).

This analysis revealed that foundation stiffness has a negligible impact on the dynamic behaviour at the top of the tube. As a result of the small bending stiffness of the shell wall

compared to the foundation, the structure's dynamic response at the top is effectively decoupled from the bottom when loaded locally with a perpendicular force. In this case, the load is still carried by the foundation but the additional feedback of the spring foundation due to dynamic loading does not significantly influence the response at the top of the tube. Thus, varying foundation stiffness results in negligible changes in the overall response. It has to be mentioned that it might be exclusive to the properties chosen in this thesis and that the parameter could gain importance if a larger thickness or smaller diameter were to be investigated. As this model considers the effects of discrete supports by a distributed continuous stiffness, it is not necessary to consider variations in span length, since it would only alter foundation stiffness which changes were proven to be insignificant. However, in a model that accurately captures periodic supports, the tube experiences periodic excitation with a frequency depending on both the velocity as well as the span. While in the present model, the beam modes are not much activated due to the continuous supports, it is expected that this changes as soon as the supports are at discrete locations, since the tube would deform between two supports similar to a beam. In that case, a variation of the span would be crucial as they change the frequency of periodic excitation, greatly affecting the dynamic amplification.

The study further highlighted that the diameter and thickness of the tube significantly influence the critical velocity. An increase in thickness or a reduction in diameter raises the critical velocity. While both changes have similar effects on the critical velocity, their impact on wave characteristics differs. A smaller diameter increases wave frequencies, whereas increased thickness affects only the wavelength.

The novel implementation of the shell theory allowed an investigation of the effects that the hoop stresses, caused by the low pressure on the inside of the tube, have on the dynamic response of the guideway. Increasing internal pressure within the tube decreases the frequency of the modes, resulting in a lower frequency response under a moving load. When considering the vacuum inside the tube, the critical velocity was found to reduce by nearly half, causing the system to operate closer to this critical velocity. The steady-state response also increases in magnitude as the pressure effectively amplifies the response. Even in an extended model, considering the internal rail as well as the discrete foundation, the effects caused by the external pressure, will not differ qualitatively from the one of the present study. Considering that Hyperloop systems are supposed to operate under vacuum conditions, the effect of the vacuum on dynamic behaviour should be implemented in the analysis as the response is greatly differs.

Using beam models is often the first choice when building models due to their extensively studied behaviour and computational efficiency. In the initial part of the thesis, it was observed that the steady-state response of the shell can be accurately captured at subcritical velocities using beam models, despite some differences in displacement magnitude. However, as the vehicle moves at supercritical velocities, the effects of the circumferential displacement field become more prominent, which cannot be adequately described by the beam model. Consequently, the beam model cannot serve as a reduced-order model unless appropriately tuned to match an existing more advanced (e.g., shell) model. Nevertheless, it provides valuable insights into phenomena with minimal computational effort, making it suitable for use as a phenomenological model to study the effects of parameters on the global behaviour of the shell. Once again this could differ in case the structural characteristics change for example if the contribution of the shell wall binding motion becomes less pronounced.

In summary, the critical velocities are significantly influenced by structural characteristics. Geometric modifications, such as increasing thickness or reducing diameter, increase critical velocities and thus reduce the dynamic amplification at operational conditions. However, including the effects of the external pressure lowers critical velocities, which could be detrimental

by bringing operational conditions closer to the supercritical zones. Therefore, strategic adjustments to the tube's structural characteristics can effectively enhance its dynamic properties and reduce vibrations in the system. A beam model can be used to make judgements about the global behaviour of the system if tuned accordingly, as it is computationally favourable over the present model. However, if the vehicle is moving at supercritical velocities, the simplistic model fails to capture the mechanisms of the shell model.

5.2. Second central research question

What is the influence on the system's stability when properly accounting for the tube through a cylindrical shell compared to a classical Euler-Bernoulli beam?

While the response of the beam model is qualitatively similar to the shell at subcritical velocities, differences emerge as the vehicle exceeds the critical velocity. The shell exhibits an extended instability zone from the onset of instability onwards, whereby it appears that the instability zones caused by the individual circumferential modes overlap with each other causing the extended unstable zone. The beam model on the other hand displays more gradual instability onset, as long as the stiffness is not greatly overestimated as else the transition between the stable and unstable configuration happens very suddenly. The beam model, however, serves well for investigative purposes, offering quick insights into the effects of certain parameters on system stability. For instance, it helps identify the required length for reaching limit cycle vibrations and the regions where they occur and allows an investigation of the effects of changing stiffness, damping, and vehicle mass in a more efficient way than the shell model.

The study showed, based on the steady-state response of the system, that an adjustment of the structural characteristics can significantly improve stability by increasing the critical velocity, thereby ensuring operational conditions remain within the subcritical range. Increasing stiffness reduces energy dissipation of the guideway, which, while unfavourable for electromagnetic instability at subcritical velocities, prevents the occurrence of wave-induced instability by eliminating the excitation of anomalous Doppler waves, which actively feed energy back into the system. The study showed that the interaction between the two instability mechanisms causes a very large zone of instability and should therefore be avoided by any means.

The absence of the wave-induced instability makes the selection of the required control gains simpler such that the occurrence of limit cycle vibrations can be avoided altogether. Which although not causing a failure of the system, can lead to passenger discomfort or accelerated deterioration of the infrastructure. However, this may vary for more complex structures involving internal rails.

It is important to note that although the system's stability for subcritical velocities improves with internal pressure compared to the unpressurised case, the range of subcritical velocities is significantly reduced. This effectively brings the critical velocities closer to the system's operational conditions, potentially increasing its susceptibility to losing stability.

To summarise the main findings concerning the stability of the system, it was found that beam and shell models show similar responses at subcritical velocities, but differences arise beyond the critical velocity. The shell model exhibits an extended instability zone due to interactions between circumferential modes, whereas the beam model shows a gradual instability onset unless stiffness is overestimated. The beam model proved useful for quickly assessing the effects of parameters like stiffness, damping, and vehicle mass on system stability but fails to capture more complex mechanisms inherent to the system. Adjusting structural characteristics can improve stability by increasing the critical velocity, and thus preventing wave-induced in-

stability under operational conditions. However, the internal low pressure enhances stability at subcritical velocities but brings critical velocities closer to operational conditions and increases susceptibility to instability due to the interplay between the two instability mechanisms.

5.3. Discussion and Recommendations

This study investigates the influence of modelling a Hyperloop guideway as an infinite tubular shell as opposed to a beam model or single-degree-of-freedom system, as it was done in the past. From a practical point of view, the dynamic behaviour of a more realistic guideway model was studied and insights into the shell subject to a constant moving load were gathered. Further, the interplay between two fundamentally different stability mechanisms was investigated, namely the *electromagnetic instability* inherent to the EMS suspension system and the *wave-induced instability* caused by the vehicle moving at supercritical velocities. The stability of the system is hereby determined by the interplay between the two mechanisms. Furthermore, the study considers the initial membrane state of the shell due to the vacuum inside the tube and its impact on structure response.

From a theoretical point of view, a method to analyse tubular shells subject to moving loads in a semi-analytical manner was investigated. Whereby the problem-specific properties made it challenging to solve the problem by assuming a solution based on a summation of wavenumbers. This was potentially caused by the weak coupling of the circumferential modes of the shell and consequently, close spacing of the roots in the complex plane, which required precision of the root solver algorithms which was computationally infeasible with the provided tools. Thereafter, the Greens's function was obtained using wavenumber integration to numerically evaluate the inverse Fourier transformation. This method allowed a study of various modelling parameters as well as the transient response of the system and the stability of the equilibrium point.

The study's approach provides a comprehensive framework for evaluating critical velocities and dynamic behaviour as well as understanding the underlying mechanics of the Hyperloop guideway, contributing valuable insights for future research and development in this area.

5.3.1. Recommendations and further explorations

Due to the challenges faced in this thesis when solving the posed problem, it is advisable to use the wavenumber integration right away or solve similar problems using numerical or semi-numerical methods such as the *semi-analytical finite element method* (SAFE), which partially discretises the problem and thus finds a compromise between the analytical and purely numerical method (classical FEM). In a similar problem, considering an infinitely long system, I advise using a discretisation in the circumferential direction to treat the infinite boundaries analytically. Furthermore, the analysis of a more realistic cross-section could be facilitated, such as a varying thickness to account for the internal rail or other local stiffening elements that run along the tube.

Given the limited scope of this thesis, the proposed Hyperloop structure which is composed of a tubular shell supported at discrete locations, contains an internal rail and stiffeners, and is subject to a vehicle with multiple points of contact, had to be reduced to a simpler model. I propose that further studies could look into supporting the tubular shell at discrete locations and include stiffening elements or investigate the effects of having a two-layered system, properly accounting for an internal rail and the outer tube. Alternatively, a two-layered system whereby both are modelled as beam elements could be investigated. For such a model, I suggest that the element resembling the outer tube has periodic supports and that the internal rail is either continuously connected to the outer tube or connected at discrete locations with a different periodicity than the outer tube. Based on the results of this thesis, I assume that

either of the two modelling approaches will cause significant changes in the behaviour of the system. Thus greatly contributing to the already existing knowledge and aiding in the further development of the system as a whole.

References

[1] Nicholas A. Alexander and Mohammad M. Kashani. "Exploring Bridge Dynamics for Ultra-high-speed, Hyperloop, Trains". en. In: *Structures* 14 (June 2018), pp. 69–74. ISSN: 23520124. DOI: 10.1016/j.istruc.2018.02.006. (Visited on 06/13/2024).

[2] Jonathan M. Blackledget. *Digital Signal Processing*. Ed. by Jonathan M. Blackledget. Second Edition. Woodhead Publishing Series in Electronic and Optical Materials. Woodhead Publishing, 2006. ISBN: 978-1-904275-26-8. DOI: https://doi.org/10.1533/9780857099457.1.

[3] Karel van Dalen. *Applied Dynamics of Structures*. Delft University of Technology. Lecture notes CIEM5220 unit 3. 2023.

[4] G.G. Denisov, E.K. Kugusheva, and V.V. Novikov. "On the problem of the stability of one-dimensional unbounded elastic systems". In: *Journal of Applied Mathematics and Mechanics* 49.4 (1985), pp. 533–537. ISSN: 0021-8928. DOI: https://doi.org/10.1016/0021-8928(85)90065-6.

[5] European Court of Auditors. *A European high-speed rail network : not a reality but an ineffective patchwork*. eng. Special report No ... (European Court of Auditors. Online). LU: Publications Office, 2018. (Visited on 12/29/2023).

[6] Andrei B. Fărăgău, Andrei V. Metrikine, and Karel N. van Dalen. "Dynamic Amplification in a Periodic Structure Subject to a Moving Load Passing a Transition Zone: Hyperloop Case Study". In: *Recent Trends in Wave Mechanics and Vibrations*. Ed. by Zuzana Dimitrovová et al. Cham: Springer International Publishing, 2023, pp. 651–661. ISBN: 978-3-031-15758-5.

[7] Andrei B. Fărăgău et al. "The Interplay Between the Electro-Magnetic and Wave-Induced Instability Mechanisms in the Hyperloop Transportation System". en. In: (2024). Ed. by Walter Lacarbonara. Series Title: NODYCON Conference Proceedings Series, pp. 617–627. DOI: 10.1007/978-3-031-50631-4_52.

[8] Junxiong Hu et al. "Levitation Stability and Hopf Bifurcation of EMS Maglev Trains". In: *Mathematical Problems in Engineering* (Apr. 2020), pp. 28439–28458. DOI: 10.1155/2020/2936838.

[9] Hardt Hyperloop. *Hardt Hyperloop Introduction*. 2023. URL: https://docs.hardt.global (visited on 05/27/2024).

[10] Arthur W. Leissa and Mohamad S. Qatu. *Vibrations of continuous systems*. en. OCLC: 733291025. New York: McGraw-Hill, 2011. ISBN: 978-0-07-171480-8.

[11] Leissa, Arthur W. *Vibrations of shells*. en. Ohio State University, Columbus, Ohio: American Institute of Physics, 1993. ISBN: 1-56396-293-4.

[12] A.V. Metrikine and H.A. Dieterman. "Instablility of vibrations of a mass moving uniformly along an axially comperessed beam on a viscoelastic foundation". en. In: *Journal of Sound and Vibration* 201.5 (Apr. 1997), pp. 567–576. ISSN: 0022460X. DOI: 10.1006/jsvi.1996.0783. (Visited on 06/02/2024).

[13] Andrei Metrikine. "Unstable lateral oscillations of an object moving uniformly along an elastic guide as a result of an anomalous Doppler effect". In: *Acoustical Physics - ACOUST PHYS-ENGL TR* 40 (Jan. 1994), pp. 85–89.

[14] Andrei V. Metrikine. “Parametric Instability of a Moving Particle on a Periodically Supported Infinitely Long String”. In: *Journal of Applied Mechanics* 75.1 (Jan. 2008), p. 011006. ISSN: 0021-8936. DOI: 10.1115/1.2745368. URL: https://doi.org/10.1115/1.2745368.

[15] Pedro Museros et al. “Key aspects in the analysis and design of Hyperloop™ infrastructure under static, dynamic and thermal loads”. In: *Engineering Structures* 239 (2021), p. 112177. ISSN: 0141-0296. DOI: https://doi.org/10.1016/j.engstruct.2021.112177.

[16] Jonas Kristiansen Nøland. “Prospects and Challenges of the Hyperloop Transportation System: A Systematic Technology Review”. In: *IEEE Access* 9 (Feb. 2021), pp. 28439–28458. DOI: 10.1109/ACCESS.2021.3057788.

[17] M. Ruzzene and A. Baz. “Dynamic stability of periodic shells with moving loads”. en. In: *Journal of Sound and Vibration* 296.4-5 (Oct. 2006), pp. 830–844. ISSN: 0022460X. DOI: 10.1016/j.jsv.2006.03.008. (Visited on 03/19/2024).

[18] H. Santos et al. “A semi-analytical finite element model for the analysis of cylindrical shells made of functionally graded materials”. en. In: *Composite Structures* 91.4 (Dec. 2009), pp. 427–432. ISSN: 02638223. DOI: 10.1016/j.compstruct.2009.04.008. (Visited on 01/17/2024).

[19] Steven H. Strogatz. *Nonlinear Dynamics and Chaos*. 2nd ed. USA: Westview, 2015.

[20] Matteo Strozzi et al. “A Comparison of Shell Theories for Vibration Analysis of Single-Walled Carbon Nanotubes Based on an Anisotropic Elastic Shell Model”. en. In: *Nanomaterials* 13.8 (Apr. 2023), p. 1390. ISSN: 2079-4991. DOI: 10.3390/nano13081390. (Visited on 01/17/2024).

[21] Athanasios Tsetas. “A unified modelling framework for vibratory pile driving methods”. en. PhD thesis. Delft University of Technology, 2023. DOI: 10.4233/UUID:C9CB4A2A-ABEB-4DE5-B0B0-5BEBD3416407. (Visited on 02/29/2024).

[22] Athanasios Tsetas, Apostolos Tsouvalas, and Andrei V. Metrikine. “A non-linear three-dimensional pile–soil model for vibratory pile installation in layered media”. en. In: *International Journal of Solids and Structures* 269 (May 2023), p. 112202. ISSN: 00207683. DOI: 10.1016/j.ijsolstr.2023.112202.

[23] Valery V. Vasiliev and Evgeny V. Morozov. “Circular Cylindrical Shells”. en. In: *Advanced Mechanics of Composite Materials and Structures*. Elsevier, 2018, pp. 687–759. ISBN: 978-0-08-102209-2. DOI: 10.1016/B978-0-08-102209-2.00010-4. (Visited on 02/26/2024).

[24] Stanislav Nikolaevich Veritchev. *Instability of a vehicle moving on an elastic structure*. en. Delft: DUP Science, 2002. ISBN: 978-90-407-2361-2.

[25] Sandeep VM. *When and why to use P, PI, PD and PID Controller?* en. Oct. 2021. URL: https://medium.com/@svm161265/when-and-why-to-use-p-pi-pd-and-pid-controller-73729a708bb5 (visited on 02/05/2024).

[26] Kevin Weicker, Raydin Salahifar, and Magdi Mohareb. “Shell analysis of thin-walled pipes. Part I – Field equations and solution”. en. In: *International Journal of Pressure Vessels and Piping* 87.7 (July 2010), pp. 402–413. ISSN: 03080161. DOI: 10.1016/j.ijpvp.2010.03.025. (Visited on 01/29/2024).

[27] Eric W. Weisstein. *Green's Function*. en. Text. Publisher: Wolfram Research, Inc. URL: https://mathworld.wolfram.com/ (visited on 04/08/2024).

[28] Han Wu et al. “Dynamic stability of an electromagnetic suspension maglev vehicle under steady aerodynamic load”. en. In: *Applied Mathematical Modelling* 97 (Sept. 2021), pp. 483–500. ISSN: 0307904X. DOI: 10.1016/j.apm.2021.04.008. (Visited on 06/13/2024).

[29] L. Zhang and Y. Xiang. “Exact solutions for vibration of stepped circular cylindrical shells”. en. In: *Journal of Sound and Vibration* 299.4-5 (Feb. 2007), pp. 948–964. ISSN: 0022460X. DOI: 10.1016/j.jsv.2006.07.033. URL: https://linkinghub.elsevier.com/retrieve/pii/S0022460X06006249 (visited on 04/10/2024).

[30] Mingjuan Zhao et al. “Instability of vibrations of an oscillator moving at high speed through a tunnel embedded in soft soil”. en. In: *Journal of Sound and Vibration* 494 (Mar. 2021), p. 115776. ISSN: 0022460X. DOI: 10.1016/j.jsv.2020.115776. (Visited on 02/19/2024).

A

Appendix A

A.1. Alternative solution method using root solving routine

This section is supposed to explain the required steps to solve the system by using an assumed solution as a summation of harmonic waves, which is referred to as root solving routine in this thesis. Although this method was not successful due to the computational limitations and the tools available at this point, the method could be useful in analysing models whereby the specific characteristics allow a more reliable computation of the roots of the system.

To facilitate the following analysis, the guideway was split into two displacement fields, one describing the motion in front of the moving load (positive ξ domain) and one behind (negative ξ domain). The two displacement fields are coupled at a moving interface and the corresponding interface conditions. Splitting the displacement field at the point of the load application renders also the equation of motion in the radial direction (w) homogeneous as F_w from Eq. (3.3) is considered at the interface. This allows solving for the roots of the system without the need for a particular solution. Note that F_w is positively defined in the positive coordinate direction (outwards of the tube). Therefore the negative sign in Eq. (3.3) occurs on the right-hand side of the equation.

Since the spatial derivative of w is of the fourth order and both u and v are derived twice with respect to ξ in Eqs. (3.1) - (3.3), there is a total of 8 interface conditions that need to be formulated (4 for each of the two domains). The stress resultants for a tubular shell can be computed as explained in Section 2.4.1. For the structure analysed in this thesis (see Figure 3.1), the following conditions have to be met at the shell interface, more specifically at the contact point of the force $\xi = 0$. The superscript "+" or "-" denotes the positive or negative domain of the spatial variable ξ respectively. At the interface, the continuity in the displacements and internal forces has to be satisfied as well as the shear force equilibrium due to the external load. The last two interface conditions shown in Eq. (A.7) and Eq. (A.8) are the equilibrium of the Kelvin-Kirchhoff edge shear forces in- and out-of-plane respectively as mentioned in [29].

A.1.1. Interface conditions

$$u(0,\theta,\tau)^- = u(0,\theta,\tau)^+ \tag{A.1}$$
$$v(0,\theta,\tau)^- = v(0,\theta,\tau)^+ \tag{A.2}$$
$$w(0,\theta,\tau)^- = w(0,\theta,\tau)^+ \tag{A.3}$$
$$w'(0,\theta,\tau)^- = w'(0,\theta,\tau)^+ \tag{A.4}$$
$$N_x(0,\theta,\tau)^- = N_x(0,\theta,\tau)^+ \tag{A.5}$$
$$M_x(0,\theta,\tau)^- = M_x(0,\theta,\tau)^+ \tag{A.6}$$
$$N_{x,\theta}(0,\theta,\tau)^- + \frac{M_{x,\theta}(0,\theta,\tau)^-}{R} = N_{x,\theta}(0,\theta,\tau)^+ + \frac{M_{x,\theta}(0,\theta,\tau)^+}{R} \tag{A.7}$$
$$\left(Q_x(0,\theta,\tau)^+ + \frac{1}{R}\frac{\partial}{\partial\theta}M_{x,\theta}(0,\theta,\tau)^+\right) - \left(Q_x(0,\theta,\tau)^- + \frac{1}{R}\frac{\partial}{\partial\theta}M_{x,\theta}(0,\theta,\tau)^-\right) = F_w(\tau)\delta(\theta) \tag{A.8}$$

The full expression of the individual stress resultants at the shell edge of a cylindrical shell according to Flügge's thin shell theory reads:

$$N_x(\xi,\theta,\tau) = -\frac{Eh}{12R^3\left(\nu^2-1\right)}\left(12R^2\left(\nu w(\xi,\theta,\tau) + \nu\frac{\partial}{\partial\theta}v(\xi,\theta,\tau) + \frac{\partial}{\partial\xi}u(\xi,\theta,\tau)\right) - h^2\frac{\partial^2}{\partial\xi^2}w(\xi,\theta,\tau)\right) \tag{A.9}$$
$$N_{x,\theta}(\xi,\theta,\tau) = \frac{Eh}{24R^3\left(\nu+1\right)}\left(12R^2\frac{\partial}{\partial\theta}u(\xi,\theta,\tau) + 12R^2\frac{\partial}{\partial\xi}v(\xi,\theta,\tau) + h^2\frac{\partial}{\partial\xi}v(\xi,\theta,\tau) - h^2\frac{\partial^2}{\partial\xi\partial\theta}w(\xi,\theta,\tau)\right) \tag{A.10}$$
$$M_x(\xi,\theta,\tau) = \frac{Eh^3}{12R^2\left(\nu^2-1\right)}\left(-\nu\frac{\partial}{\partial\theta}v(\xi,\theta,\tau) + \nu\frac{\partial^2}{\partial\theta^2}w(\xi,\theta,\tau) - \frac{\partial}{\partial\xi}u(\xi,\theta,\tau) + \frac{\partial^2}{\partial\xi^2}w(\xi,\theta,\tau)\right) \tag{A.11}$$
$$M_{x,\theta}(\xi,\theta,\tau) = \frac{Eh^3}{12R^2\left(\nu+1\right)}\left(\frac{\partial}{\partial\xi}v(\xi,\theta,\tau) - \frac{\partial^2}{\partial\xi\partial\theta}w(\xi,\theta,\tau)\right) \tag{A.12}$$
$$M_{\theta,x}(\xi,\theta,\tau) = -\frac{Eh^3}{24R^2\left(\nu+1\right)}\left(\frac{\partial}{\partial\theta}u(\xi,\theta,\tau) - \frac{\partial}{\partial\xi}v(\xi,\theta,\tau) + 2\frac{\partial^2}{\partial\xi\partial\theta}w(\xi,\theta,\tau)\right) \tag{A.13}$$
$$Q_x(\xi,\theta,\tau) = \frac{\partial}{\partial\xi}M_x(\xi,\theta,\tau) + \frac{1}{R}\frac{\partial}{\partial\theta}M_{\theta,x}(\xi,\theta,\tau) \tag{A.14}$$

Equivalent to the EOMs, the interface conditions have to be projected onto the circumferential modes and expressed in terms of the wavenumbers. Hereby the, assumed solution $\hat{\bar{U}}(k,s) = \bar{u}(\xi,\tau)\cdot e^{-ik\xi}\cdot e^{s\tau}$ can simply be substituted into the expressions above. In this expression, k represents the specific wavenumbers which represent the roots or poles of the system and s the corresponding frequencies.

The interface conditions after projection and substitution are summarised below.

Interface conditions projected on the circumferential modes
Projected on mode $n = 0$:

$$u_0^-(\xi,\tau) - u_0^+(\xi,\tau) = 0 \tag{A.15}$$

$$w_0^-(\xi,\tau) - w_0^+(\xi,\tau) = 0 \tag{A.16}$$

$$\frac{\partial}{\partial\xi} w_0^-(\xi,\tau) - \frac{\partial}{\partial\xi} w_0^+(\xi,\tau) = 0 \tag{A.17}$$

$$\begin{aligned}&\frac{Eh}{12R\left(\nu^2-1\right)}\left(-12R\left(\frac{\partial}{\partial\xi}u_0^-(\xi,\tau)\right)+12R\left(\frac{\partial}{\partial\xi}u_0^+(\xi,\tau)\right)+h^2\left(\frac{\partial^2}{\partial\xi^2}w_0^-(\xi,\tau)\right)\right.\\&\left.-h^2\left(\frac{\partial^2}{\partial\xi^2}w_0^+(\xi,\tau)\right)-12\nu w_0^-(\xi,\tau)+12\nu w_0^+(\xi,\tau)\right)=0\end{aligned} \tag{A.18}$$

$$\frac{E\,h^3}{12R\left(\nu^2-1\right)}\left(R\left(\frac{\partial^2}{\partial\xi^2}w_0^-(\xi,\tau)\right)-R\left(\frac{\partial^2}{\partial\xi^2}w_0^+(\xi,\tau)\right)-\frac{\partial}{\partial\xi}u_0^-(\xi,\tau)+\frac{\partial}{\partial\xi}u_0^+(\xi,\tau)\right)=0 \tag{A.19}$$

$$\begin{aligned}&\frac{E\,h^3}{12R\left(\nu^2-1\right)}\left(-R\left(\frac{\partial^3}{\partial\xi^3}w_0^-(\xi,\tau)\right)+R\left(\frac{\partial^3}{\partial\xi^3}w_0^+(\xi,\tau)\right)+\frac{\partial^2}{\partial\xi^2}u_0^-(\xi,\tau)-\frac{\partial^2}{\partial\xi^2}u_0^+(\xi,\tau)\right)\\&=\frac{F(\tau)}{2\pi}\delta(\xi)\end{aligned} \tag{A.20}$$

$$v_{sn}^-(\xi,\tau) - v_{sn}^+(\xi,\tau) = 0 \tag{A.21}$$

$$\begin{aligned}&\frac{1}{2R^2\left(\nu+1\right)}\left(\left(R^2+\frac{h^2}{4}\right)\left(\frac{\partial}{\partial\xi}v_{sn}^-(\xi,\tau)\right)+\left(-R^2-\frac{h^2}{4}\right)\left(\frac{\partial}{\partial\xi}v_{sn}^+(\xi,\tau)\right)+\right.\\&\left.\frac{n}{4}\left(h^2\left(\frac{\partial}{\partial\xi}w_{cn}^-(\xi,\tau)\right)-h^2\left(\frac{\partial}{\partial\xi}w_{cn}^+(\xi,\tau)\right)-4R\left(u_{cn}^-(\xi,\tau)-u_{cn}^+(\xi,\tau)\right)\right)\right)hE=0\end{aligned} \tag{A.22}$$

Projected on cosine-mode $n > 0$:

$$u_{cn}^-(\xi,\tau) - u_{cn}^+(\xi,\tau) = 0 \tag{A.23}$$

$$w_{cn}^-(\xi,\tau) - w_{cn}^+(\xi,\tau) = 0 \tag{A.24}$$

$$\frac{\partial}{\partial\xi} w_{cn}^-(\xi,\tau) - \frac{\partial}{\partial\xi} w_{cn}^+(\xi,\tau) = 0 \tag{A.25}$$

$$\begin{aligned}&-\frac{hE}{R\,\nu^2-R}\left(-\frac{h^2}{12}\left(\frac{\partial^2}{\partial\xi^2}w_{cn}^-(\xi,\tau)\right)+\frac{h^2}{12}\left(\frac{\partial^2}{\partial\xi^2}w_{cn}^+(\xi,\tau)\right)+R\left(\frac{\partial}{\partial\xi}u_{cn}^-(\xi,\tau)\right)\right.\\&\left.-R\left(\frac{\partial}{\partial\xi}u_{cn}^+(\xi,\tau)\right)+\nu\left(v_{sn}^-(\xi,\tau)\,n-v_{sn}^+(\xi,\tau)\,n+w_{cn}^-(\xi,\tau)-w_{cn}^+(\xi,\tau)\right)\right)=0\end{aligned} \tag{A.26}$$

$$-\frac{h^3E}{12R^2\nu^2-12R^2}\left(-R^2\left(\frac{\partial^2}{\partial\xi^2}w_{cn}^-(\xi,\tau)\right)+R^2\left(\frac{\partial^2}{\partial\xi^2}w_{cn}^+(\xi,\tau)\right)+R\left(\frac{\partial}{\partial\xi}u_{cn}^-(\xi,\tau)\right)\right. \tag{A.27}$$
$$\left.-R\left(\frac{\partial}{\partial\xi}u_{cn}^+(\xi,\tau)\right)+n\nu\left(w_{cn}^-(\xi,\tau)\,n-w_{cn}^+(\xi,\tau)\,n+v_{sn}^-(\xi,\tau)-v_{sn}^+(\xi,\tau)\right)\right)=0$$

$$\frac{h^3E}{(24\nu^2-24)\,R^3}\left(-2R^3\left(\frac{\partial^3}{\partial\xi^3}w_{cn}^-(\xi,\tau)\right)+2R^3\left(\frac{\partial^3}{\partial\xi^3}w_{cn}^+(\xi,\tau)\right)+2R^2\left(\frac{\partial^2}{\partial\xi^2}u_{cn}^-(\xi,\tau)\right)\right. \tag{A.28}$$
$$-2R^2\left(\frac{\partial^2}{\partial\xi^2}u_{cn}^+(\xi,\tau)\right)+n\left(R\,(\nu+1)\left(\frac{\partial}{\partial\xi}v_{sn}^-(\xi,\tau)\right)-R\,(\nu+1)\left(\frac{\partial}{\partial\xi}v_{sn}^+(\xi,\tau)\right)\right.$$
$$\left.\left.+2\left(\left(\frac{\partial}{\partial\xi}w_{cn}^-(\xi,\tau)\right)R-\left(\frac{\partial}{\partial\xi}w_{cn}^+(\xi,\tau)\right)R-\frac{\left(u_{cn}^-(\xi,\tau)-u_{cn}^+(\xi,\tau)\right)(\nu-1)}{2}\right)n\right)\right)=\frac{F(\tau)}{\pi}\delta(\xi)$$

Projected interface conditions in the Laplace-wavenumber domain
Projected on mode $n=0$:

$$\hat{U}_0^- - \hat{U}_0^+ = 0 \tag{A.29}$$

$$\hat{W}_0^- - \hat{W}_0^+ = 0 \tag{A.30}$$

$$-ik\left(\hat{W}_0^- - \hat{W}_0^+\right) = 0 \tag{A.31}$$

$$\frac{12hE}{12R\,\nu^2-12R}\left(-\frac{h^2\left(\hat{W}_0^- - \hat{W}_0^+\right)k^2}{12}+i\left(\hat{U}_0^- - \hat{U}_0^+\right)Rk-\nu\left(\hat{W}_0^- - \hat{W}_0^+\right)\right)=0 \tag{A.32}$$

$$\frac{k\,h^3E}{(12\nu^2-12)\,R}\left(-k\left(\hat{W}_0^- - \hat{W}_0^+\right)R+i\hat{U}_0^- - i\hat{U}_0^+\right)=0 \tag{A.33}$$

$$-\frac{k^2h^3E}{(12\nu^2-12)\,R}\left(ik\left(\hat{W}_0^- - \hat{W}_0^+\right)R+\hat{U}_0^- - \hat{U}_0^+\right)=\frac{F}{2\pi} \tag{A.34}$$

Projected on sine-mode $n>0$:

$$\hat{V}_{sn}^- - \hat{V}_{sn}^+ = 0 \tag{A.35}$$

$$\frac{hE}{2\,(\nu+1)\,R^2}\left[\left(\left(i\hat{V}_{sn}^+ - i\hat{V}_{sn}^-\right)R^2+\frac{ih^2}{4}\left(\left(-\hat{W}_{cn}^- + \hat{W}_{cn}^+\right)n+\hat{V}_{sn}^+ - \hat{V}_{sn}^-\right)\right)k\right. \tag{A.36}$$
$$\left.-Rn\left(\hat{U}_{cn}^- - \hat{U}_{cn}^+\right)\right]=0$$

Projected on cosine-mode $n>0$:

$$\hat{U}_{cn}^- - \hat{U}_{cn}^+ = 0 \tag{A.37}$$

$$\hat{W}_{cn}^{-} - \hat{W}_{cn}^{+} = 0 \tag{A.38}$$

$$-ik\left(\hat{W}_{cn}^{-} - \hat{W}_{cn}^{+}\right) = 0 \tag{A.39}$$

$$\frac{hE}{R\,\nu^2 - R}\left(\left(-\hat{W}_{cn}^{-} + \hat{W}_{cn}^{+} + \left(\hat{V}_{sn}^{+} - \hat{V}_{sn}^{-}\right)n\right)\nu + k\left(-\frac{h^2 k}{12}\left(\hat{W}_{cn}^{-} - \hat{W}_{cn}^{+}\right)\right.\right. \tag{A.40}$$
$$\left.\left. + i\left(\hat{U}_{cn}^{-} - \hat{U}_{cn}^{+}\right)R\right)\right) = 0$$

$$\frac{h^3 E}{12R^2\nu^2 - 12R^2}\left(n\left(\left(-\hat{W}_{cn}^{-} + \hat{W}_{cn}^{+}\right)n + \hat{V}_{sn}^{+} - \hat{V}_{sn}^{-}\right)\nu + kR\left(-k\left(\hat{W}_{cn}^{-} - \hat{W}_{cn}^{+}\right)R\right.\right. \tag{A.41}$$
$$\left.\left. + i\hat{U}_{cn}^{-} - i\hat{U}_{cn}^{+}\right)\right) = 0$$

$$\frac{h^3 E}{(24\nu^2 - 24)\,R^3}\left(-2\,ik^3\left(\hat{W}_{cn}^{-} - \hat{W}_{cn}^{+}\right)R^3 - 2k^2\left(\hat{U}_{cn}^{-} - \hat{U}_{cn}^{+}\right)R^2\right. \tag{A.42}$$
$$\left. + ik\left(\left(-2\hat{W}_{cn}^{-} + 2\hat{W}_{cn}^{+}\right)n + (\nu+1)\left(\hat{V}_{sn}^{+} - \hat{V}_{sn}^{-}\right)\right)nR - n^2\left(\hat{U}_{cn}^{-} - \hat{U}_{cn}^{+}\right)(\nu - 1)\right) = \frac{F}{\pi}$$

A.1.2. General solution to the coupled system

The general solution of the wave amplitudes for the homogeneous algebraic equations (Eq. (3.11) - Eq. (3.13), when splitting the domain accordingly) is shown in Eq. (A.43) below.

$$u_n(\xi, s) = \sum_{j=1}^{N_{roots}} \gamma_{u,n}(s) \cdot C_j(s) \cdot e^{-i \cdot k_j(s) \cdot \xi} \tag{A.43}$$

The wave amplitude in axial direction is for an arbitrary circumferential mode n. In this notation, k represents the wavenumbers which represent the roots of the system matrix formed by Eqs. (3.11) - (3.13). A wavenumber of the system is found once it makes the determinant of the system matrix vanish; the matrix becomes singular. The coefficients C are found by substituting the assumed solution into the interface conditions. They define the contribution of each of the individual harmonic components that make up the wave amplitude. As the system is assumed to be infinite in length, the radiation condition applies which ensures a decay of the wave amplitude with increased distance from the load. This boundary condition is applied by using only those wavenumbers which result in a negative real part in the exponent in other words the wavenumbers must be chosen such that $\Re(-i \cdot k_j \cdot \xi)$ is negative to ensure a decay with increasing distance from the source. For this assumed solution we have the following two cases when this condition is satisfied:

- $\xi < 0 = \Im(k_j) > 0$
- $\xi > 0 = \Im(k_j) < 0$

The coefficient γ represents the displacement ratios analogue to a mode shape (eigenvector) and is needed in solving the coupled system. Since the wavenumbers and the wave amplitudes are determined for the whole system in case of full coupling, they cannot be allocated to a

specific displacement component anymore. The coefficient γ scales the individual harmonics for the various wave amplitudes accordingly.

As the system size for the coupled symmetric case is of the size $2 + 3N_h$, we have a total of $6 + 8N_h$ roots in our system. In case the system would be possible to decouple – removal of the foundation at the bottom of the shell – the γ factor is only needed for one circumferential mode and therefore of size 3 (size 2 in case of $n = 0$), as there is still coupling between the EOMs which is unavoidable for most of the shell theories.

Substituting the general solution for one wave amplitude mentioned above (Eq. (A.43)) into the circumferential expansion or general solution for the full displacement shown in Eq. (3.6) the displacement field of the system in the Laplace domain can be obtained.

$$u(\xi,\theta,s) = \sum_{j=1}^{N_{roots}} \gamma_{u,0} \cdot C_j(s) \cdot e^{-i\cdot k_j(s)\cdot\xi} + \sum_{n=1}^{N_h} \left(\sum_{j=1}^{N_{roots}} \gamma_{u,n} \cdot C_j(s) \cdot e^{-i\cdot k_j(s)\cdot\xi} \right) \cos(n\theta) \quad \text{(A.44)}$$

$$v(\xi,\theta,s) = \sum_{n=1}^{N_h} \left(\sum_{j=1}^{N_{roots}} \gamma_{v,n} \cdot C_j(s) \cdot e^{-i\cdot k_j(s)\cdot\xi} \right) \sin(n\theta)$$

$$w(\xi,\theta,s) = \sum_{j=1}^{N_{roots}} \gamma_{w,0} \cdot C_j(s) \cdot e^{-i\cdot k_j(s)\cdot\xi} + \sum_{n=1}^{N_h} \left(\sum_{j=1}^{N_{roots}} \gamma_{w,n} \cdot C_j(s) \cdot e^{-i\cdot k_j(s)\cdot\xi} \right) \cos(n\theta)$$

The largest computational cost in solving the problem comes in finding the roots k_j of the system (wavenumbers). Due to the coupled nature of the problem, the size of the system is $2 + 3N_h$ (assuming symmetry). For $N_h = 1$, thus considering the modes $n = 0$ and $n = 1$, the limit of finding a symbolic expression for the determinant is already reached by using Maple, SymPy or another symbolic software. The advantage of having such a solution is that the roots of the characteristic polynomial can be found efficiently with a root solver algorithm for polynomials. These algorithms are computationally favourable over optimisation-based algorithms. In case $N_h > 1$, no polynomial can be obtained from the matrix and the roots can only be found through complex root solvers, whereby a root is found when the real and imaginary part of the numerically computed determinant is zero. Hereby the algorithms are based on an optimisation algorithm (ex. Newton method) in the complex plane or algorithms based on subdivisions and contour integration. These routines come with the drawback of computational expense and sensitivity to their problem-specific parameters.

B

Appendix B

B.1. Additional pressure terms projected on the circumferential modes

Note that the terms are ordered according to the EOMs, δu, δv, δw. In this case of $n = 0$ the EOM in tangential direction (v) is not present as symmetry in the response is assumed.

Projected on circumferential mode $n = 0$.

$$\frac{2R^2 p_r \left(-\nu^2+1\right)\left(\frac{\partial}{\partial\xi} w_0(\xi,\tau)\right)}{Eh} \tag{B.1}$$

$$\frac{2R^2 p_r \left(-\nu^2+1\right)\left(\frac{\partial}{\partial\xi} u_0(\xi,\tau)\right)}{Eh} \tag{B.2}$$

Projected on circumferential mode $n > 0$.

$$\frac{\left(-\nu^2+1\right)\left(R^2 p_r\left(\frac{\partial}{\partial\xi} w_{cn}(\xi,\tau)\right)+49Rp_r u_{cn}(\xi,\tau)\right)}{Eh} \tag{B.3}$$

$$\frac{\left(-\nu^2+1\right)\left(49Rp_r v_{sn}(\xi,\tau)+7Rp_r w_{cn}(\xi,\tau)\right)}{Eh} \tag{B.4}$$

$$\frac{\left(-\nu^2+1\right)\left(R^2 p_r\left(\frac{\partial}{\partial\xi} u_{cn}(\xi,\tau)\right)-7Rp_r v_{sn}(\xi,\tau)-49Rp_r w_{cn}(\xi,\tau)\right)}{Eh} \tag{B.5}$$

B.2. Additional pressure terms in the Laplace- wavenumber domain

Projected on circumferential mode $n = 0$.

$$\frac{-2iR^2 p_r \left(-\nu^2+1\right) W_0 k}{Eh} \tag{B.6}$$

$$\frac{-2iR^2 p_r \left(-\nu^2+1\right) U_0 k}{Eh} \tag{B.7}$$

Projected on circumferential mode $n > 0$.

$$\frac{\left(-\nu^2+1\right)\left(-iR^2p_rW_{cn}k+49Rp_rU_{cn}\right)}{Eh} \tag{B.8}$$

$$\frac{\left(-\nu^2+1\right)\left(49Rp_rV_{sn}+7Rp_rW_{cn}\right)}{Eh} \tag{B.9}$$

$$\frac{\left(-\nu^2+1\right)\left(-iR^2p_rU_{cn}k-7Rp_rV_{sn}-49Rp_rW_{cn}\right)}{Eh} \tag{B.10}$$

C

Appendix C

C.1. Dispersion curve for the uncoupled shell $n = 3$ to $n = 6$

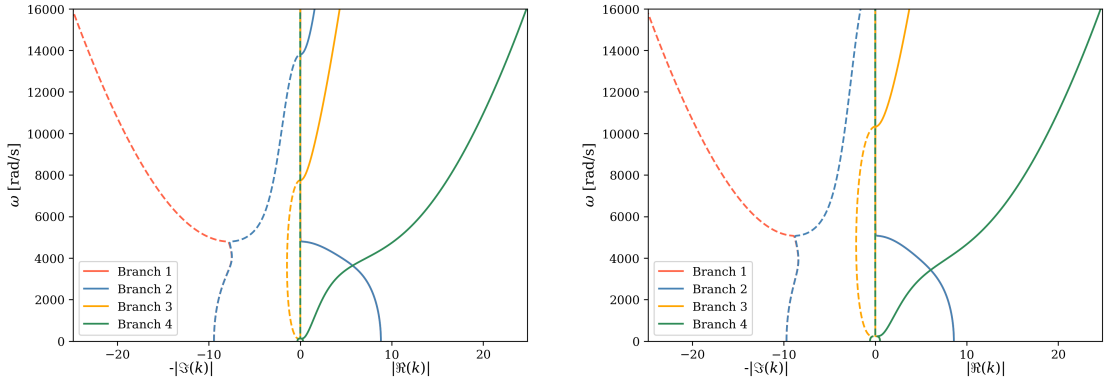

(a) Dispersion graph $n = 3$

(b) Dispersion graph $n = 4$

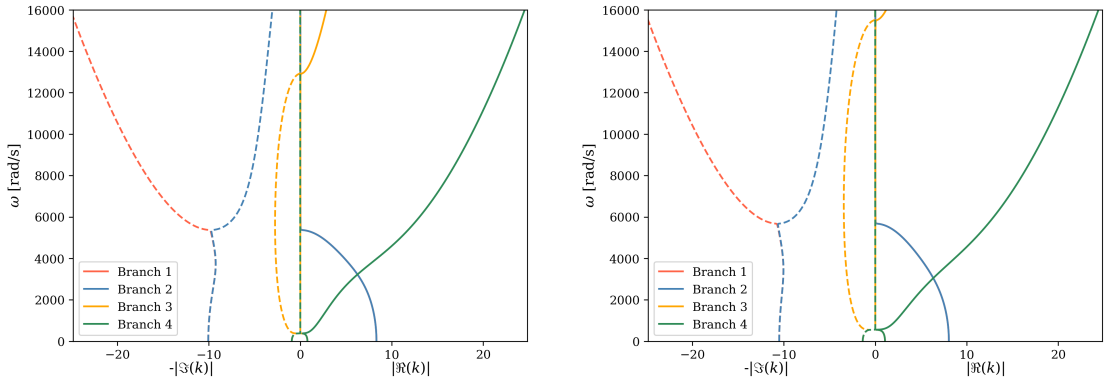

(c) Dispersion graph $n = 5$

(d) Dispersion graph $n = 6$

Figure C.1: Dispersion graph for a closed, free, cylindrical shell for the circumferential modes $n = 3$ to $n = 6$

D

Appendix D

D.1. Tuning of the beam model according to the shell dispersion curve

The dispersion relation of an EB-Beam has been extensively studied in the past and the derivation is therefore omitted for brevity. The dispersion relation Δ_{EB} shown below was obtained from [3] whereby k resembles the wavenumber, ω the angular frequency, k_s the spring constant of the Winkler foundation, EI the bending stiffness and ρA the mass per unit length

$$\Delta_{EB} = k^4 - \frac{\rho A}{EI}\omega^2 + \frac{k_s}{EI} = 0 \tag{D.1}$$

for which the individual dispersion branches can be computed by solving Δ_{EB} for k or ω.

$$k_{1,2} = \pm\sqrt[4]{\frac{\rho A}{EI}}\sqrt[4]{\omega^2 - \omega_c^2} \tag{D.2}$$

$$\omega_{1,2} = \pm\sqrt{\frac{EI}{\rho A}k^4 + \omega_c^2} \tag{D.3}$$

The cut-off frequency of this system is found by solving for ω such that $k = 0$ which results in $\omega_c^2 = k_s/\rho A$. To tune the beam according to the results from the shell model, the foundation spring stiffness k_s can be adjusted to match the cut-off frequency, depending on the mode considered (see Figs. 3.2 and 3.3). In Fig. 3.4 (b) it can be seen that shell mode $n = 2$ has the greatest amplitude and therefore contributes the most to the response of the system. Even though, the total response is composed of infinite modes (truncated at $n = 6$ mode), each contributing to the total response of the system, in the following, the beam model is tuned to the second mode. The cut-off frequency of the $n = 2$ mode is very small and is therefore not visible in Fig. 3.3 (c). Therefore a magnified plot of the low-frequency range can be seen in Fig. D.1 together with the tuned and original EB model.

The critical velocity is reached when the velocity of the moving load is equal to the phase speed of the propagating wave ($\omega_{1,2}/k$) [3]. The phase speed of the EB Beam can be computed based on Eq. (D.3) above which leads to the following expression:

$$c_{ph} = \pm\frac{1}{k}\sqrt{\frac{EI}{\rho A}k^4 + \omega_c^2} \tag{D.4}$$

From the equation of the critical velocity, it is evident that it depends not only on the cut-off frequency, which is influenced by the foundation stiffness but also on the bending stiffness of

the beam. This allows for independent tuning of the foundation stiffness and bending stiffness based on the cut-off frequency and the critical velocity, respectively. However, it is important to note that the distributed mass ρA is also dependent on the bending stiffness due to the geometrical properties of the cross-section. In other words, both the moment of inertia (I) and the cross-sectional area (A) are influenced by the dimensions and shape of the cross-section.

Due to the limited scope of this thesis, the bending stiffness is reduced by a factor without adjusting any cross-sectional properties, such that $EI_{tuned} = EI \cdot f_{EI,adj.}$. While the beam moves as a whole, the shell only deflects at the top portion, as illustrated by the cross-sectional displacement in Fig. 3.5, which results in a significantly lower activated mass of the shell.

To match the dispersion graph of the shell shown in Fig. 3.3, the foundation stiffness has to be reduced such that the cut-off frequency aligns with the one from the shell element ($n = 2$ branches, $\omega_c \approx 25\ rad/s$). Afterwards, the bending stiffness can be adjusted to match the critical velocities.

The dispersion graph in Figure D.1 confronts the original as well as the adjusted beam model to the shell model. Hereby the dispersion branches for $n = 2$ of the coupled shell considering $N_h = 2$ modes. As outlined in previous chapters, the computational limitations make it difficult to obtain the dispersion curves for $N_h = 6$.

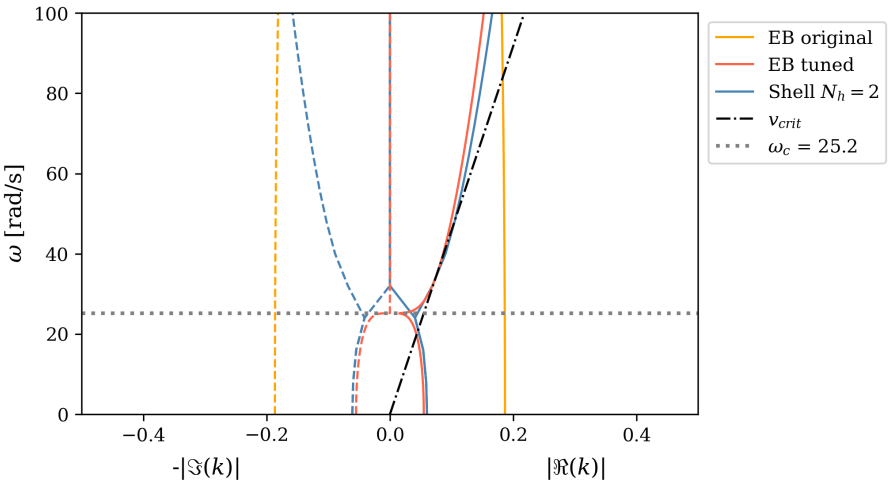

Figure D.1: Dispersion graph for Shell model for $N_h = 2$, $n = 1$ and tuned Euler-Bernoulli beam model

The dispersion graph in Fig. D.1 shows that the shell model has a significantly lower cut-off frequency than the original beam model ($\approx 300\ rad/s$), which is not shown in the graph for visual purposes. After adjusting bending and foundation stiffness the dispersion curves of the two models align overall well; only considering the shell bending branches. The adjustment factor for the spring foundation was determined analytically using the expression for ω_c and the one for the bending stiffness was determined iteratively; both are shown below:

- $f_{EI,adj.} = 0.9$
- $f_{ks,adj.} = 6.7e-3$